REPORT DOCUMENTATION PAGE

Form Approved
OMB No. 0704-0188

PLEASE DO NOT RETURN YOUR FORM TO THE ABOVE ORGANIZATION.

1. REPORT DATE *(DD-MM-YYYY)*	2. REPORT TYPE	3. DATES COVERED *(From - To)*
30-10-2004	Final Report	01-Nov-1995 - 31-May-2003

4. TITLE AND SUBTITLE
Effect of Gravity on Sheared Turbulence Laden with Bubbles or Droplets

5a. CONTRACT NUMBER

5b. GRANT NUMBER
N00014-96-1-0213

5c. PROGRAM ELEMENT NUMBER

6. AUTHOR(S)
Lasheras, Juan C. (PI)

5d. PROJECT NUMBER
02PR00779-01

5e. TASK NUMBER

5f. WORK UNIT NUMBER

7. PERFORMING ORGANIZATION NAME(S) AND ADDRESS(ES)
University of California, San Diego
9500 Gilman Drive
La Jolla, CA 92023-0934

8. PERFORMING ORGANIZATION REPORT NUMBER
2259AV

9. SPONSORING/MONITORING AGENCY NAME(S) AND ADDRESS(ES)
Office of Naval Research
Ballston Centre Tower One
800 North Quincy Street
Arlington, VA 22217+5660

10. SPONSOR/MONITOR'S ACRONYM(S)
ONR

11. SPONSOR/MONITOR'S REPORT NUMBER(S)
ONR 333, ONR 254

12. DISTRIBUTION/AVAILABILITY STATEMENT

DISTRIBUTION STATEMENT A
Approved for Public Release
~~Distribution Unlimited~~

13. SUPPLEMENTARY NOTES

14. ABSTRACT

This report studies the dynamics of particle-laden turbulent flows. Specifically, it addresses the effect of the turbulence on the concentration field and drift velocity of spherical particles. The coupling between the particle accumulation and the modification of the drift velocity of spherical particles. The coupling between the particle accumulation and the modification of the drift velocity is also investigated. Turbulent flows with and without mean shear are analyzed and the effect of the turbulent length scales on the behavior of the particles is described. The effect of the density ratio between the disperse and the continuous phase was considered in the two extreme cases of water droplets in air (1000) and air bubbles in water (1/1000).

15. SUBJECT TERMS
Shared turbulence laden with bubbles or droplets. Dynamics of particle-laden turbulent flows.

16. SECURITY CLASSIFICATION OF:			17. LIMITATION OF ABSTRACT	18. NUMBER OF PAGES	19a. NAME OF RESPONSIBLE PERSON
a. REPORT	b. ABSTRACT	c. THIS PAGE			Juan C. Lasheras
U	U	U	SAR	126	19b. TELEPHONE NUMBER *(Include area code)* 858-534-5437

Effect of Gravity on Sheared Turbulence Laden with Bubbles and Droplets

Award ONR-00014-96-1-0213 Technical Report

Alberto Aliseda and Juan C. Lasheras
Department of Mechanical and Aerospace Engineering
University of California, San Diego

30 October 2004

TABLE OF CONTENTS

ABSTRACT

Effect of Gravity on Sheared Turbulence Laden with Bubbles and Droplets

This report studies the dynamics of particle-laden turbulent flows. Specifically, it addresses the effect of the turbulence on the concentration field and drift velocity of spherical particles. The coupling between the particle accumulation and the modification of the drift velocity is also investigated. Turbulent flows with and without mean shear are analyzed and the effect of the turbulent length scales on the behaviour of the particles is described. The effect of the density ratio between the disperse and the continuous phase was considered in the two extreme cases of water droplets in air (10^3) and air bubbles in water (10^{-3}).

Experiments were conducted with water droplets in a homogeneous isotropic turbulent air flow, as well as with air bubbles in a turbulent water flow. To investigate the different effects introduced by mean shear, air bubbles were studied in both homogeneous isotropic turbulence and in a turbulent boundary layer. Measurements of the velocity of the particles were obtained by LDV and DPIV techniques. Instantaneous particle concentration maps were determined from flow visualizations. The length scales present in the concentration field were compared to the turbulence scales, in an effort to clarify the role of the different regions of the turbulent spectrum in the accumulation of micro-particles.

In all cases, the particles were found to be strongly concentrated due to the interaction with the turbulence. The characteristic length of the accumulation of particles in homogeneous isotropic turbulence was found to be between 10 and 20 times the Kolmogorov micro-scale of the turbulence. In the turbulent boundary layer, the instantaneous concentration field showed accumulation at a length scale equal to 100 times the viscous scale of the boundary layer, corresponding to the separation between the counter-rotating vortices that are responsible for ejections

and sweeps in the turbulent boundary layer. The mean bubble concentration, however, showed regions that scaled with the boundary layer thickness. The drift velocity of the particles due to gravity was found to differ from the values predicted in still fluid. This difference was found to depend on the turbulent intensity and to scale with the particle Stokes number. The settling velocity of droplets was increased by their interaction with the turbulent flow. The rise velocity of the bubbles, on the other hand, was reduced by the turbulence. Only in the region where the mean shear induces accumulation of the bubbles, their rise velocity is enhanced over the value in still fluid.

Chapter 1

Introduction

The study of turbulent multiphase flows has direct relevance in many industrial and environmental processes. Those processes, including combustion chambers and nuclear reactors, as well as cloud dynamics and gas exchange between the ocean and the atmosphere, often involve a turbulent carrier flow and a dilute concentration of the dispersed phase. In these situations, the behaviour of the dispersed phase is greatly influenced by the characteristics of the turbulence. Thus, a well controlled laboratory experiment can produce valuable information on the effect of the underlying turbulence on the behaviour of very small particles with densities either larger or smaller than the carrier fluid. From the results, the different effects can be isolated and models built to help predict the incidence of the various phenomena present in real-life applications. That way, knowledge of the influence of the turbulence on the settling velocity and concentration of particles can help improve current models for droplet combustion in jet engines or sediment transport in river beds and coastal areas. Similarly, better knowledge of the rise velocity of microbubbles in a turbulent flow can lead to improved understanding of the mechanisms by which carbon dioxide is removed from the atmosphere by the ocean, to mention just a few examples of possible applications.

The study of the interaction of turbulence with a dispersed phase has a long and illustrious history, starting with the theory of turbulent dispersion by

Taylor (1921). However, for many years such theories treated turbulence as a random source for agitation of the particles. It was not until the past few decades that the necessary tools made possible to study in detail the many intriguing phenomena that characterize this type of flows.

In their seminal work, Snyder & Lumley (1971) found the decisive role that the particle inertia and the crossing trajectories effect have on the velocity autocorrelation of the particles. Wells & Stock (1983) tried to decouple the effect of inertia from the crossing trajectories on the dispersion of particles by a turbulent flow. These effects are coupled by the earth's gravitational field, but it was found that, when isolated, particle inertia seemed to increase the dispersion coefficient. Crossing trajectories effect, on the other hand, tend to decrease long time dispersion, although it is negligible when the settling velocity is smaller than the carrier flow r.m.s., as predicted by Reeks (1977). The argument on which turbulence time scale should be used to characterize particle inertia was already open at that time, and despite the huge amounts of information produced since then, it still seems to linger.

With the advent of Direct Numerical Simulation, Squires & Eaton (1991*a*) and Elghobashi & Truesdell (1992), studied particle dispersion in homogeneous and isotropic turbulence. The first simulation found qualitatively the same behaviour found in the two experiments mentioned above, that is, that particle inertia increases long time dispersion coefficients and that gravitational settling greatly reduces dispersion when it's larger than the r.m.s. velocity of the flow. The second simulation provided quantitative comparison with the experiments. Even with Re_λ equal to one third the experimental one, the mean square displacement showed good agreement with the experiments. The kind of detailed information provided by the simulations allowed physical insight into the interaction mechanism to be gained. Crossing trajectories was found to be associated with negative loops in the velocity autocorrelation of the particles, largest for the heaviest particles, dispersion in the direction of gravity was shadowed by the settling, and, in the absence

of gravity, long term dispersion coefficients of both particles and fluid elements reached an asymptotic state, as predicted by Taylor (1921).

So far, the effect of gravitational settling on the interaction between particles and turbulence had been considered as a dispersion reducing factor. Using the equation of motion for a rigid sphere in a nonuniform flow, Maxey & Riley (1983), the influence of turbulence on the settling velocity could be studied. The influence of a single vortex on the settling trajectory of a particle was analytically computed by Tio *et al.* (1993*a*). The interaction of a particle with a two dimensional cellular flow, Maxey (1987*b*), was a first approach to the settling in turbulence. The settling in random flows with a prescribed turbulence-like spectrum followed, Maxey (1987*a*), and finally the full Navier Stokes simulation and the particle tracking could be run simultaneously, Wang & Maxey (1993*a*). They found that heavy particles settling under gravity in a turbulent flow have a mean velocity in the direction of gravity that is larger than the one they would have in still fluid (predicted by Stokes flow, since the Reynolds number of the particles is very small). They proposed the 'preferential sweeping mechanism' that explains this effect in terms of the drift created by the particles inertia, coupled with the crossing trajectories effect due to gravity. In short, when an inertial particle that has a certain settling velocity encounters an eddy, it is more probable that it will be swept to the downward side than to the upward side. Thus, drag is more likely to increase than to reduce the settling velocity. A cartoon of this can be seen in figure 1.1. When averaged over the history of one particle, lagrangian, or over the instantaneous velocities of all particles in the flow, eulerian, the average vertical velocity is found to be greater than the Stokes velocity.

Associated with this phenomenon is the preferential accumulation of inertial particles in a turbulent flow. This anti-gradient diffusion effect consists in the accumulation of particles in the high strain regions between the vortex cores. Due to their larger density, particles drift outwards with respect to fluid elements in their rotational trajectories around vortex cores. Thus, they are found prefer-

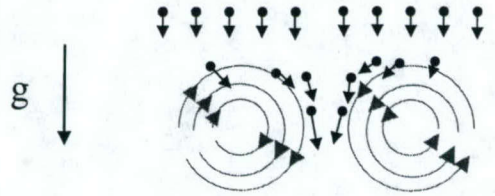

Figure 1.1: Heavy particle interacting with a vortex pair.

entially in convergence regions, where vorticity is low. Despite the fact that the vorticity structure in a turbulent flow is very complicated and it doesn't render itself to such simple considerations, preferential accumulation by turbulence has been observed both in numerical simulations and experiments in many different types of flows. Crowe *et al.* (1988) reviewed different studies of preferential accumulation of particles in free shear flows. In these type of flows, diffusion is controlled by the large scale coherent vortices. For homogeneous flows, Maxey & Corrsin (1986) showed in their analysis that the divergence of the particle velocity is positive in regions of high vorticity and negative in regions of high strain, and called this tendency inertial bias. Squires & Eaton (1990, 1991a, 1991b) studied preferential accumulation in homogeneous isotropic turbulence as well as in homogeneous sheared turbulence. They found very strong inhomogeneities in the concentration field, with peak concentrations up to 25 times the mean. Intermediate Stokes number particles showed the strongest effects, as predicted by the analysis. Regions of preferential accumulation were correlated with regions of negative value of the second invariant of the deformation tensor. Wang & Maxey (1993*a*) used Kolmogorov scaling for the Stokes number and found maximum accumulation for Stokes number equal to one. They introduced a parameter to quantify the deviation from randomness of the particles, $D_1 = \Sigma(P(c) - P_{random}(c))^2$. Fessler *et al.* (1994) introduced a second parameter to quantify the difference between the spatial distribution of particles in the flow and the one given by a random process, $D_2 = \sigma - \sigma_p/\mu$. In their experiments, particles with different Stokes num-

bers were introduced in a turbulent channel flow and images of the center plane were analyzed to study preferential accumulation. Both parameters showed that preferential accumulation occurs at length scales in the dissipation range (between 6-20 η).

The literature on bubbly turbulent flows is much more concise. In normal situations like air bubbles in water, bubbles with Stokes number of order one do not satisfy the conditions that the Reynolds number and the ratio of the diameter to η are smaller than unity. Thus, the equation of motion is still a matter of discrepancy. A recent review can be found in Magnaudet & Eames (2000).

The experimental studies of turbulent bubbly flows has been mostly carried out with relatively large bubbles and volume fractions. Lance & Bataille (1991) studied the turbulence characteristics of the continuous phase in an upwards flowing water channel, where turbulence was introduced both by a grid and by ellipsoidal bubbles with an equivalent diameter of 5 mm, approximately equal to the Taylor microscale of the single phase flow. As the bubble void fraction was increased from 0 to 5%, the flow transitioned from a regime where the hydrodynamic interaction of the bubbles is negligible to one in which the bubbles transfer a great amount of kinetic energy to the flow, modifying the one dimensional spectra from the classical -5/3 power law to a -8/3 dependency. More recently, Panidis & Papailiou (2000) revisited the problem of bubbles injected into an upward-moving, grid-induced turbulent water flow. They focused on the bubble spatial distribution, as well as on the effect of the bubbles on the underlying carrier flow turbulence. They found a non uniform distribution of the bubbles, with a peak in the local void fraction located approximately halfway between the channel wall and the centerline. An associated peak in the streamwise velocity was also reported, presumably induced by the stronger buoyancy of the bubbles at the location of the void fraction peak. The reasons for the existence of these peaks, as well as their location was not provided and several mechanism, such a lift due to the interaction with the mean shear, Segre & Silberberg (1962), or preferential accumulation by large

eddies, Rightley & Lasheras (2000), were suggested as possible. Because in these experiments the bubbles were several millimeters in diameter and the volume fraction was very high ($\approx 5\%$), the effect of the carrier flow on the dynamics of the bubbles was not satisfactorily analyzed. Moreover, because the mean flow was in the same direction as gravity, the rise velocity was not considered.

Sridhar & Katz (1995) did experiments to determine the forces acting on bubbles in the 500-800 μm range due to nonuniform flow. They found drag coefficients that agreed well with steady state data and lift coefficients that did not agree with existing theoretical or numerical models. In the course of their experiments they measured the trajectory of a bubble entrained by a laminar vortex and were able to reproduce it with calculations using the equation of motion from Maxey & Riley (1983), with adequate coefficients. Rightley & Lasheras (2000) studied the dispersion of microbubbles in a free shear layer. Using bubbles with diameters smaller than 100 μm so that their rise velocity was negligible, they were able to characterize the effect of the large coherent vortices present in a mixing layer on the bubble dispersion. More recently Poorte & Biesheuvel (2002) have reported experimental evidence of a decrease in the rise velocity of bubbles caused by homogeneous isotropic turbulence, created by an active grid.

Numerical simulations of the interaction of bubbles with a vorticity field have been carried out by Maxey and collaborators. Wang & Maxey (1993*b*) reported preferential accumulation of bubbles in homogeneous isotropic turbulence. In parallel with the simulations of the settling particles, they confirmed the intuition that microbubbles would be subject to the same accumulation effect due to turbulence, except because the density ratio is inverted, accumulation of bubbles occur in regions of very high vorticity. It took several years, however, to report the equivalent study for the rise velocity of the bubbles. Counter to what happens with the particles, bubbles have their rise velocity reduced by the turbulence. Maxey *et al.* (1997) found this preferential accumulation to reduce the rise velocity of the bubbles, due to the increased residence time of the bubbles in the downward

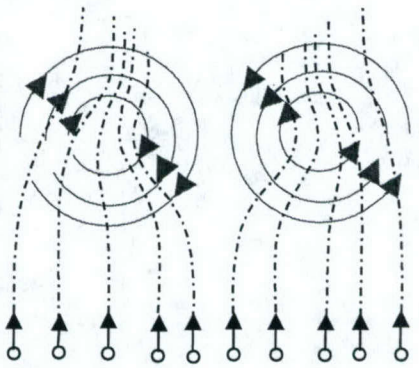

Figure 1.2: Rising bubbles interacting with a vortex pair.

side of the eddies, where there is theoretical static equilibrium point Tio *et al.* (1993*b*). This is due to the fact that, instead to being driven by inertia to the downward convergence zones between eddies, they are driven to the eddies cores, where pressure forces oppose the rising that would take them away from these regions. A cartoon of this mechanism is drawn in figure 1.2. Spelt & Biesheuvel (1997) and Maxey *et al.* (1997) found these effects in their simulations of homogeneous isotropic turbulence laden with bubbles. Direct Numerical Simulations of bubbly turbulent flows have been performed by Druzhinin & Elghobashi (1998), who found that preferential accumulation is not significant for very small bubbles in low Reynolds number homogeneous, isotropic, decaying turbulence. Under these circumstances the effect of the bubbles is similar to stratification, enhancing the turbulence decay for stable stratification and delaying it in the unstable case. Mazzitelli *et al.* (2003) recently reported the results of a DNS study of microbubbles in homogeneous isotropic turbulence. They focused the attention on the effect of lift force and found that bubbles increase their residence time in the downward side of the eddies, thus reducing the bubble mean rise velocity. Large scale velocity fluctuations in the carrier fluid are inhibited by the buoyancy, while energy is added at the small scales of the turbulence, resulting in a net reduction of the turbulence decay rate.

The interaction of bubbles with a turbulent boundary layer has been studied experimentally by Moursali *et al.* (1995) and Marie *et al.* (1997). They introduced large ellipsoidal bubbles (3.5-6 mm diameter) at the leading edge of a vertical flat plate and measured the void fraction distribution as the boundary layer developed. They found that larger bubbles flow away from the wall, while smaller bubbles remain inside the boundary layer, with the void fraction peaking at a distance from the wall slightly larger than the bubble radius. Merkle & Deutsch (1992) studied the behaviour of small spherical bubbles introduced in a flat plate turbulent boundary layer. They determined that the bubbles tend to diffuse throughout the boundary layer. Unfortunately, the focus of the experiment was drag reduction due to the bubble injection. Accordingly, a very large void fraction was introduced and the information pertaining to the bubbles was only qualitative. More recently, Felton & Loth (2001) studied bubbles in the 400-1200 μm range in a vertical boundary layer. They were interested in the dynamics of large spherical bubbles injected in an upward flowing channel. The mean void fraction profiles were obtained but not the instantaneous concentration fields. Moreover, the mean flow was in the same direction as the buoyancy, so the rise velocity was not considered.

Results from well resolved direct numerical simulations of a bubbly turbulent boundary layer became available in the literature only very recently in the work of Ferrante & Elghobashi (2004). They performed Direct Numerical Simulations of a spatially developing flat plate laden with micro-bubbles. They found that the bubbles induce compressibility of the carrier fluid velocity field and that this is the leading order term in the modification of the dynamics of the turbulent boundary layer laden with micro bubbles. They compared different orientations of the plate relative to gravity and determined that it is compressibility, and not buoyancy, that creates a secondary flow normal to the wall. This flow away from the wall is responsible for the lifting of the streamwise turbulent structures that produce ejections and sweeps. They showed how this mechanism can explain the

decrease in the rate of production of turbulent kinetic energy and the reduction of the skin friction by microbubble injection.

In spite of the large body of work done on this subject, several issues stand out as the important questions that still remain open in the study of dilute turbulent multi-phase flows. The first one is how the turbulence modifies the drift velocity, settling or rising, that particles have in the presence of a gravitational field. This phenomenon that has been theoretically analyzed and numerically simulated had still not been confirmed experimentally, and no model had been proposed to address it. The second important topic is the preferential accumulation of particles due to the turbulence. This effect, that acts against the standard paradigm of enhanced mixing by turbulence has been explained by a simple characterization of the turbulence as an array of eddies, and has only been partially analyzed in experimental and numerical studies. However, the issue of which length scales, of the continuous spectrum of the turbulence, was responsible for it, had not been satisfactorily studied. The third question, related to the first two, is what is the role that the strong inhomogeneities in the concentration field which result from preferential accumulation of particles due to turbulence, play in the settling velocity. Although Wang & Maxey (1993*a*) hinted at the possibility of a coupling between preferential accumulation and preferential sweeping, it was considered until now that this was just a statistical artifact caused by the uneven sampling of particles in the downward side of the eddies.

Finally, the last important remaining open question is the effect of a mean shear in the velocity profile of the carrier flow, such as the one created by the presence of a solid wall, in the preferential accumulation and modification of the gravitational drift. Although these effects have been studied in homogeneous isotropic turbulence, forced or decaying, the influence of mean shear in the carrier flow velocity has not been yet characterized.

In this introduction, and for the rest of the thesis, the flows studied are composed of two phases: a disperse phase, the particles, and a continuous phase,

the carrier fluid. The particles are isolated, spherical volumes of one fluid immersed into a continuous expanse of another fluid, the carrier flow. The particles can be heavier than the surrounding fluid, dust or water droplets in air, or lighter, such as air bubbles in water. General results, that are not dependent on the density ratio between the disperse and continuous phases, will be described in terms of the behaviour of particles. Specific results for a certain value of the density ratio will be given in terms of droplets/heavy particles or bubbles.

The primary aim of this thesis is to provide new experimental evidence of the effect that the interaction of a turbulent flow with a dilute disperse phase has on the dynamics of the turbulence and the particles. In particular, this thesis focuses on the four topics stated above. To answer these questions, three different experiments have been designed and carried out.

The first experiment involved small spherical droplets injected into a grid generated homogeneous isotropic decaying turbulent flow. The settling and accumulation of heavy particles in unbounded turbulence with no mean shear were studied. In a second experiment, small spherical air bubbles were injected into a turbulent water channel. Homogeneous isotropic decaying turbulence was generated by a grid, and the behaviour of bubbles was studied in a way equivalent to the first experiment. The two limits of the density ratio between the disperse phase and the carrier fluid were thus covered. To study the effect of mean shear on the interactions between the particles and the turbulent carrier flow, the third experiment consisted of an investigation of the dynamics of a bubble-laden turbulent boundary layer. The presence of a solid wall introduced mean shear in the velocity profile and a corresponding new length scale. The effect of the mean shear on the preferential accumulation of bubbles and the modification of their rise velocity was carefully described and the similarities and differences between this wall-bounded flow and the previous cases were systematically studied.

The outline of the thesis is as follows. Chapter 2 describes the results of the experimental study of heavy particles settling in a homogeneous isotropic

turbulent flow. The behaviour of air bubbles in homogeneous isotropic turbulence is characterized in Chapter 3, with special emphasis on the modification of the rise velocity due to the turbulence in the carrier flow. Chapter 4 describes the behaviour of microbubbles in a turbulent boundary layer, and their effect on the dynamics of the turbulence. The flow at the junction between the solid wall and the free surface is described in Chapter 5, with particular attention at how the bubble-laden case differs from the single phase flow. The conclusions extracted from these three experiments, as well as suggestions for future work in this area, are summarized in Chapter 6.

Chapter 2

Effect of homogeneous isotropic turbulence on the settling velocity of heavy particles

2.1 Experimental set-up

The experiments were performed in a horizontal blow down wind tunnel, with a test section length of 2.5 m and a square cross-section of 20 cm by 20 cm. The air flow is laden with water droplets injected upstream of the test section. A sketch of the facility is shown in figure 2.1. The air flow is supplied by a blower and passes through a nozzle, with an area contraction ratio of 2:1. Fine mesh screens and honeycombs are also used to damp out all possible inhomogeneities in the flow before entering the test section. The turbulence is produced by a grid in which the liquid atomizers are embedded. The grid is made up of round tubes, with a diameter of 1 mm and a lateral spacing of 15 mm.

Water droplets are injected in the air stream through an array of atomizers embedded in the vertical bars of the grid, producing a uniform spray over the central region of the tunnel (14 cm by 14 cm). Each atomizer, a sketch of which is shown in figure 2.2, consists of two parallel tubes carrying water and air. The

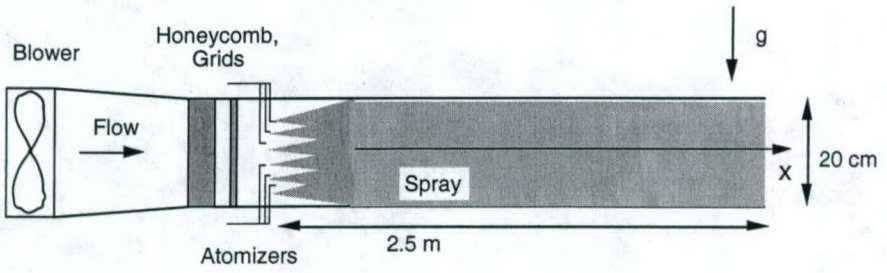

Figure 2.1: Experimental facility.

water is delivered normal to the main flow while the pressurized air exits the nozzle parallel to the main stream. The high momentum air jet impinges perpendicularly on the water jet, atomizing the liquid and producing a spray jet. The droplet size distribution and liquid mass fraction of the spray can be controlled by the pressure of the air supply line and by the flow rate of water, as shown by Lázaro & Lasheras (1992). In all the experiments reported here the air pressure was kept constant, while the water flow rate was varied over a range where its influence on the resulting droplet size distribution was negligible. Additionally, the droplet size distribution was measured at different locations along the test section and found to be uniformly the same. This allowed us to discard coalescence and breakup effects in all the experiments. The droplet size distribution used through all the experiments reported here is shown in figure 2.3. The droplet turbulent Weber number, $We_t = \rho_p \overline{u(d)^2} d/\sigma$, is always less than 10^{-2} for all droplets in the distribution. Thus, surface tension dominates over the unsteady pressure distribution from the gas that may deform the droplets, allowing us to assume a spherical shape for the droplets during the experiments.

The characteristics of both the single-phase turbulent carrier flow and the injected droplets were carefully determined by hot-wire anemometry and Phase Doppler Particle Analysis (PDPA) and the region of the flow where wall effects could be neglected was identified. Several iterations of changes in the geometry and the operating conditions of the experiment were necessary to ensure that the conditions selected corresponded to nearly homogeneous, isotropic, slowly decaying

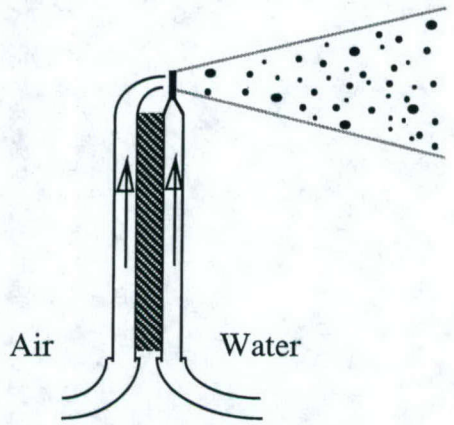

Figure 2.2: Sketch of an atomizer used in the experiment.

turbulent particle-laden flow.

2.1.1 Turbulence characterization

The characteristics of the turbulence of the single phase air flow were determined by hot-wire constant temperature anemometry. An AA Lab Systems AN-1003 anemometer with a TSI, 1210-T1.5, single wire probe were used, together with a National Instruments BNC 2090 digital acquisition card. Information was acquired at a frequency of 10 kHz, which is fast enough to resolve the dissipation range of the turbulent spectrum. The length of each individual data set was $5 \cdot 10^5$ samples (or 50 s), and the statistically stationary flow hypothesis was checked comparing the results with data sets which were $2.5 \cdot 10^5$ and 10^6 points long. The data was then processed to compute the turbulent characteristics. The selected flow has a bulk Reynolds number ($Re = U_\infty l/\nu$) of $7.5 \cdot 10^4$ and a Reynolds number based on the Taylor microscale of $Re_\lambda = 75$.

It was observed that the air injected through the atomizers contributed significantly to both the total momentum (up to 10%) and the initial value of the turbulent intensity of the carrier flow (up to 50%). Therefore, the characterization of the turbulence was done with the atomizers injecting air at their normal operating conditions. The fact that the injection of air contributes significantly

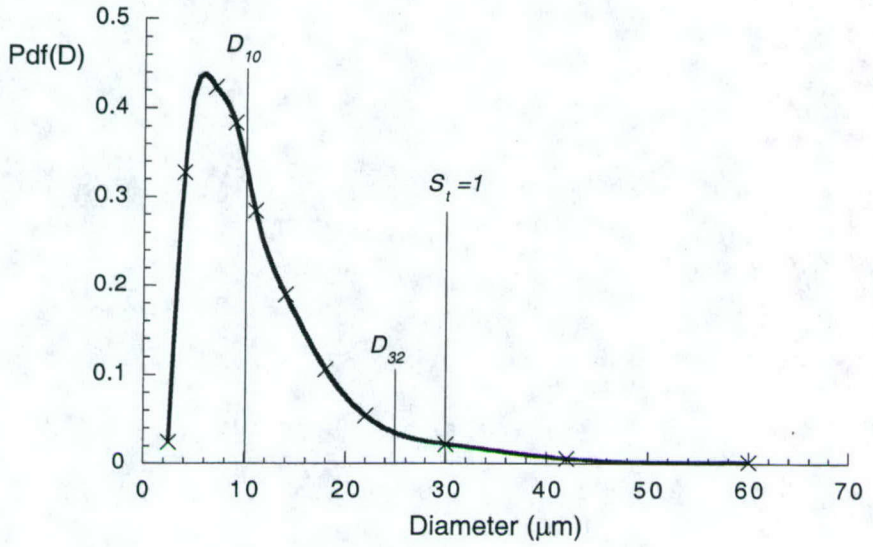

Figure 2.3: Probability density function of the droplet's diameter.

to the turbulence intensity made the grid of atomizers an active grid, potentially modifying the decaying characteristics of the turbulence produced by it.

Measurements were taken at 6 downstream locations, over a set of 16 x 6 points in the z and y directions with a spacing of 1 cm, covering the central part of the wind tunnel. The measuring region extended from x=83 cm to x=207 cm (see sketch in figure 2.4). Measurements showed that the flow could be considered to be homogeneous in planes perpendicular to the axial velocity (y-z planes). Vertical profiles of the mean axial velocity (U) are shown in figure 2.5. Although the growth of the boundary layer can be observed in figure 2.5(b), the selected region of interest for our experiments is located well outside its limits. Thus, within the test section relevant for our experiments, the flow can be assumed to be unaffected by the presence of the walls. Vertical profiles of the axial velocity RMS (u') are shown in figure 2.6. Again, the effect of the boundary layer is found to be restricted to a region far away from the measuring zone.

In order to characterize the decay of the turbulence, the inverse of the turbulent kinetic energy can be fitted to a power law. Comte-Bellot & Corrsin (1966) proposed an exponent of between 1.2 and 1.3 to best fit the data over

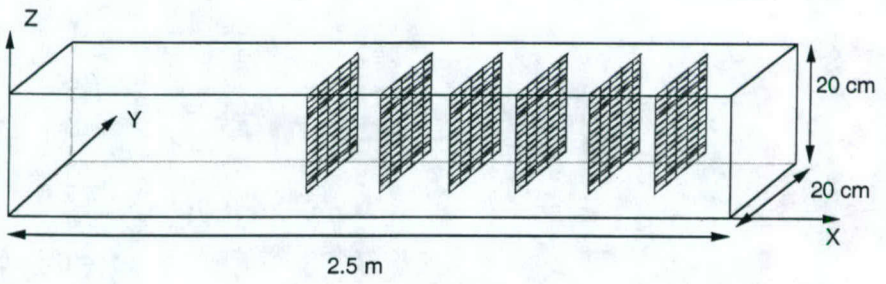

Figure 2.4: Sketch of hot-wire measurement locations.

the whole range. It has been further proposed, Wells & Stock (1983), that three different regions of decay can be identified in grid induced turbulence. The near region, which extends from 10 to 150 mesh distances downstream from the grid, is characterized by a decay of the turbulent intensity proportional to the inverse of the distance downstream. In the far region, which extends from 500 mesh lengths onwards, the decay of the turbulent intensity is faster and is given by $\left(\frac{U}{u'}\right)^2 \sim (x - x_0)^{5/4}$. There is also some evidence of an intermediate region where the turbulent intensity decays as $\left(\frac{U}{u'}\right)^2 \sim (x - x_0)^{10/7}$.

The decay of the turbulent intensity measured at the centerline of the tunnel is shown in figure 2.7. Since all of our data lies well within the near region and the macroscale Reynolds number is almost constant, it is justified to apply a linear fit to our data, $(U/u')^2 = 38.41(x/M - 10.17)$. Thus characterized, we have the means to compare the decay law for the active grid in our experiment with those of passive grids.

Since the typical time scale of the decay of the turbulence is much larger than the particle's response time, we will assume quasi-stationary conditions when analyzing the problem of the interaction of the particles with the turbulence. Following Nir & Pismen (1979), the time of decay of the turbulence as seen by a particle moving with the mean streamwise velocity of the flow can be estimated by $t_d^{-1} = U\mathrm{dln}(u')/\mathrm{d}(x - x_0)$. In all our experiments, this time is of the order of 0.2 s, which is much larger than the response time of all particles. Thus, we can assume that the particles are always in equilibrium with the surrounding turbulence.

a)

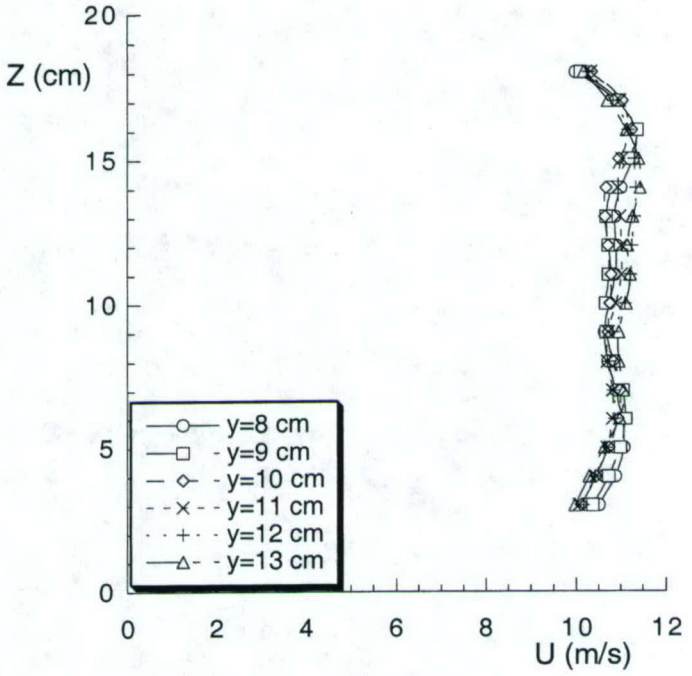

b)

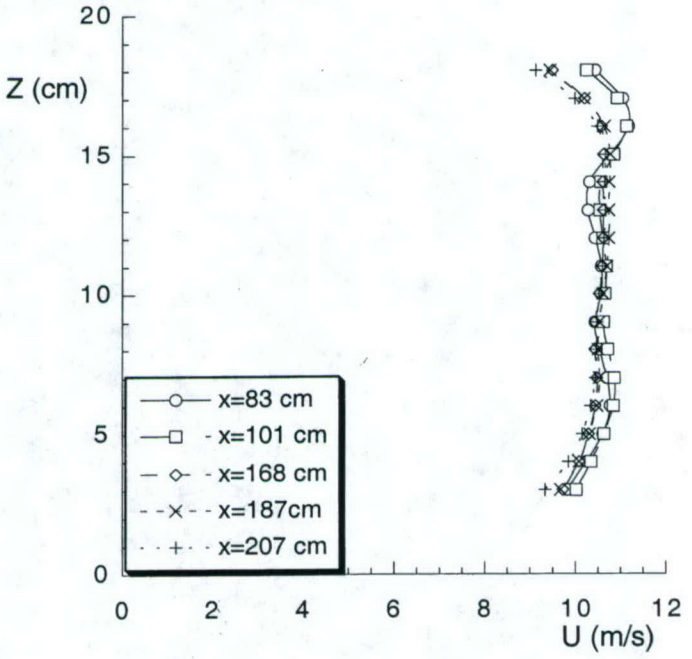

Figure 2.5: (*a*) Mean axial velocity profiles (x=101 cm). (*b*) Downstream evolution of the mean axial velocity at the center of the tunnel.

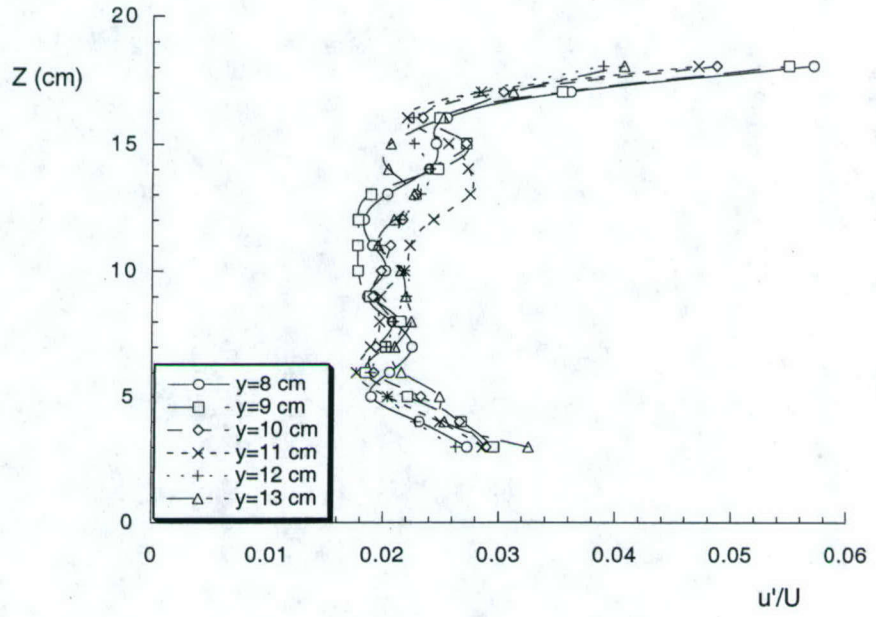

Figure 2.6: Turbulent intensity profiles (x=101 cm). Vertical sections of the tunnel

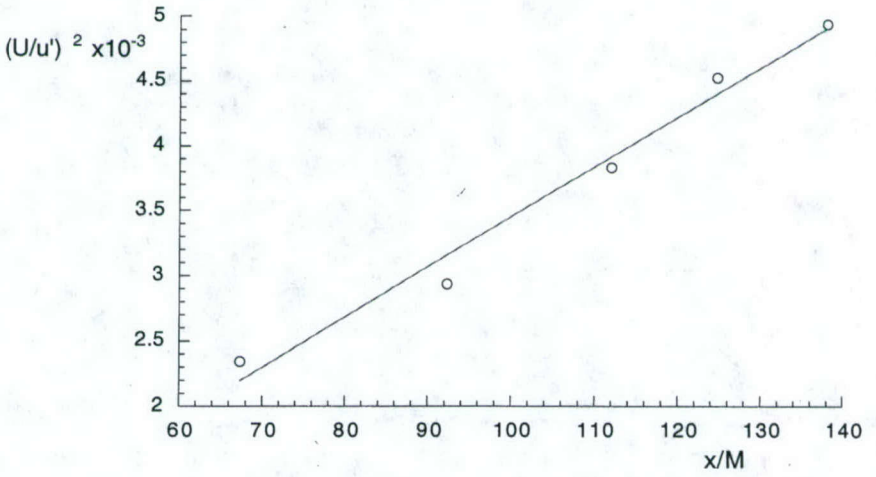

Figure 2.7: Decay of the turbulent intensity along the test section.

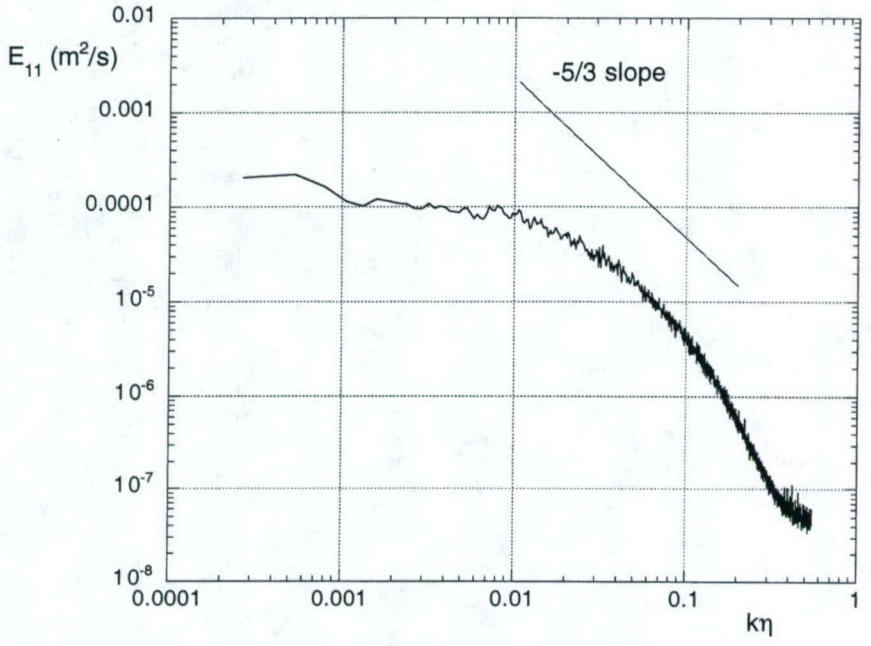

Figure 2.8: Longitudinal one-dimensional turbulent energy spectrum.

The one-dimensional power spectrum of the carrier fluid (air flow) was computed at all downstream locations in the tunnel, using a Fast Fourier Transform algorithm. The spectra, plotted in figure 2.8, shows the typical features of a moderate Reynolds number flow, including a very short inertial subrange of less than a decade.

The turbulence characteristics obtained from the hot-wire measurements are shown in table 2.1. The dissipation rate of turbulent kinetic energy was computed with two different methods; as an integral of the unidirectional spectrum, Eq. 2.1, and from the derivatives of the fluctuating velocities, Eq. 2.2, Hinze (1975). Both calculations were found to agree to within 10% for all downstream locations.

$$\epsilon = 15 \cdot \nu \int_0^\infty k^2 \cdot E_{11}(k) dk, \tag{2.1}$$

$$\epsilon = -\frac{1}{2} \frac{\mathrm{d}\bar{q}^2}{\mathrm{d}t}. \tag{2.2}$$

The Kolmogorov microscales were computed from their definitions:

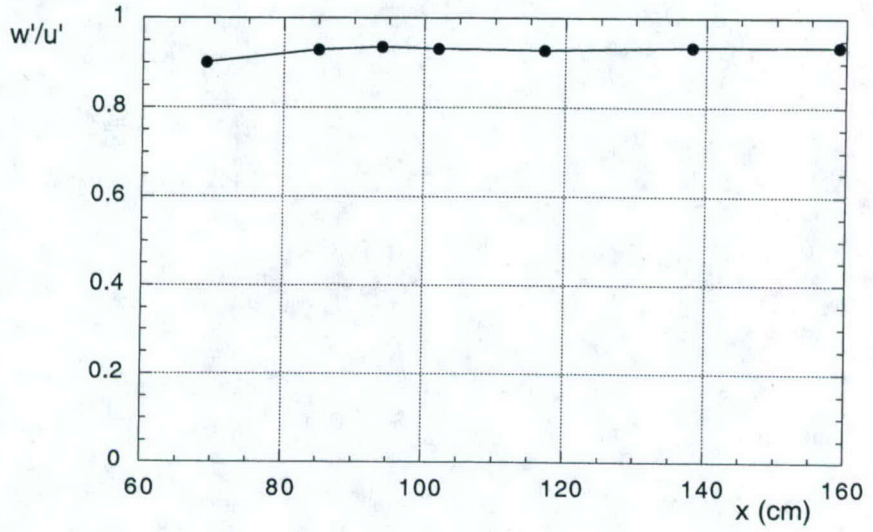

Figure 2.9: Ratio of the RMS of the horizontal and the vertical velocities.

$\tau_k = (\nu/\epsilon)^{1/2}$; $\eta = (\nu^3/\epsilon)^{1/4}$; $v_k = (\nu/\epsilon)^{1/4}$. It is important to notice that the Kolmogorov length scale in the carrier flow is an order of magnitude larger than the droplet's diameter (both the arithmetic and Sauter mean diameters).

To characterize the isotropy of the carrier gas, measurements of the RMS of the velocity of the flow in the three directions are needed. Measurements of the velocity in the x and z directions were taken with the phase Doppler particle analyzer system (PDPA), described in section 2.2. For this purpose, the flow was seeded with very small smoke particles ($d < 1\mu m$), which behave as fluid elements, and their horizontal and vertical velocities were processed to obtain the values of

$x(cm)$	u' (cm/s)	$\epsilon(m^2/s^3)$	L (mm)	$\lambda(mm)$	$\eta(mm)$	$\tau_k(ms)$	$v_k(cm/s)$
83	26.2	1.75	37.7	5.06	0.210	2.92	7.16
101	21.1	1.00	43.0	5.37	0.241	3.87	6.23
138	19.6	0.88	48.4	5.26	0.249	4.13	6.03
168	17.6	0.76	50.5	4.80	0.258	4.43	5.82
187	16.3	0.68	56.5	4.64	0.265	4.69	5.66
207	15.6	0.61	56.2	4.66	0.273	4.96	5.50

Table 2.1: Downstream evolution of the turbulence characteristics for the single phase air flow.

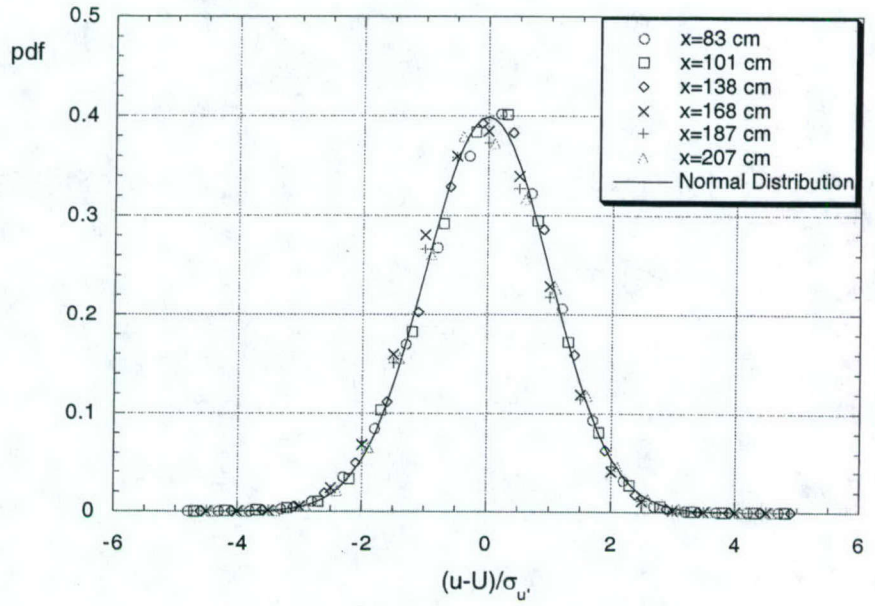

Figure 2.10: Probability density function of the fluctuating velocity.

u' and w'. As a test of the accuracy of this procedure, it should be noted that the value of u' obtained from the PDPA measurements agrees very well with the one we measured using the hot-wire technique. In figure 2.9, we plot the ratio of u' and w' showing that it remains very close to unity, with a maximum deviation of less than 10%. In addition, the probability density function (PDF) for the fluctuating velocity, shown in figure 2.10, was found to be nearly Gaussian.

2.1.2 Two-phase flow measurement technique

The experimental technique used to characterize the dispersed phase was particle Doppler analysis. The equipment selected for this task was an Aerometrics Phase Doppler Particle Analyzer (PDPA). This system allows for simultaneous measurements of the horizontal and vertical velocities, as well as of the diameter of the particles. Two beams, with wavelengths of 514 nm (green) and 488 nm (blue), from a Coherent I70 2-C Ar^+ continuous laser are split and a frequency shift is introduced in one branch of each color. The beams are then driven through optical fibers to a 250 mm focal length transmitting lens. The green beams are positioned

in the horizontal plane and the blue ones in the vertical plane. The beams cross at a point of the flow materializing the probe volume, which is very small even compared with the Kolmogorov scale of the flow (0.5x0.5x2.5 η^3). Any particle crossing the probe volume scatters the light which is received by the collecting optics located in the forward side at 30° from the emitter. This mode of operation, 30° forward first mode of refraction, has been shown to be the most advantageous for water droplets in an air flow, Bachalo (1994). The velocity and size of the droplets are, then, computed from the frequency and phase-shift introduced by the droplets in the Doppler bursts. A complete description of the system, as well as a detailed study of the error in the measurements, can be found in Kiger (1995). Since in the present work the turbulence is homogeneous and isotropic, no velocity bias correction due to large scale structures is necessary. However, it is important to take into account the alignment errors introduced in the vertical velocity measurements by the fact that the laser beams can only be positioned in the vertical plane with finite precision. Since the horizontal velocity is two orders of magnitude larger than the vertical one, a small projection of the horizontal velocity measured by the vertical channel will create a significant error. This error is the same for all particles because the horizontal velocity is the same for all droplets (deviations are smaller than u'). This alignment bias can be effectively corrected by subtracting the measured vertical velocity of the smallest droplets in the lowest volume fraction case, whose average vertical velocity should be zero since they follow the flow, from all the vertical velocity measurements.

The uniformity of the droplet seeding was checked using a sampling technique. A thin tube, 10 mm in diameter, was introduced in the tunnel and positioned parallel to the main flow. The water flow rate collected by the tube was measured directly while the air flow rate was computed based on the tube diameter and the air velocity measured with one of the PDPA channels. Since the dispersed phase adopts the carrier flow axial velocity soon after injection, the volume fraction can be estimated by the ratio of the volumetric flow rates. $\alpha = Q_l/(Q_g + Q_l)$.

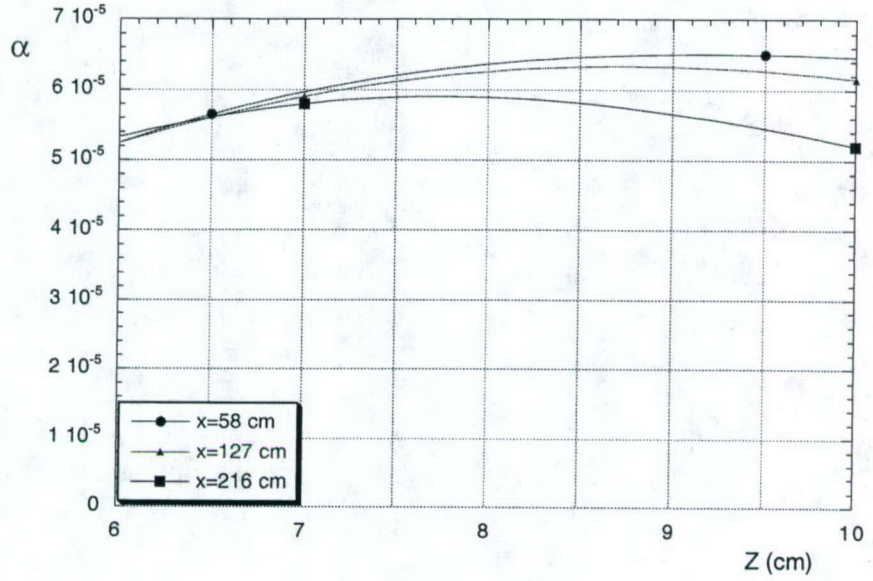

Figure 2.11: Local volume fraction profiles at different locations downstream. y=10 cm.

As shown in figure 2.11, the sampling determined that the injection was uniform within 10% in a 4 cm region centered around the point were the measurements were taken (z=8 cm).

2.1.3 Flow visualizations

A high resolution (1008x1008 pixels) digital camera was used to obtain images of the flow at several locations downstream of the particle injection. The flow is illuminated with a Continuum Surelite I, 5 W pulsed Yag laser, whose light is directed through a cylindrical lens and a rectangular slit so that a very thin sheet of light is projected into the tunnel. The width of the sheet is approximately 1 mm (or 5η) so integration in the direction perpendicular to the flow is minimized, and the duration of the pulses is 10 ns, short enough to freeze the motion of the droplets. The camera is mounted perpendicular to the laser plane and images of a 35 mm by 35 mm region of the flow are taken. The light scattered by the droplets is captured over a black background. The images are then processed to extract

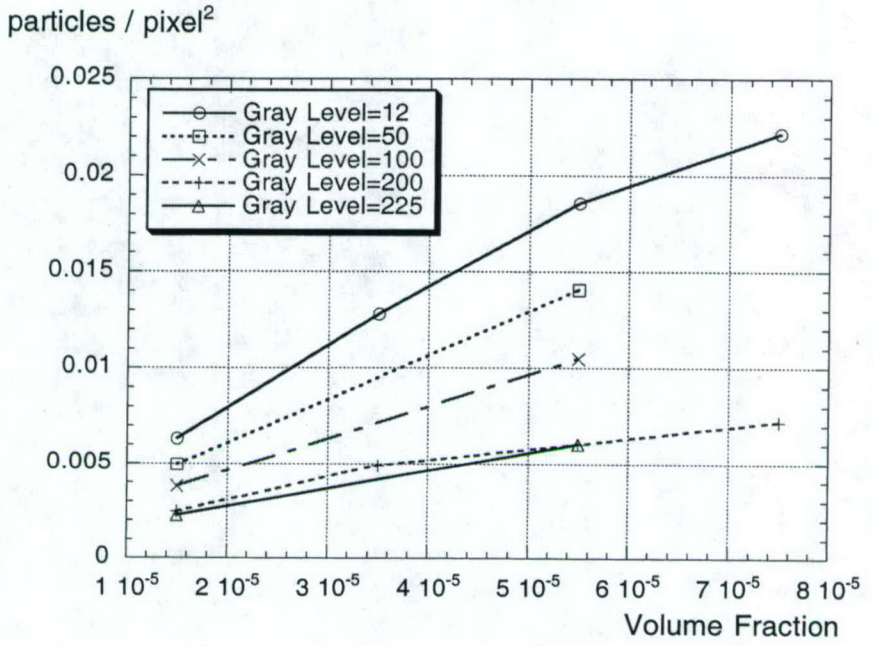

Figure 2.12: Average number of particles per pixel. Effect of the threshold.

information about the spatial location of the particles in the flow.

Using NIH image processing software, the images were made binary and processed. By thresholding the data with different light intensities, the noise due to multiple reflections, current leakage from saturated pixels or microlense spreading can be rejected. However, strict thresholds reject small particles which create dim reflections in the images. The sensitivity of the measurements to the threshold was systematically analyzed and found to be negligible in the range used in our experiments. The number of droplets per image, which can be observed in figure 2.12, decreases as the threshold is raised, as could be expected. However, the number of droplets in an image increases linearly with the volume fraction which ensures that the statistics based on the relative concentration, C/C_0, are unbiased.

During the image processing, each particle is reduced to a single pixel located at its centroid. A representative raw image and its processed binary image are shown in figure 2.13, where the presence of preferential accumulation of particles can be observed. Information on the preferential accumulation of particles

obtained with this processing method is presented in section 3.2.

2.2 Experimental results

Simultaneous measurements of the size and vertical velocity of the droplets were taken at 100 and 200 cm downstream from the injection grid. Large data sets (10^6 droplets) were acquired for each water mass loading. The data was divided into eleven bins, according to the diameter of the droplets. Each bin was characterized by the Stokes number computed using the average diameter in the bin. At the x=100 cm downstream station, where most of the experimental data was collected, particles with a diameter of 30 μm have a Stokes number equal to 1 and a corresponding terminal velocity ratio equal to 0.6.

2.2.1 Enhancement of the settling velocity

In this section we report the measurements of the mean vertical velocity of the droplets and its dependency on both the turbulence characteristics and the droplet volume fraction.

The instantaneous vertical velocity of all particles in each size class was averaged to compute the mean value of the settling velocity of particles of that size. This settling velocity is computed in an Eulerian sense, by averaging measurements of different particles taken at a fixed point. The Lagrangian settling velocity measured by following the trajectory of a particle is also of interest, but unfortunately could not be computed in this study where the number of particles present in the flow is too large to track individual ones. The settling velocity of particles in a still fluid, hereafter called Stokes velocity (V_{St}), is subtracted from the averaged settling velocity measured, and the difference is non-dimensionalized with the RMS of the carrier flow (u'). This dimensionless quantity has been proposed by Wang & Maxey (1993*a*) to characterize how the turbulence enhances the settling velocity of particles of different sizes. Plots of the non-dimensional increase

a)

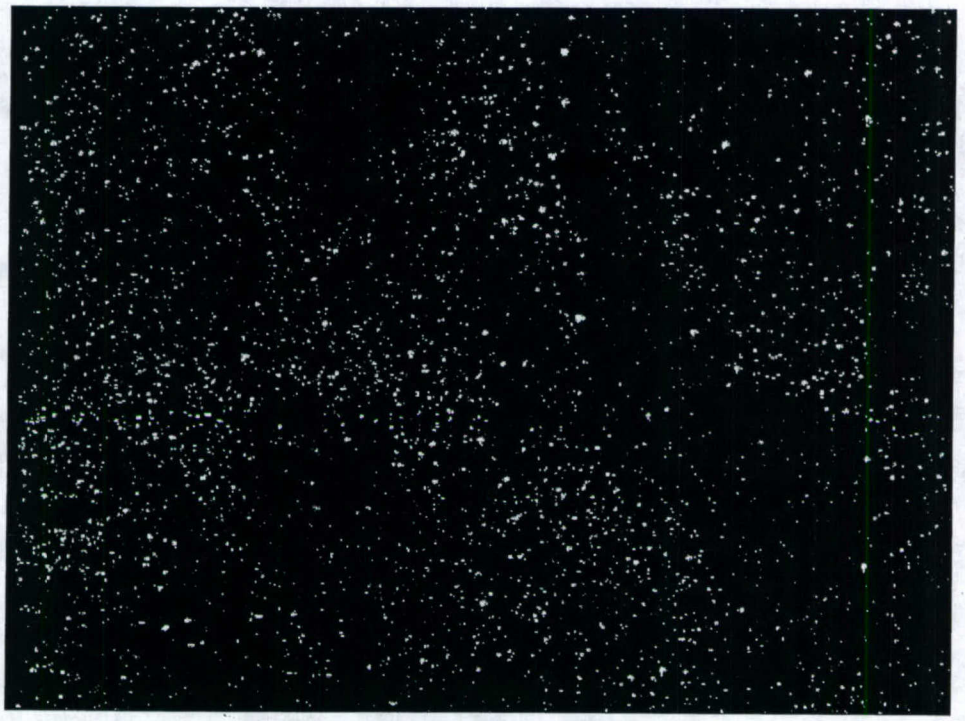

b)

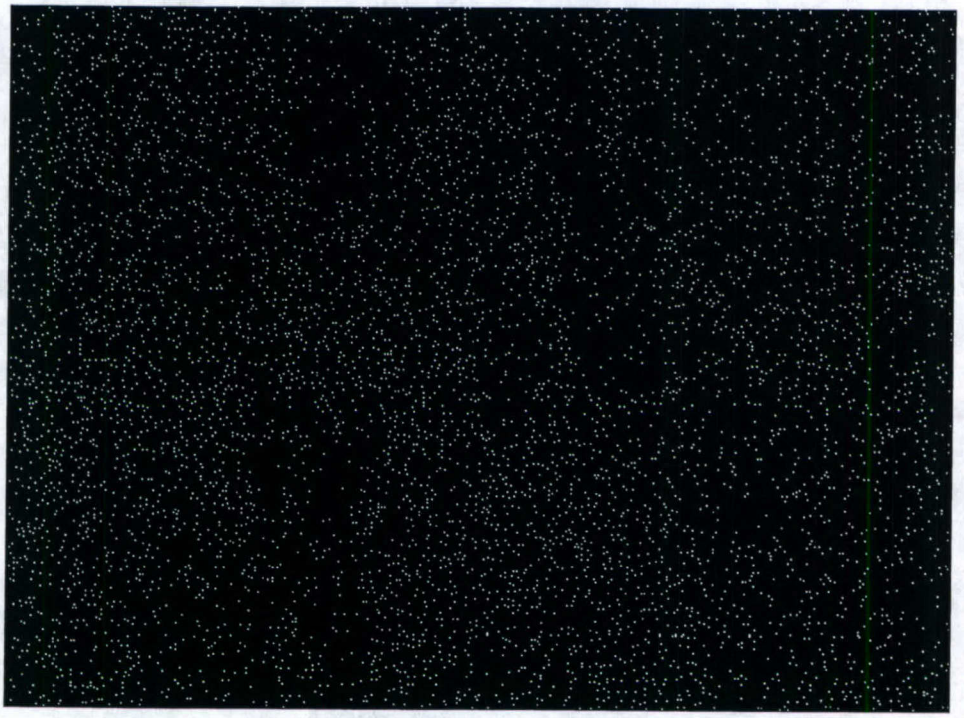

Figure 2.13: Flow visualizations. *a)* Raw image. *b)* Processed binary image.

a)

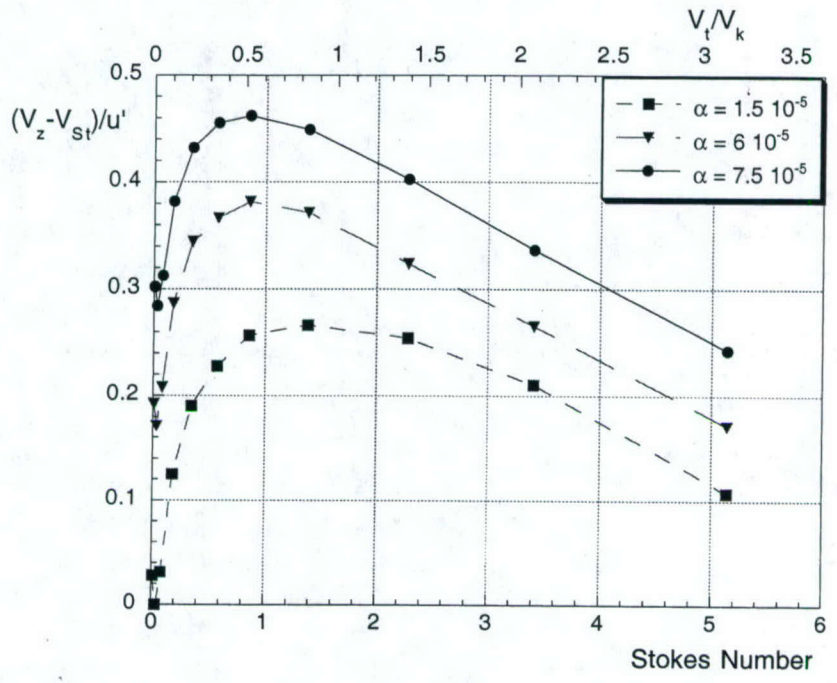

b)

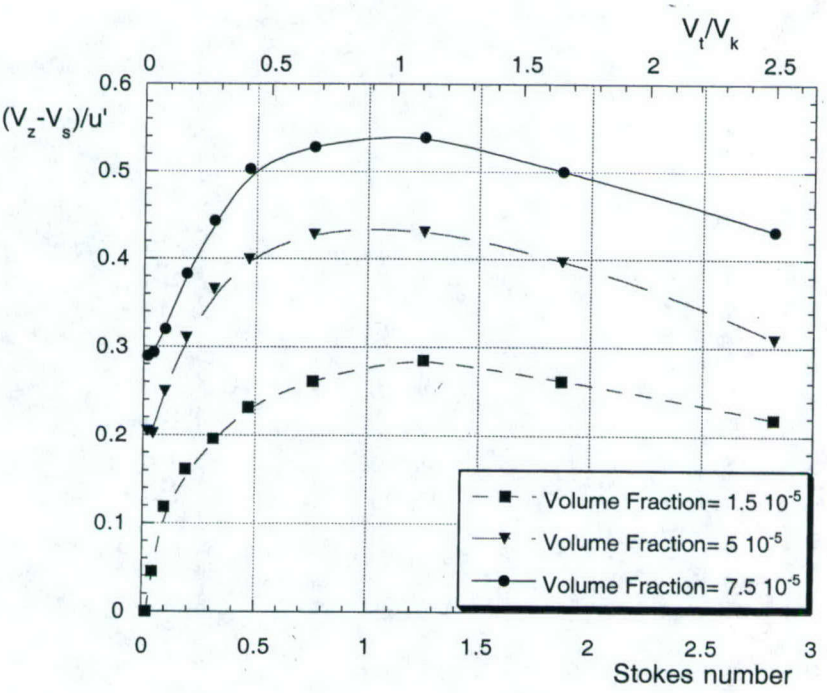

Figure 2.14: Increase in the settling velocity of particles as a function of their Stokes number, for different volume fractions. (*a*) x=100 cm. (*b*) x=200 cm.

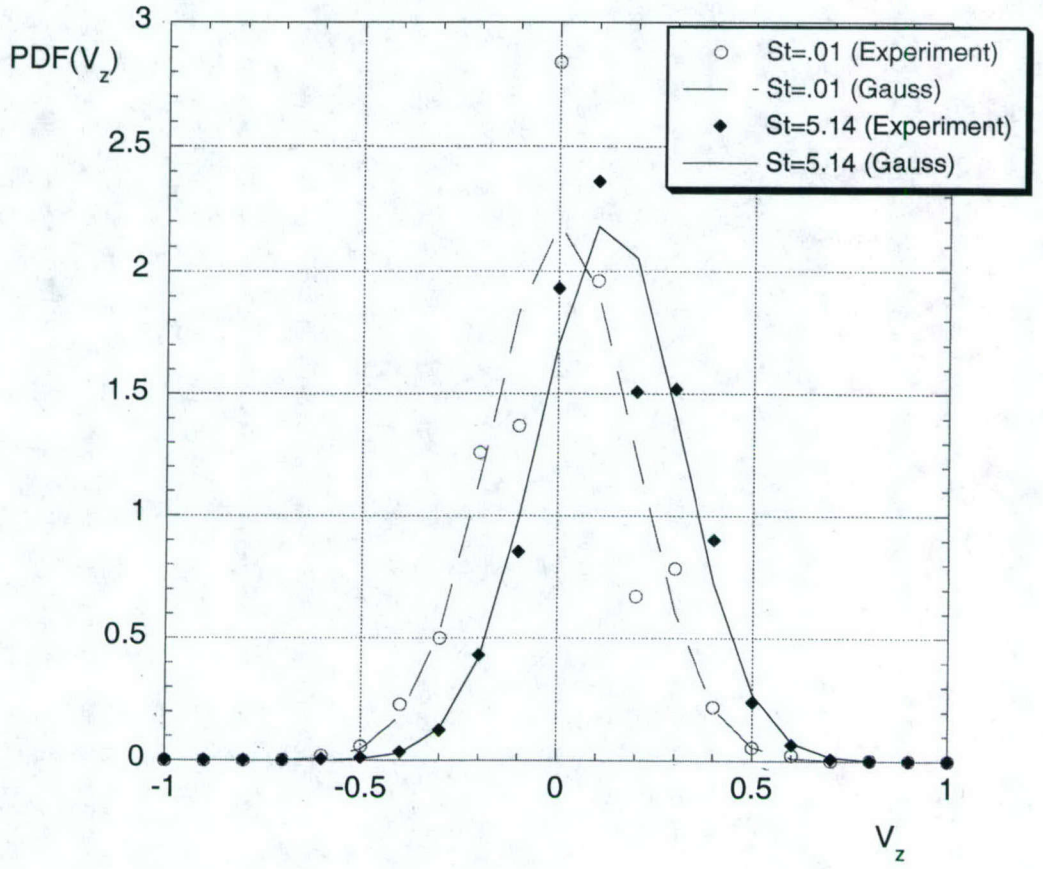

Figure 2.15: Probability density function of the vertical velocity measurements. $\alpha = 7.510^{-5}$, x=100 cm.

of the settling velocity at two different downstream locations, as a function of the Stokes number, are shown in figure 2.14.

Results for different values of the droplet mass loading or, equivalently, dispersed phase volume fraction (α) show the same qualitative behaviour. The variation of the increase in the settling velocity with the Stokes number is similar for all cases, exhibiting a maximum in the neighbourhood of Stokes ≈ 1. There is also a common tendency to decay to zero as the Stokes number becomes either zero or infinity. This can be easily explained by considering that the Stokes number measures the tuning of the response time of the particle to the excitation by the turbulence. Particles with Stokes number equal to one have the optimal

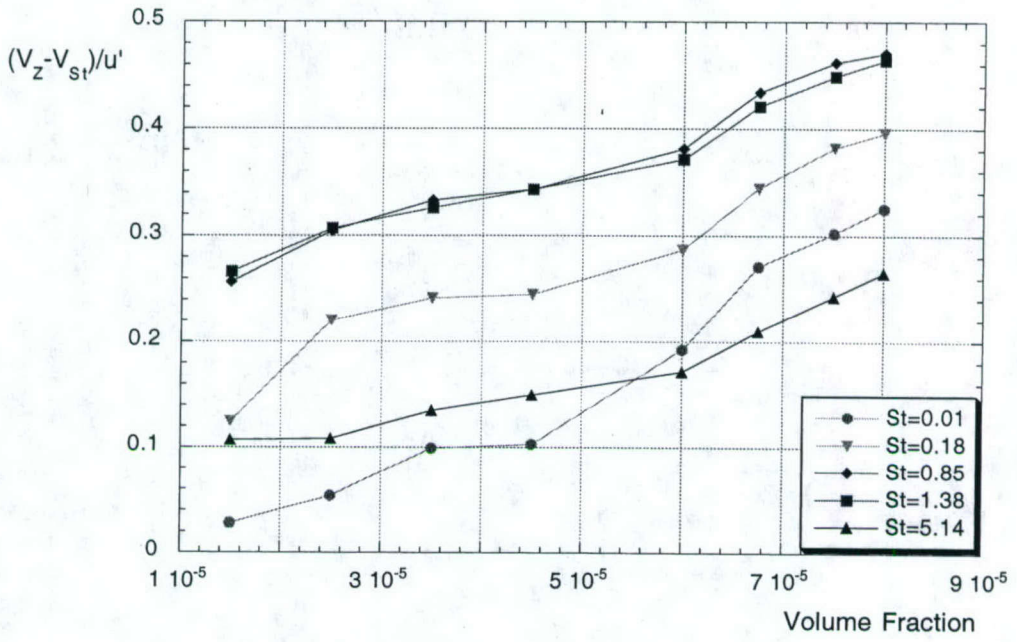

Figure 2.16: Effect of the volume fraction on the settling velocity enhancement, for different particle's sizes. x=100 cm.

sensitivity to the inertial bias caused by the turbulence. Very big particles, with large Stokes numbers, fall through the turbulent structures without responding to their fluctuations in velocity, due to their large inertia and short interaction time. Very small particles, on the other hand, have very small inertia (very small Stokes numbers) and long interaction time, and they follow the flow completely. Thus, their *average* settling velocity is zero. The PDF of the velocity measurements was found to be close to a Gaussian distribution, see figure 2.15. This seems to discard any possible bias in the sampling and indicates that the velocity enhancement is statistically significant for all the particles, so the mean velocity is a good measure of the long time settling behaviour of the particles.

The magnitude of the enhancement of the velocity was, however, found to be very different for the different values of the particle volume fraction studied. When the volume fraction increases, the settling velocity enhancement increases, and this was found to be true throughout the entire range of Stokes numbers at

both downstream locations. To better appreciate this trend, we show in figure 2.16 the non-dimensional settling velocity increase plotted versus the droplet volume fraction in the flow, with the Stokes number as a parameter. It is apparent from this plot that there is a monotonic increase in the settling velocity enhancement with the volume fraction of droplets in the flow. It must be emphasized that the range of volume fractions used in all the experiments reported here is such that the turbulence is not significantly affected by the presence of the particles, Eaton (1994), Elghobashi & Truesdell (1993), so this mechanism of turbulence modification by high particle volume fractions can be discarded as the mechanism responsible for the observed enhancement in Vz.

2.2.2 Clustering of particles due to turbulence

Turbulence has the effect of preferentially concentrating heavy particles, producing spatially non-homogeneous distributions, even if the particles are homogeneously injected in the flow. This effect, which leads to the formation of high local concentration regions, known as clusters, has been well documented by the numerical simulations of Squires & Eaton (1991*b*), Wang & Maxey (1993*a*) and Yang & Lei (1998), among others, and has been experimentally observed in monodisperse systems by Fessler *et al.* (1994). The relation between the preferential concentration of particles and their settling velocity enhancement has been investigated in the present study.

To study the characteristic dimensions of the clusters in the flow, the local concentration probability density function can be compared with that arising from a purely random process. Images of horizontal and vertical cross cuts of the flow were taken at different locations downstream from the injection. The concentration PDF was obtained by dividing an image into boxes of a certain size and counting the number of particles inside each box. The distribution of particles in boxes for a random process is given by a binomial distribution, equation 2.3. This distribution tends to a Poisson distribution, equation 2.4, when both the number of particles

and the number of boxes tend to infinity. For large volume fraction cases where the number of particles is too large to compute the binomial distribution analytically, we used the latter.

$$P_{binom}(n) = \begin{pmatrix} N_p \\ n \end{pmatrix} \left(\frac{1}{N_b}\right) \left(1 - \frac{1}{N_b}\right)^{N_p - n} \tag{2.3}$$

$$P_{poisson}(n) = \frac{e^{-\lambda} \cdot \lambda^n}{n!} \tag{2.4}$$

where λ is the mean number of particles per box, N_p/N_b, and P(n) is the probability of finding n particles in a box.

The comparison between the PDF found for a given box size and the random process provides us with an indication of how turbulence affects the particle concentration field. We have used two parameters to compare the measured PDF to the random distribution. The first one, hereafter referred to as D_{sum}, was used by Wang & Maxey (1993*a*) to analyze their DNS results. It is defined in equation 2.5 and represents the square of the difference of probabilities given by the two distributions. It is, by definition, always positive or zero,

$$D_{sum} = \sum_{n=1}^{N_p} (P(n) - P_{binom}(n))^2. \tag{2.5}$$

The second parameter, hereafter referred to as D_{sigma}, was introduced in Fessler *et al.* (1994), and is the difference between the standard deviation of the two distributions. Positive values of this parameter indicate the presence of concentrated regions, while negative values represent a quasi-uniform concentration field that is close to a Dirac's delta probability distribution,

$$D_{sigma} = \frac{\sigma - \sigma_{binom}}{\lambda}. \tag{2.6}$$

The length scale for which preferential concentration is most effective can be identified by computing these statistics for boxes of different sizes. Figure 2.18 shows the results of computing these two parameters, D_{sum} and D_{sigma}. It can be

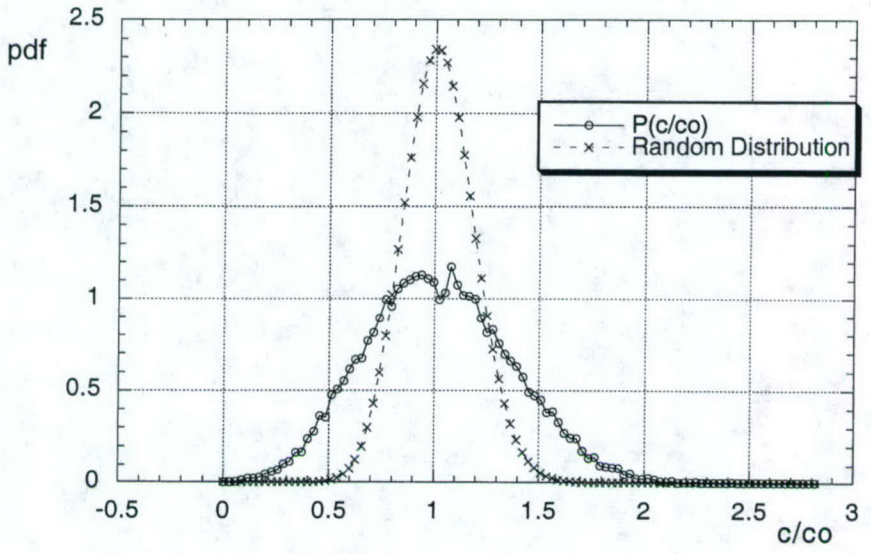

Figure 2.17: Probability density function of the number of particles per box. Total number of particles N_p, number of boxes N_b, $C_0 = N_p/N_b$.

seen that both parameters reach a maximum value at the same location. Furthermore, we also found that this result is insensitive to the details of the processing, namely the threshold. The maximum was consistently located at values of the box size around 10η, for all volume fractions used in the experiments. The suggested scaling of the location of the maximum with η seems to indicate that a characteristic length scale for the regions where particles accumulate due to turbulence (clusters) should be related to the smallest scales of the flow. Therefore, particle clusters seem to be under the influence of viscous effects.

In order to achieve a better understanding of the structure of the clusters, local concentration maps were produced by counting the number of particles inside a circle centered at each point. The radius was fixed at 3η which was found to be a good compromise between the spatial resolution and accuracy on the concentration measurements. An example of these concentration maps is shown in figure 2.19. Within these maps there are regions of very high concentration, relative to the mean. Determining the extent of these regions is of major importance if one wants to quantify the influence of local concentration on the settling velocity.

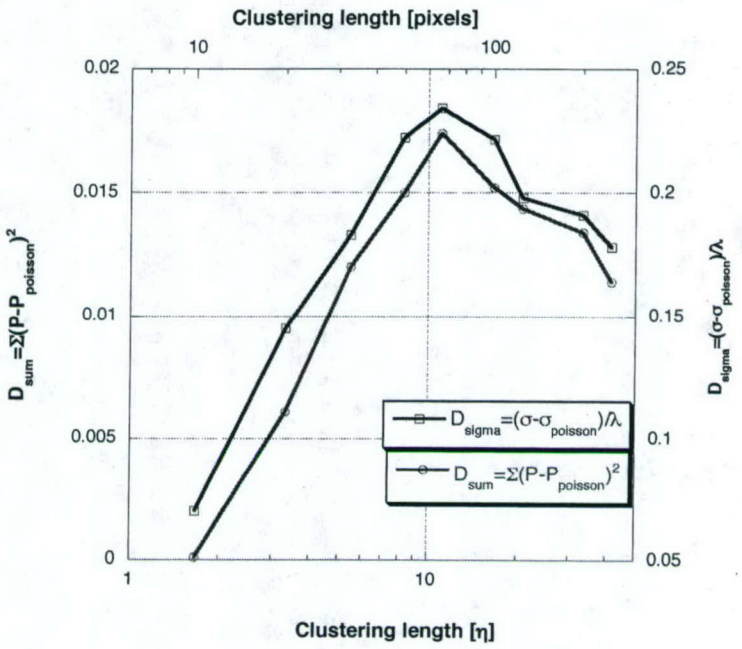

Figure 2.18: Two estimates of the distance between the PDF of particles in the flow and that of a random process. Evolution with the length scale.

Clusters are thereafter defined from iso-concentration contours, as regions where the concentration is higher than a prescribed level. In parallel with the analysis of scalar mixing of Catrakis & Dimotakis (1996), these will be referred to as level sets. The objects identified from this analysis are then characterized by their perimeter, P, their area, A, and the concentration level, $C_{cluster}$. The relationship between the perimeter and the area of the clusters is shown in figure 2.20. When the perimeter of the clusters is plotted versus the square root of the area, both scaled with η, one can observe two different behaviours. When the structures of the clusters are small and 'compact', P and $A^{1/2}$ are linearly related, whereas larger cluster structures exhibit a fractal nature. This fractal nature has been reported previously by Hogan *et al.* (1999), from numerical simulations, and by Fessler *et al.* (1994), from experiments. These features were found to be always present for the different level sets studied. Thus, one can conclude that either the perimeter or the area can be used, in a first approximation, to characterize

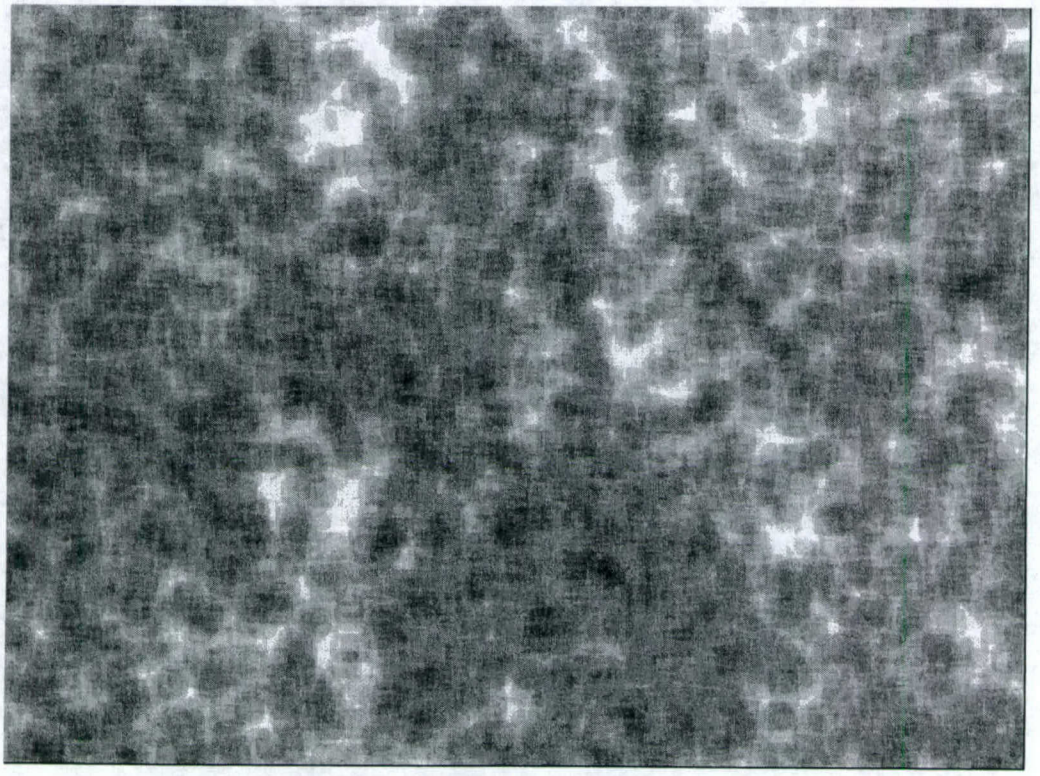

Figure 2.19: Local concentration map. From the image shown in figure 2.13.

the dimension of the clusters. We have used the area in figure 2.21 to study the occurrence of clusters in the flow. The number of structures of a given size was computed for a set of images, at different levels of concentration. For a given level set, the number of clusters of a given area was found to decay exponentially with size. Moreover, the argument of the exponential was found to increase with the concentration, indicating that the dimension of the clusters decreases drastically as the concentration level is increased.

Another important measure of the dimensions of the cluster can be obtained by examining the environment that the particles find. By computing the cumulative amount of particles contained in regions of a certain size and concentration, the cluster thickness as seen by the particles can be estimated. Figure 2.22 shows such a plot. It can be observed that about 50% of all particles are found in regions with a characteristic thickness between 7 and 16 η and where the concen-

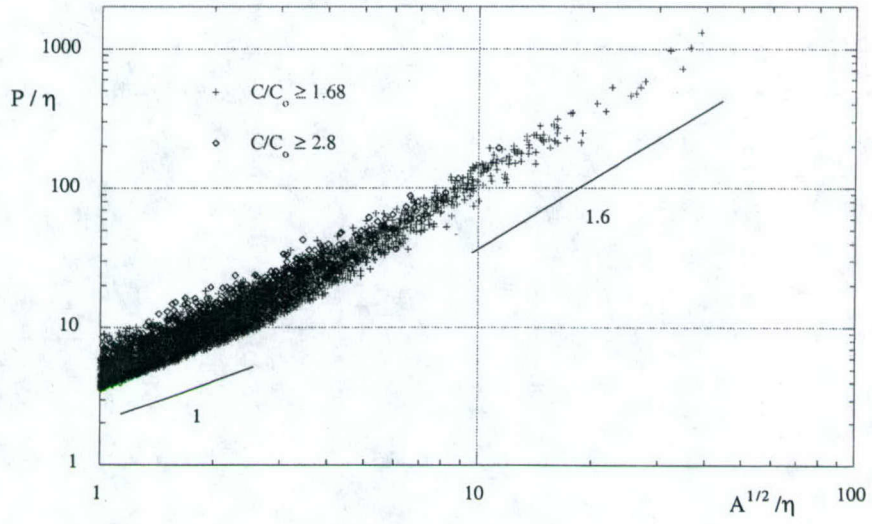

Figure 2.20: Perimeter vs. square root of the area of clusters for two different level sets.

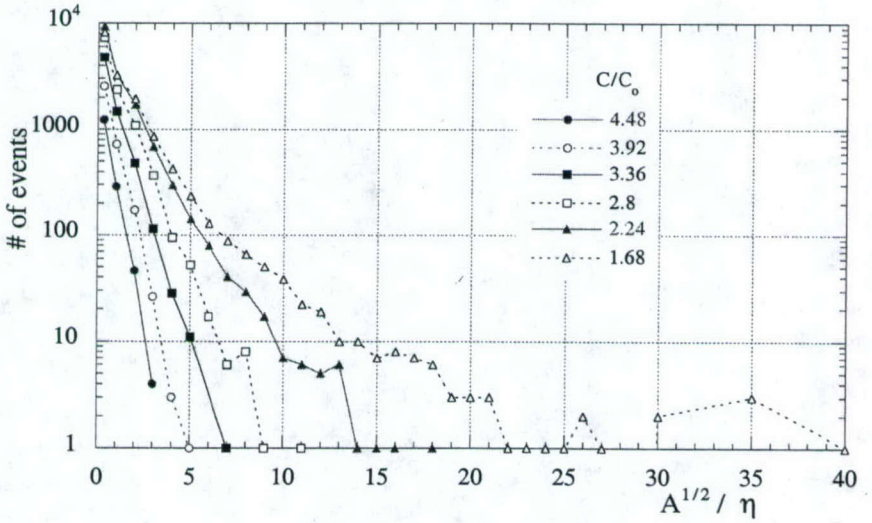

Figure 2.21: Number of clusters of a given area, for different concentration levels. Volume fraction=5 10^{-5}. x=100 cm. 30 images processed.

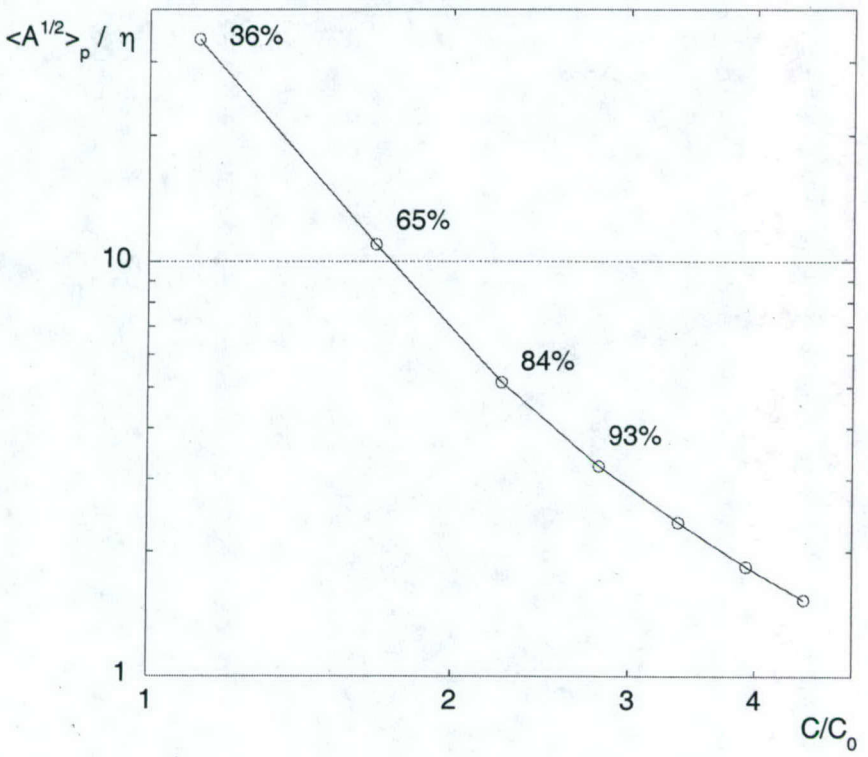

Figure 2.22: Typical cluster thickness as seen by the particles.

tration is between 1 and 2.5 times the mean. This information strongly supports the finding that the significant thickness for particle accumulation regions is of the order of 10η.

2.2.3 Measurements of the settling velocity of the particles conditioned to the local concentration

Measurements of the local concentration of particles in the flow were also obtained from the PDPA data presented earlier in this section. The PDPA data consists of four fields recorded for each droplet that crosses the interrogation volume. Those fields are: diameter, horizontal velocity, vertical velocity and time of arrival. The positions where the measurements were taken are at a sufficient distance downstream from the injection to ensure that all droplets have reached the horizontal velocity of the flow with fluctuations smaller than or equal to those

of the single phase flow ($\approx$ 2% of the mean). Therefore, the inter-arrival time between particles can be related to the inter-particle distance by using the mean horizontal velocity of the flow. The local concentration around a particle can then be computed by counting the number of particles that are within a given distance of the particle of interest. However, PDPA concentration measurements suffer from several effects that bias these results, making it extremely difficult to obtain absolute concentrations, Sommerfeld & Qiu (1995). Thus, we did not attempt to conduct these measurements. Instead, the experimental settings were optimized for maximum data rate while preserving the proportionality with the droplet volume fraction. In this way reliable relative concentration, C/C_0, measurements were obtained. Using the information from the image processing about the size of the preferential concentration regions, the number of particles within 10η of each particle were counted. Particles were classified according to the number density found around them and statistics were computed for these groups.

In figure 2.23 we plot the probability of finding particles of a given size in a region of a certain local concentration compared to the probability of finding a particle of that size over the entire flow. Observe that particles with $S_t \approx 1$ accumulate more efficiently and are less likely to be found in regions of low concentration, whereas small and large particles are found in those regions in proportions larger than the average. The opposite is true for high concentration regions, although the difference in relative probabilities is much smaller. The composition of the clusters is very similar to the injected distribution, the probability of finding particles with $S_t \approx 1$ is slightly increased and the probability of particles with $S_t << 1$ or $S_t >> 1$ is slightly decreased. Those small probability surpluses and deficits found in high concentration regions, balance the larger differences in probability at lower concentration, where the number of particles is much smaller.

The same conditioning technique was used to process the vertical velocity data. Averaging the vertical velocity of all particles found in regions of a given concentration, the influence of the local concentration in the settling velocity of

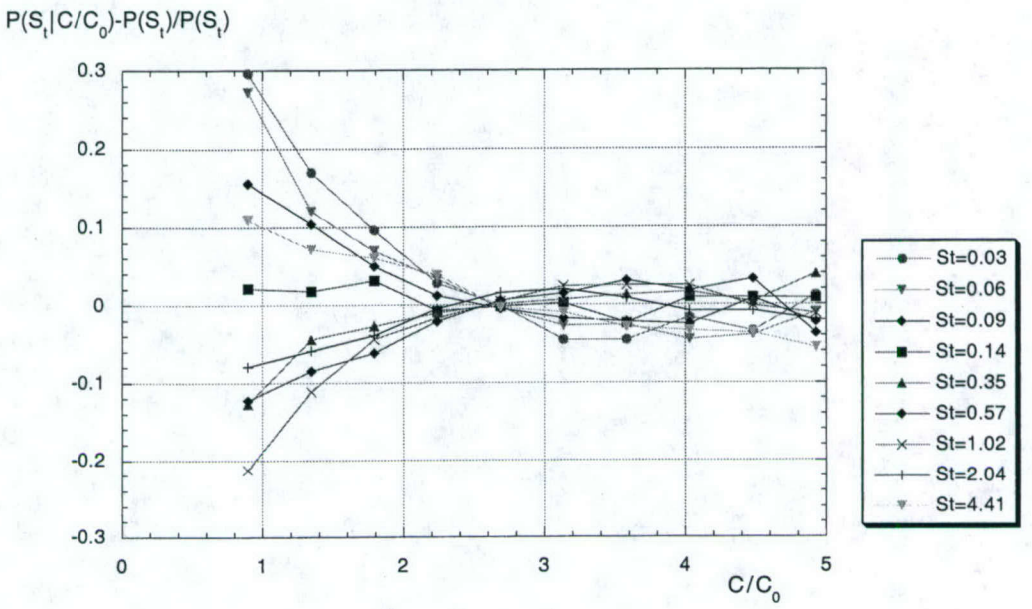

Figure 2.23: Preferential concentration of particles, for different Stokes number. Size PDF conditioned to the local concentration, compared to the overall size PDF of the flow. x=100 cm, $\alpha = 7.5\ 10^{-5}$.

particles was studied. Figure 2.24 shows the results from this processing for two different volume fractions of particles at downstream locations x=100 cm and x=200 cm. The difference between the averaged settling velocity of particles of a given size conditioned by a given concentration and the velocity of particles of that same size class averaged over all concentrations is plotted versus the local concentration. The tendency of the settling velocity to increase as the local concentration increases is evident, and this dependency is almost linear, within the range studied. The fact that curves for all sizes collapse indicates that the mechanism responsible for this increase is most probably a collective effect.

2.3 Analysis and discussion of the results

The experimentally determined settling velocity enhancement of particles in a turbulent flow, shown in figure 2.14, exhibits all the qualitative features

a)

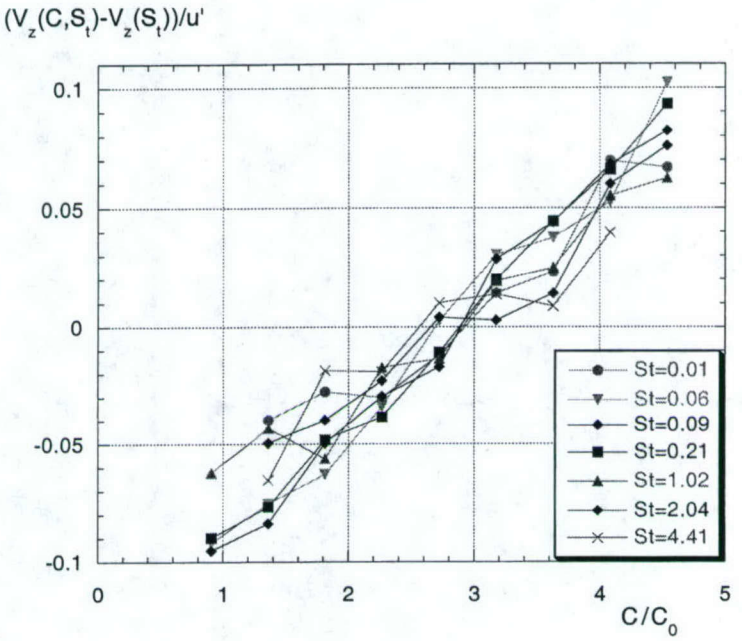

b)

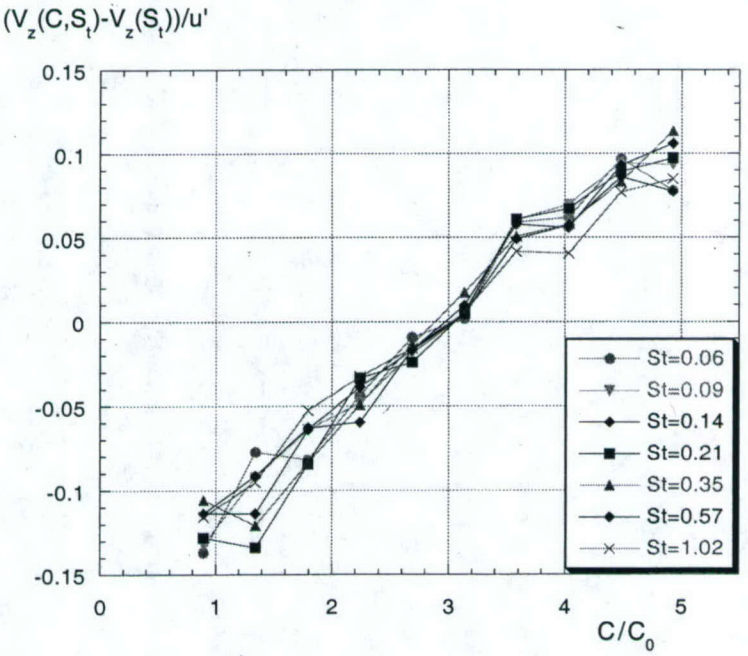

Figure 2.24: Enhancement of the settling velocity as a function of the local concentration. *a)* x=100 cm, $\alpha = 6\ 10^{-5}$. *b)* x=100 cm, $\alpha = 7.5\ 10^{-5}$. *c)* x=200 cm, $\alpha = 5\ 10^{-5}$. *d)* x=200 cm, $\alpha = 7.5\ 10^{-5}$.

c)

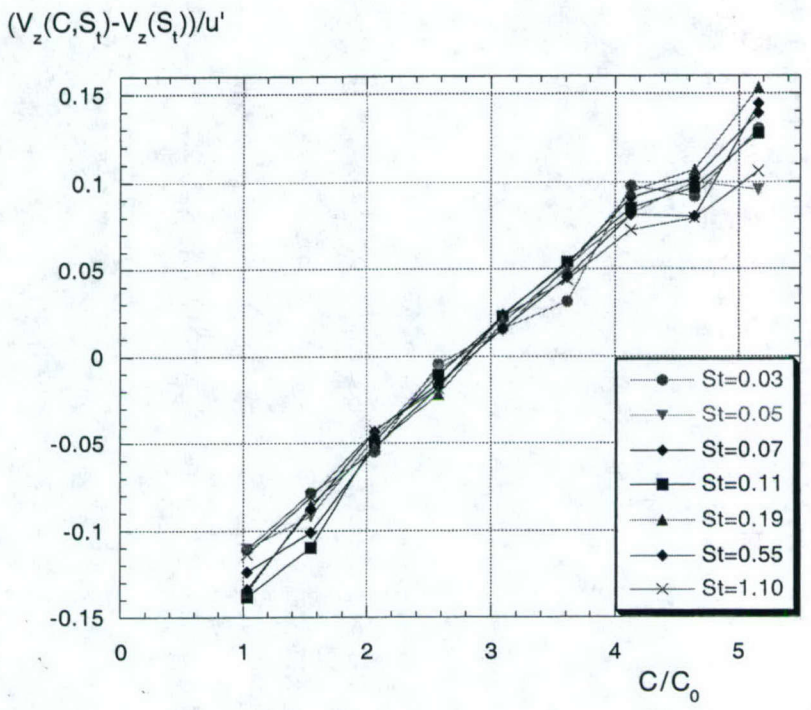

d)

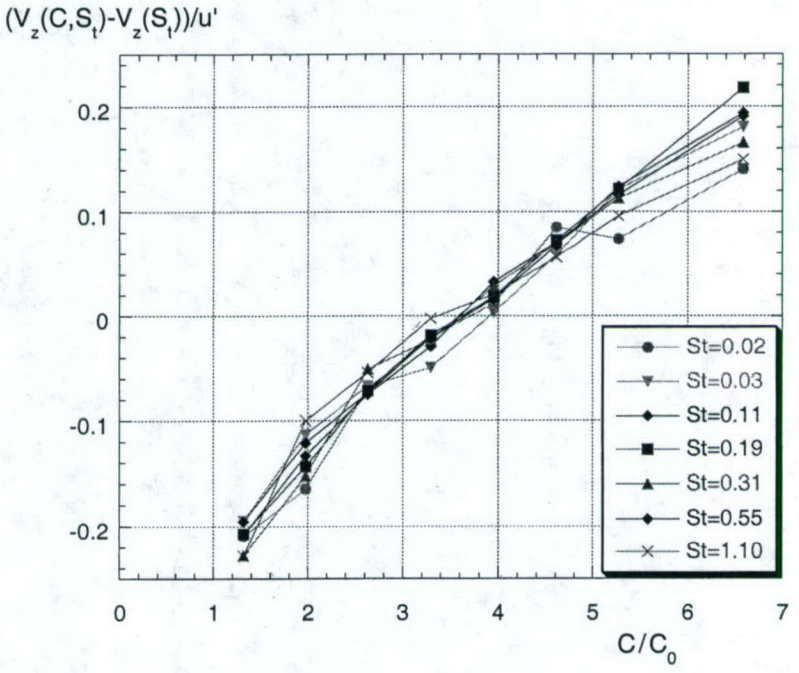

Figure 2.24: continued

shown in the DNS of Wang & Maxey (1993*a*). As in Wang & Maxey's simulation, the vertical velocity enhancement plots have a well defined maximum consistently located near $St \approx 1$. There are, however, quantitative differences between the values measured in our experiment and the ones computed in Wang & Maxey's simulation. It has to be kept in mind that the simulations were done without any mechanism by which one particle could feel the presence of the others, thus they can only be compared to our results in the limit of zero volume fraction. Furthermore, the simulations were done at Reynolds numbers lower than our experiment, and they showed a weak dependency of the settling velocity enhancement with Re_λ. However, considering these differences, the simulations compare well with the measurements in the smallest volume fraction case. For the higher volume fractions, the experimental values of the increase in the settling velocity are significantly larger than the simulated ones. Since, for the range of concentrations used, the enhancement in the experimentally determined settling velocity increases monotonically with the volume fraction in the flow, we explored the possibility that the preferential accumulation of particles could be responsible for this behaviour. This in turn would explain the discrepancy with the simulations where the increase in the settling velocity due to turbulence is computed without any influence of the particles on each other, and is independent of the volumetric fraction of particles in the flow.

We have already mentioned that the maximum increase of the settling velocity is always found for particles whose Stokes number is close to one. This supports the scaling argument we introduced when we defined the Stokes number in terms of the Kolmogorov velocity. On the other hand, we can not shed any new evidence on which should be the correct scale for the velocity increase. Although we have chosen to scale it with u' and the resulting non-dimensional increase varies only slightly as the flow conditions change between x=100 cm and x=200 cm, the velocity scales u' and V_k evolve similarly as the turbulence decays, as seen in table 2.1. Unfortunately, there is not enough dynamic range in our experiments

to study which would be the correct scale for the settling enhancement.

Results from the two different downstream locations are very consistent. The main difference between the conditions at these two stations is that, as the turbulence dissipation rate decays, the ratio V_t/V_k decreases compared to the Stokes number of the particles. In the x=200 cm case, particles with $S_t \approx 1$ also have $V_t/V_k \approx 1$ and the value of the maxima are found to be larger than in the x=100 cm case, where the maximum occurs at $V_t/V_k \approx 0.5$. This influence of the terminal velocity ratio, although weak, agrees with the previous findings that suggest values of V_t/V_k between 1 and 2 as optimum for the settling velocity enhancement.

Despite the random nature of turbulence, the distribution of particles in a turbulent flow is far from random. In fact, it exhibits large intermittency in the temporal and spatial concentration fields. Inertial bias creates a tendency for heavy particles to accumulate in regions of high strain rate and low vorticity. This tendency induces the creation of clusters of particles and those clusters are denser and more numerous as the volume fraction of particles in the flow increases. Both tendencies are supported by our experimental findings, namely in figure 2.24 the value where the lines cross the abscissa (local concentration for which the velocity corresponds to the average velocity) is larger for larger volume fractions.

Clusters are regions of relatively high concentration formed when particles accumulate in regions of low vorticity and high strain. As a number of particles come close enough they start to interact through the surrounding fluid, and no longer react to the turbulence independently. This region where the particles locally perturb the flow and interact with each other is what we call a cluster. Once formed, the cluster continues to settle entraining other particles. Those particles will see their vertical velocities enhanced and they will increase the relative density of the cluster, thus increasing its settling velocity. Eventually, the interaction with another turbulent structure will disperse the particles, ending this feedback process. The effect of these regions in the overall statistics of the flow is negligible, so they cannot be revealed in two-way coupling simulations by considering turbulence

modulation. However, this collective effect might be recovered in those simulations by studying the local perturbations of the carrier fluid velocity inside these high density regions, possibly through the modification of the pressure field.

Previous studies of preferential accumulation have been carried out in flows with mono-dispersed distributions of particles. These studies predict an important difference between accumulation of particles with Stokes number near one and those with Stokes number far away from unity. The results in figure 2.23 show a significant difference in the low concentration regions. However, as the local concentration increases, the difference disappears. The particle size distribution in our experiment is poly-dispersed and so the different behaviour could very well be explained if we consider that in this case particles of $S_t \approx 1$ accumulate preferentially and form clusters which then entrain particles of all sizes. In flows with mono-dispersed distributions, either all particles tend to accumulate, which makes the accumulation more evident, or they all tend towards a random distribution and clusters do not form. This hypothesis is consistent with the fact that the maximum values found in figure 2.18, where the spatial distribution is compared with a random one, are smaller than the values obtained when all particles are of the same size, Wang & Maxey (1993*a*) and Fessler *et al.* (1994).

In figure 2.21 we noted that the largest cluster areas are about 15η for $C/C_0 > 2.2$, and 7η for $C/C_0 > 3.4$, which is fully consistent with the maximum occurrence of clustering at 10 η shown in figure 2.18. However, that figure showed the presence of elongated structures, and thus of larger characteristics sizes. As the level of complexity in the description of the cluster structure increases, the analysis becomes more difficult. In figure 2.21 we observe that most of the clusters, especially those with higher concentrations levels, have an equivalent radius equal to or less than 10η. Also, in figure 2.20, one can observe that the clusters that most significantly affect the settling velocity are within the range where the perimeter and the square root of the area are linearly related.

When the cluster size calculated from the image processing was used

$x(cm)$	*Volume fraction*	$\frac{V_{is}-V_{St}}{u'}$	$\frac{\overline{V_z}(\alpha_{min})-V_{St}}{u'}$
100	$6\ 10^{-5}$	0.24	0.26
	$7.5\ 10^{-5}$	0.27	0.26
200	$5\ 10^{-5}$	0.26	0.28
	$7.5\ 10^{-5}$	0.26	0.28

Table 2.2: Settling velocity of isolated particles. $St \approx 1$.

to conditionally average the vertical velocity, we found a quasi-linear behaviour characterized by two parameters: the slope and the value at $C/C_0 \rightarrow 0$. The settling velocity that particles would have in isolation can be computed using the mean velocity from figure 2.14 and the slope and mean cluster concentration from figure 2.24. The results are shown in table 2.2.

$$V_{is}(S_t) = \overline{V_z(S_t, \alpha)} - \frac{\mathrm{d}V_z}{\mathrm{d}C/C_0}(\alpha) \cdot C/C_0(\alpha) \mid_{V_z=\overline{V_z}} \tag{2.7}$$

These values can be compared with numerical simulations and with experimental data in the limit of very small volume fraction. The comparison between the settling velocity for isolated particles ($St \approx 1$) predicted from the data in figures 2.14 and 2.24 and the measured velocity for the smallest volume fraction, from figure 2.14, is shown in table 2.2. The values found for isolated particles in high volume fraction flows, are remarkably similar to the mean settling of particles in the lowest volume fraction case (taken to be the limit in which the settling velocity of one particle is not influenced by the presence of other particles). This indicates that particles only perceive the local concentration in their vicinity and that they are unaware of the overall volume fraction in the flow, as long as the properties of the turbulence are not significantly altered. The slope of the settling velocity as a function of relative concentration can be related to the dynamics of the clusters. Table 2.3 shows the values of the slopes obtained when a linear fit was applied to the plots in figure 2.24. A preliminary effort to relate those values to the behaviour of the clusters is made in the next section.

2.4 A phenomenological model of the effect of preferential accumulation on the settling velocity of the particles

As mentioned in the introduction, it is already well known that particles accumulate in the downward side of the eddies and that their settling velocity is enhanced. This has been called the preferential sweeping effect and it has been well established both theoretically and from DNS results, Wang & Maxey (1993*a*). However, if preferential sweeping were the only effect, the increase in the settling velocity of particles would be independent of the number of particles in the flow, as long as that number were not large enough to attenuate the intensity of the turbulence or to promote collisions. Our experimental results shown in figures 2.14 and 2.16 clearly indicate that there is a dependency of the enhancement of the velocity on the volume fraction of particles in the flow. If particle accumulation becomes more important as more particles are added to the flow and the enhancement of the settling velocity also becomes larger as the volume fraction increases, it is reasonable to hypothesize that there ought to be a correlation between the formation of particle clusters and the settling velocity of the particles.

It could be argued that the velocity increase with the local concentration is just an effect of the correlation between the regions of high concentration and the downward side of the eddies. Particles in regions of high concentration are also most likely to be in the downward side of the eddies and, when averaged, the resulting settling velocity is larger than the overall mean. This argument, which arises from the point of view of particles interacting with an isolated, horizontal vortex, fails to explain the phenomenon when turbulence is isotropic and eddies do not have a preferential orientation. Moreover, the increase with the volume fraction can not be explained by this argument.

The idea that clusters play an important role in the settling of particles, supported by the result shown in figure 2.16, led us to develop a simple phenomenological model to estimate the settling velocity of particles, while inside a cluster,

as the sum of two terms.

$$V_z = V_{is} + V_{cluster} \tag{2.8}$$

The first term is the settling velocity that isolated particles would have in a turbulent flow. This term is formed by the Stokes velocity that particles would have in a quiescent fluid plus the enhancement due to the preferential sweeping by turbulence. It can be observed in the limit of very low volume fraction of particles in the flow and has been computed in direct numerical simulations, Wang & Maxey (1993*a*).

The second term in the equation is due to the effect that clusters have on the settling velocity of particles inside them. In order to estimate this second effect, which has not been addressed before, we model the clusters as large pseudo-particles with a characteristic size l and a mean density ρ_{cl} given by the local concentration of particles in them, $\rho_{cl} = (1 - c) \cdot \rho_{air} + c \cdot \rho_p$. Further assuming that clusters are inside the viscous domain (the Reynolds number of the clusters is at most of order 10), the interaction with the surrounding carrier fluid can be expressed in the form of a simple Stokes drag law. The equilibrium between the weight of the cluster and the drag exerted by the fluid will give us an estimate of the terminal velocity of the cluster as a function of its concentration

$$(\rho_{cl} - \rho_{air}) \cdot \frac{\pi \cdot l^3}{6} \cdot g = \frac{1}{2} \cdot \rho_{air} \cdot V_{cl}^2 \cdot \frac{\pi \cdot l^2}{4} \cdot C_D \tag{2.9}$$

where V_{cl} is the settling velocity of the cluster.

The velocity of the clusters is then:

$$V_{cl} = \frac{K_T}{18} \cdot \frac{\rho_p}{\rho_{air}} \cdot \frac{g}{\nu_{air}} \cdot C \cdot l_{cl}^2 \tag{2.10}$$

where K_T depends on the volumetric shape factor, Clift & Weber (1978), and it ranges between 0.3-0.5 for long, thin structures, and equals 1 for spheres. It is important to note the linear dependency of this expression on the local concentration of particles, confirmed by the experimental results from figure 2.24. Thus,

		From the model	From figure 2.24	
$x(cm)$	α	$\frac{V_{cl}/u'}{c/c_0}$	$\frac{dV_z/u'}{dC/C_0}$	$C/C_0(V_z = \overline{V_z})$
100	$6 \cdot 10^{-5}$	0.051	0.052	2.81
	$7.5 \cdot 10^{-5}$	0.063	0.065	3.05
200	$5 \cdot 10^{-5}$	0.053	0.068	2.95
	$7.5 \cdot 10^{-5}$	0.074	0.102	3.84

Table 2.3: Settling velocity dependency on the local concentration.Comparison between model and experiments.

we can rewrite equation 2.8 as $V_z = V_{is} + m \cdot C/C_0$, where m corresponds then to $dV_z/dC/C_0$. Using the experimental value of l_{cl}, the characteristic length of the clusters, one can estimate the ratio between the cluster velocity and the RMS of the flow velocity as a function of the relative concentration, that is the value of m. Despite the simplicity of the model, the results shown in table 2.3 are comparable to the experimentally determined slopes of the curves in figure 2.24, also given in the table.

The data in table 2.3 can be used to estimate the effect of clustering on the mean settling velocity of particles. According to this simple model, since the particle size PDF inside the clusters is roughly the same as in the overall flow, the effect is the same for particles of all sizes. That can be compared with the increase due to the volume fraction. Subtracting the settling velocity of the smallest volume fraction from the values for larger volume fractions in figure 2.14, also gives an estimate of how much of the increase in the settling velocity is due to clustering. Figure 2.25 shows those estimates for the four different cases in table 2.3. The model gives a good prediction of the effect for particles of $S_t \approx 1$, but over-predicts the effect for large particles and under-predicts it for small particles. The predictions are in good agreement with the experimental data, especially for the data taken at x=100 cm, which is where we measured the size of the clusters. However, the underestimate of the slope at x=200 cm may be due to the evolution of the cluster characteristic length, which has been assumed to be constant at all

a)

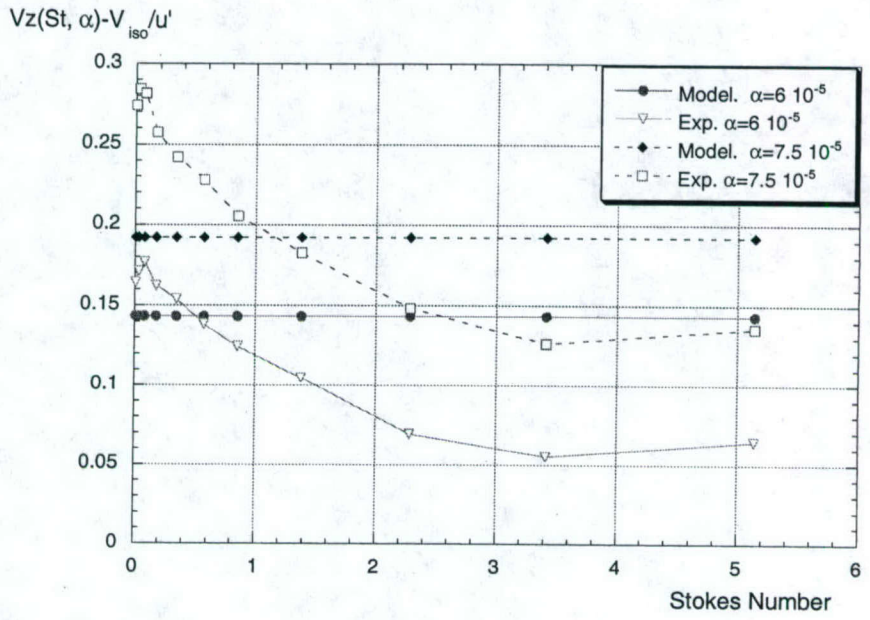

b)

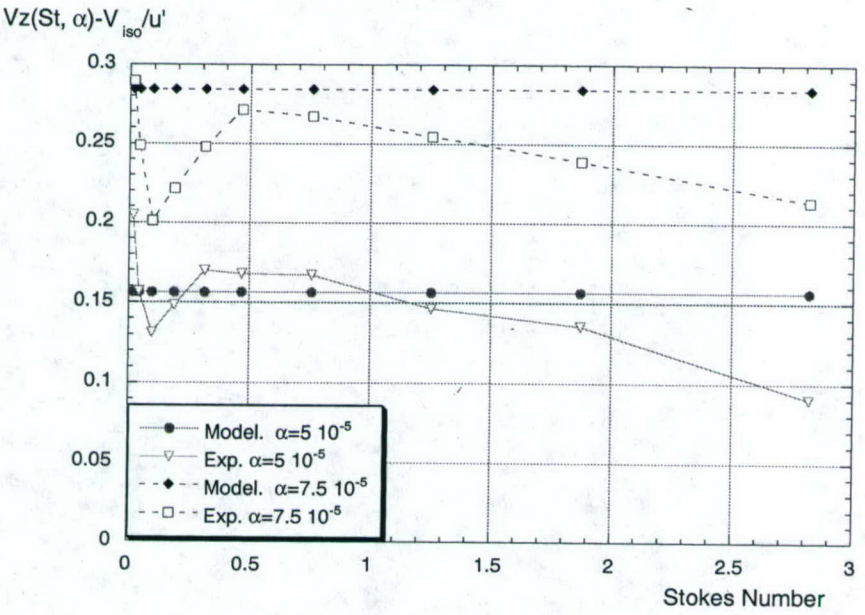

Figure 2.25: Effect of clusters on the increase in the settling velocity of particles as a function of their Stokes number. Comparison between model and experiments. (*a*) x=100 cm, (*b*) x=200 cm.

locations and equal to 10η. An assumption which needs further study.

It is worth noting that the proposed model does not provide the unconditional settling velocity. The fraction of time that a given particle remains under the influence of clusters is not known. One should introduce an intermittency factor, γ, to express the unconditional settling velocity as:

$$\overline{V_z(S_t, \alpha)} = V_{is}(S_t) + \int \gamma(S_t, \alpha, C) \cdot V_{cl}(C) \mathrm{d}C \tag{2.11}$$

Extracting γ from the above expression requires to account for the variability in the cluster structure, and such detailed information is not available from the experiments. If equation 2.11 is compared to equation 2.7, we can understand the value of $C/C_0(\alpha) \mid_{V_z=\overline{V_z}}$ as an integrated measure of the intermittency factor. The value of this parameter, the local concentration where the mean settling velocity is reached, is shown in table 2.3 to vary from case to case, increasing with the volume fraction.

2.5 Conclusions

Experiments were conducted to study the behaviour of heavy particles in homogeneous, isotropic, decaying turbulence. It has been shown that the settling velocity of the particles is enhanced by the turbulence, and the concentration field shows large inhomogeneities. These inhomogeneities were attributed to the preferential sweeping and to the preferential concentration of particles by the turbulent structures, two effects that have been predicted theoretically and simulated numerically but of which there had been little or no experimental evidence so far. The use of the Kolmogorov scales to formulate the parameters that govern the problem is supported by the location of maxima for values of the Stokes number and the terminal velocity ratio of order one. The correct scaling for the increase of the settling velocity is still an open question.

The concentration field of particles in the flow were studied by means

of image processing. Digital images of the flow were taken and analyzed in an effort to characterize the geometry of the concentration field. The comparison of the distribution of the number of particles in boxes of a certain size and the distribution in a random process (binomial/Poisson) unveiled a length scale where the concentration is most highly correlated. This length scale has been determined to be $O(10\eta)$ and can be interpreted as a characteristic cluster length. This result is in very good agreement with length scales for preferential accumulation found in previous experiments, Fessler *et al.* (1994).

A dependency of the settling velocity enhancement on the particle volume fraction. that can not be explained in terms of the behaviour of isolated particles in a turbulent flow. has also been found. A new mechanism to explain the effect of the number density of particles on the settling velocity of a neighbouring particle has been proposed. Conditional measurements of the settling velocity as a function of the local concentration of particles support the hypothesis that regions of high concentration are formed and behave as large pseudo-particles that we call clusters. These clusters settle in the lower density fluid surrounding them with their own velocity, which adds to the settling velocity of the particles inside them. By comparing the velocity conditioned to the local concentration with the unconditional velocity, and scaling them with a characteristic velocity of the flow, be it u' or V_k, it was shown that all the measurements collapse. The result is a linear function for particles of all sizes, whose value at the origin gives the settling velocity of isolated particles, and whose slope gives the effect of clustering in the settling velocity of particles.

Finally, a simple phenomenological model has been formulated to address this behaviour. The terminal velocity of clusters can be computed using the characteristic cluster length found and assuming Stokes drag is applicable, and that value, which depends linearly on the local concentration, is added to the velocity for isolated particles. Given the simplicity of the model the predictions are in good agreement with the experiments, both in predicting the trend with the local

concentration and in the mean effect that clustering has in the enhancement of the settling velocity with droplet volume fraction.

Chapter 3

Preferential concentration and rise velocity reduction of bubbles immersed in a homogeneous and isotropic turbulent flow

3.1 Experimental methods

3.1.1 Experimental facility

The experiments were carried out in a recirculating water channel with a capacity of roughly five thousand liters. The free stream in the channel has a maximum speed of 1 m/s. The test section is 2 m. long and has a square cross section of 0.6 m x 0.6 m. A sketch of the facility is shown in figure 3.1. The facility has a series of grids and honeycombs, followed by a contraction, to assure that fluctuations originating at the pump are damped out before the flow reaches the test section. The underlying turbulent intensity is very low, less than 0.5 %, and the homogeneous isotropic turbulence is created by a grid located at the entrance to the test section. The grid was formed by cylindrical bars with a diameter of 1/8 in. and spaced 1 in., which gives a solidity ratio of 0.11. This, together with three

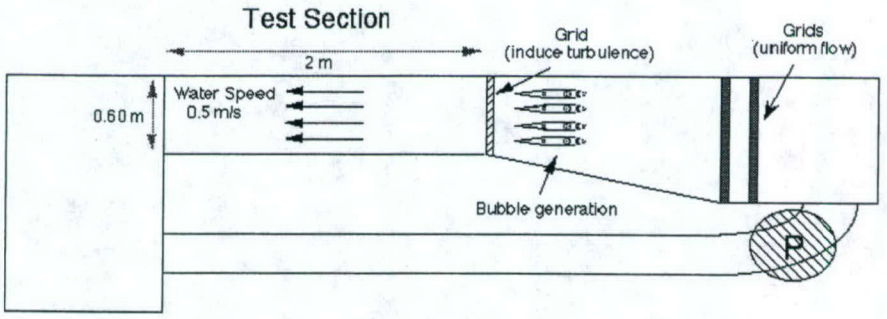

Figure 3.1: Recirculating water channel.

different mean velocities of the carrier flow enabled us to study the behaviour of the bubbles under different conditions of the turbulence.

The bubbles were introduced in the flow by an array of hydrofoils located a small distance in front of the turbulence-inducing grid. They were positioned horizontally and arranged in a grid type structure, separated 4 in. from each other and from the top and bottom of the channel, so the perturbation due to the bubble injecting device was just a small contribution to the overall turbulence. The injectors have been embedded in the hydrofoils to minimize their wakes. Each injector consists of an aluminum NACA 0012 profile with a longitudinal cavity machined along its leading edge. The cavity is closed with a porous plate through which compressed air, injected from the side of the hydrofoil, is bubbled into the incoming flow. The experiments required the injection of very small bubbles, $d_{32} \approx 200\mu m$, in very large numbers so that the volume fraction would be significant to study accumulation effects, $\alpha \approx 10^{-4}$. To further reduce the bubble size, ethanol micro-jets were directed at the porous plate along the leading edge of the hydrofoil so that the contact angle of the growing bubbles was increased, making it easier for bubbles to detach from the plate. Essentially, as the volume to cross-sectional area ratio is decreased and since drag depends on the area exposed to the incoming fluid, bubbles with smaller volume are formed. A schematic of the device and the mechanism of size reduction is shown in figure 3.2. The volume of alcohol injected

Transmitter Optics		
Wavelength (nm)	514.5	488.0
Focal lenth (mm)	515	515
Beam separation (mm)	20	20
Laser Beam diameter (mm)	0.7	0.7
Expander	1	1
Expanded beam separation (mm)	20	20
Expanded beam diameter (mm)	0.7	0.7
Fringe spacing (μm)	13.25	12.57
Beam waist (μm)	481.95	457.13
Shift (MHz)	40	40
Velocity limit min. (m/s)	-463.78	-439.89
Velocity limit max. (m/s)	1457.68	1382.52
Diameter limit min. (μm)	7.95	
Diameter limit max. (μm)	927.7	

Receiver Optics			
RCV. Front lens (mm)	500	Collection angle (o)	63
RCV. Back lens (mm)	250	Slope	0.431
Slit apperture (μm)	150		

Table 3.1: Settlings of the PDPA system used to characterize the turbulent flow.

was very small, approximately 1 ml/s, and so its effect on the bulk properties of the carrier fluid was negligible.

3.1.2 Turbulence characterization

The turbulence was characterized with Laser Doppler Velocimetry. Using the smallest bubbles as flow tracers, the carrier fluid velocity components in two perpendicular directions, along the mean flow and along the direction of gravity, were obtained from the PDPA measurements by filtering out the data for bubbles larger than 50 μm. From these measurements, the turbulence characteristic length, time and velocity scales were computed. The homogeneity and isotropy of the flow in planes perpendicular to the mean flow were also confirmed. The parameters used for the LDV measurements are shown in table 3.1.

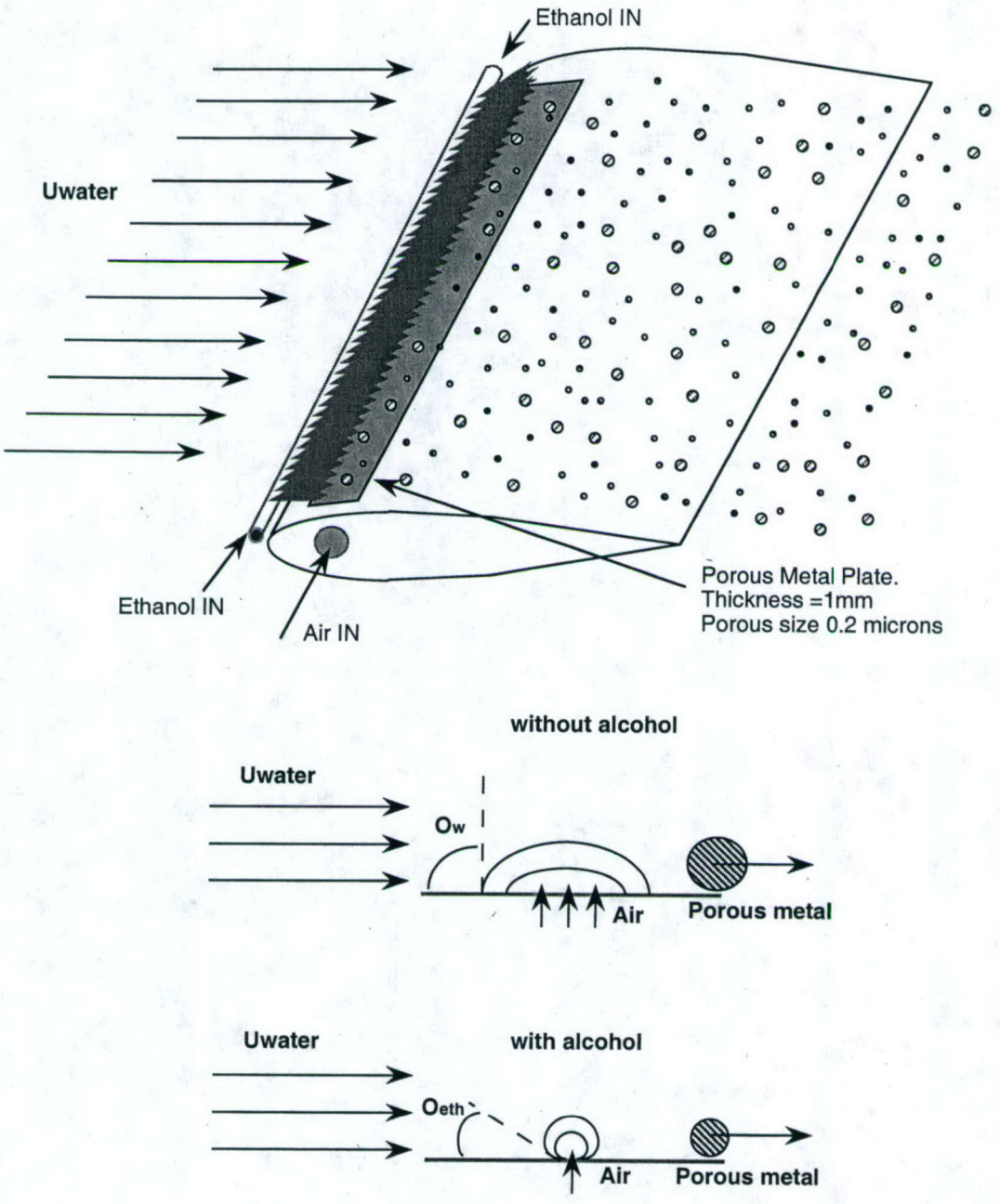

Figure 3.2: Sketch of the bubbler and the diameter reduction mechanism.

3.1.3 Bubble diagnostics

The measurements of the bubble velocity were carried out exclusively by the Phase Doppler Particle Analyzer system. This system, which has been described at length in Chapter 2.1.2, uses the frequency and phase shifts of the laser light reflected by bubbles that cross through the probe volume to compute the velocity and diameter of the bubbles. For the measurements of the bubble size and velocity in this experiment, the emitter was located on one side of the water channel test section. Two pairs of beams of different frequencies, perpendicular to each other, were projected the into test section and intersected at a certain point in the flow, materializing the probe volume. Every bubble that crossed that volume reflected light from all four beams. The receiver was located above the test section, looking down on the probe volume at a 63° angle with the line of propagation of the emitted light. A plexiglass triangular prism, with a matching 63° major angle, was filled with water and positioned at the free surface to ensure that light would leave the water channel perpendicular to the interface between water and air, minimizing refraction of the beams as they propagate into a medium of different refraction index. A sketch of the setup is shown in figure 3.3. This mode of operation, 63° forward reflection, has been shown to provide the best accuracy in the measurements of bubble diameters, Bachalo (1994). The system acquired and analyzed the reflected light, computing the frequency and phase shifts introduced by the bubble in each pair of beams. From that information the system provided the diameter of the bubbles and two components of the velocity, in this case the streamwise and vertical components.

Flow visualizations were used to obtain information on the spatial distribution of the bubbles. This technique allowed a large area of the flow to be sampled. The techniques referred to above, provided with point measurements while this one gave instantaneous information on the distribution of bubbles in a large area in the flow. To obtain an instantaneous visualization of the position of the bubbles in the flow, a vertical slice of the flow was illuminated by a laser

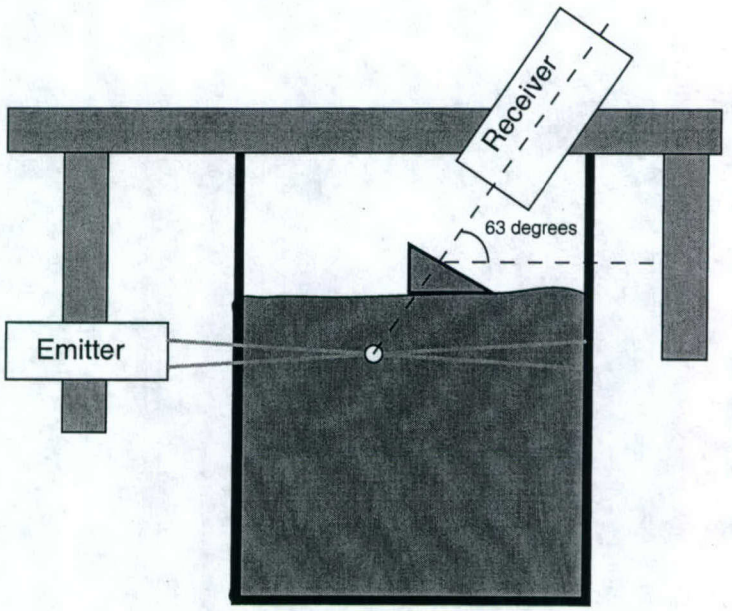

Figure 3.3: Sketch of the mount used to take PDPA measurements on the water channel.

plane projected from the bottom of the test section. The beam from a Ar ion laser was redirected to a rotating mirror located under the test section of the channel. The vertical plane of light swept the flow at 4000 Hz and the light reflected by the bubbles was captured by a Kodak ES 1.0 digital high resolution (1008x1008 pixels) CCD camera located perpendicular to the laser plane. Using NIH image processing software, large sets of images taken with this method were made binary and analyzed, following a procedure that has already been described in Chapter 2.1.3. Following this image processing technique, the location of the bubble centroid was computed and stored. By analyzing a large number of images taken under the same conditions, statistics of the concentration field of the particles could be build and the influence of the turbulence was studied. Information on the preferential accumulation of bubbles obtained with this method is presented in section 3.2.2.

Statistics of the bubble diameter distribution were obtained from attenuation images taken with the digital camera described above. A source of collimated

light was placed opposite to the camera, on the other side of the test section. Thus, the light propagated across the test section and was scattered by the bubbles in the flow. The camera captured the light deficit created by the bubbles with respect to the bright background. The camera was focused at the same point used for the PDPA measurements and set to a large aperture so that the a narrow depth of field was achieved. A background image was captured, in the absence of bubbles, and subtracted from the bubble image to minimize the errors due to uneven illumination conditions. The outcome of this subtraction was then thresholded and processed to extract the area and location of the bubbles. A typical pair of images, raw and thresholded, is shown in figure 3.4. The equivalent diameter was computed from the cross sectional area, assuming the bubbles were spherical.

3.2 Experimental results

Three sets of experiments were conducted to study the influence of the carrier flow turbulence on the rise velocity and concentration field of the bubbles. The first one looked at the rise velocity of relatively large bubbles, in the range 300-1200 μm, using PDPA measurements. The second used a modification of the PDPA optics and signal processing settings to look at the rise velocity of smaller bubbles, in the range 10-400 μm. Finally, flow visualizations were used to study the bubble instantaneous concentration field.

3.2.1 Rise velocity measurements

The streamwise and vertical velocities of the bubbles, as well as their size, were measured at two different locations downstream from the grid, $x/M = 24$ and $x/M = 30$, and at different velocities of the water channel. The rise velocity obtained by averaging the vertical velocities of all bubbles within a size range are plotted in figure 3.5, as a function of the average diameter of the bubbles within that size range. The velocity increases with size, somewhat quadratically. Due to

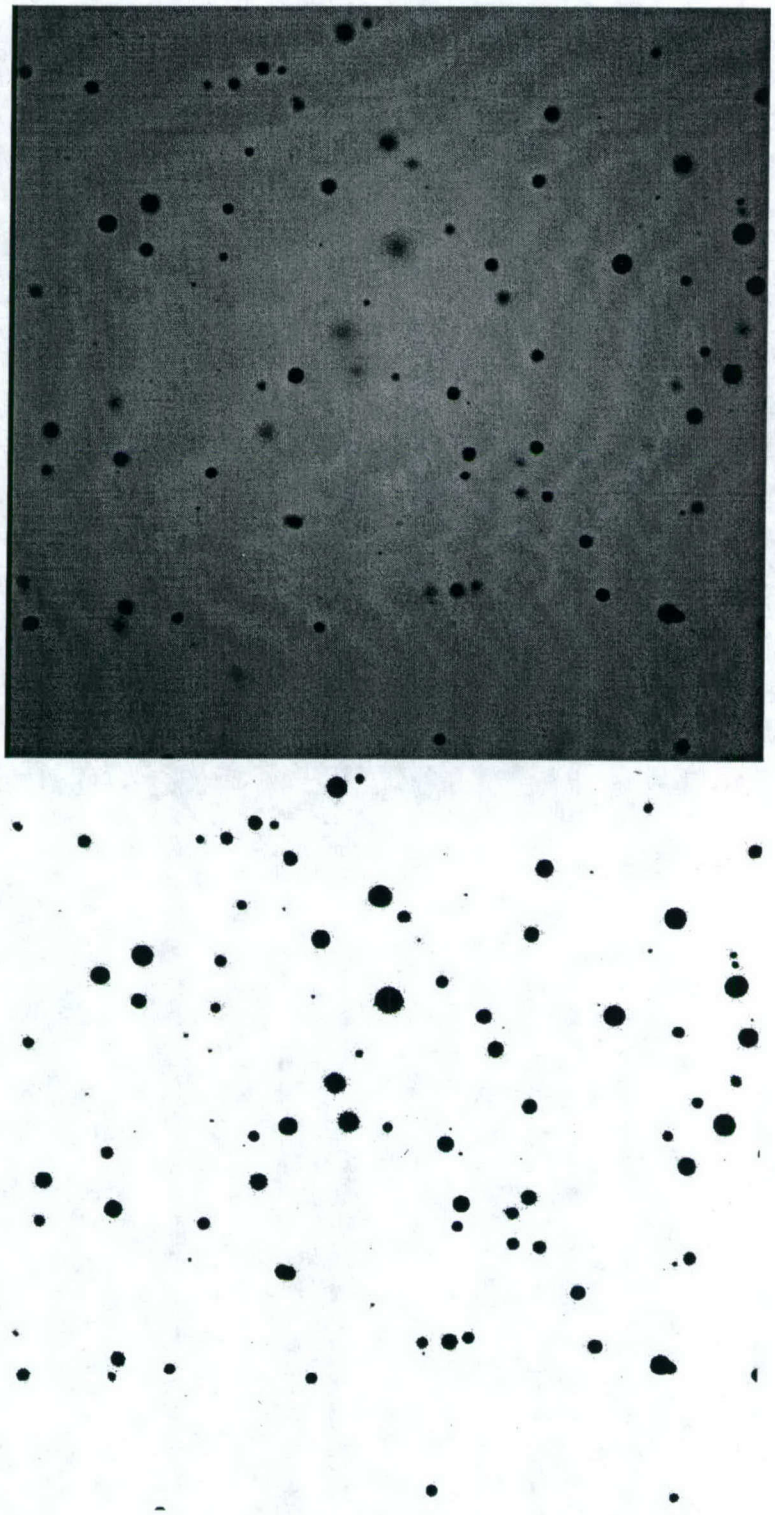

Figure 3.4: Typical images used to determine the bubble diameter distribution.

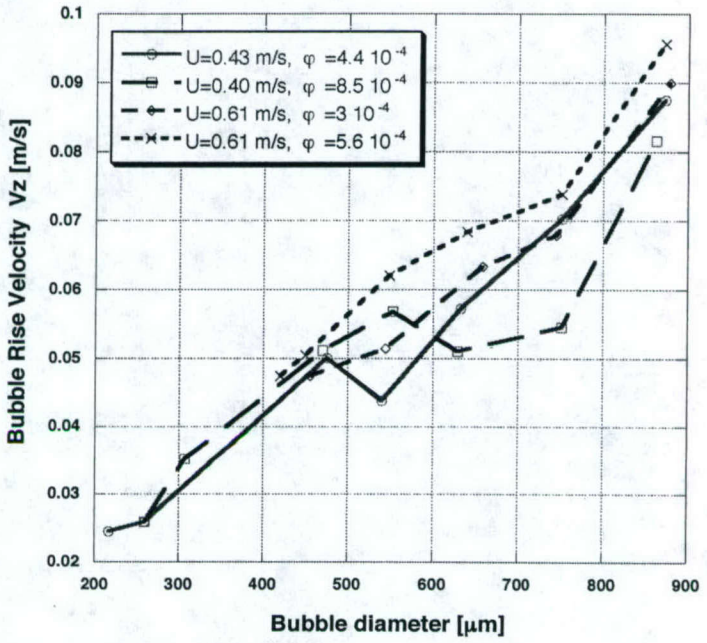

Figure 3.5: Measurements of the average vertical velocity of the bubbles.

the low data rate obtained by the PDPA, two orders of magnitude lower than for the heavy particles in Chapter 2.2.1, and the uncertainty in the measurements of the vertical velocity, the smallest size class is composed of bubbles with diameters between 0 and 300 microns. This wide range was necessary to ensure that a large number of bubbles was used to compute the statistics of the velocity. It is critical to obtain reliable statistics of the smaller size class, as they were used to characterize the turbulence and, more importantly, the mean vertical velocity of the smallest size class was used to align the laser beams to a horizontal axis. As explained in Chapter 2.1.2, misalignment between the laser beams and the horizontal axis of the channel would cause a small component of the streamwise velocity being measured as part of the vertical velocity, contaminating the data. Thus, the laser beams were rotated in their mount until the mean vertical velocity of the smallest class was found to be zero within experimental error. The rise velocity of bubbles of a certain size, within the PDPA smallest size range, was computed by an indirect

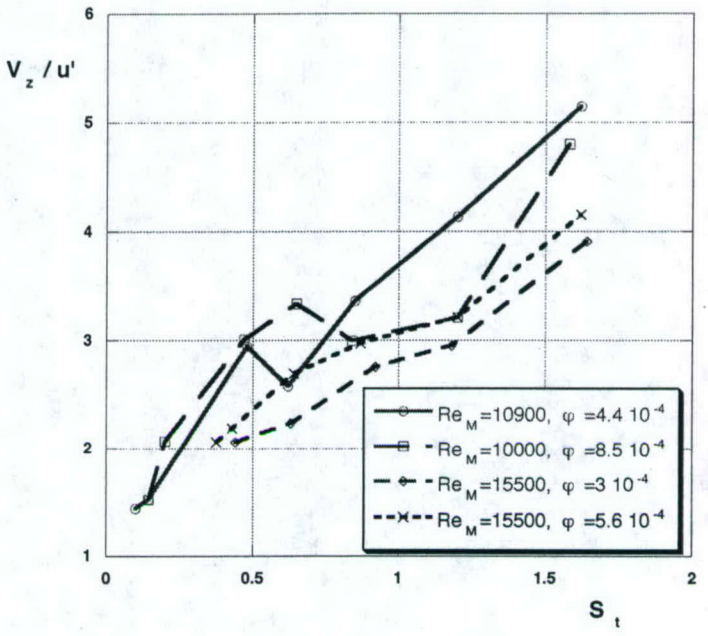

Figure 3.6: Normalized average rise velocity of the bubbles.

method explained below. These values represent the rise velocity for the smallest bubbles that can be measured with these settings, reducing the experimental error incurred when assigning a zero rise velocity to bubbles with non zero diameter. In figure 3.6, the same data is non dimensionalized by the root mean square of the fluctuating velocity and plotted against the Stokes number of the bubbles. It can be observed that the data non dimensionalized in this way seems to show a consistent behaviour over different values of the turbulence intensity.

In order to obtained measurements of the bubble rise velocity that are independent of the alignment of the laser beams, which has been found to create problems, see Chapter 2.1.2, in the interpretation of the data on the vertical velocity of small bubbles, an indirect method was devised. A single bubble injector was used to introduce a point source of bubbles in the flow. The size distribution of bubbles was measured at two different locations downstream from the source (and the turbulence inducing grid). The evolution of the bubble cloud under mean flow convection, turbulence dispersion and buoyant rise would make the size distribu-

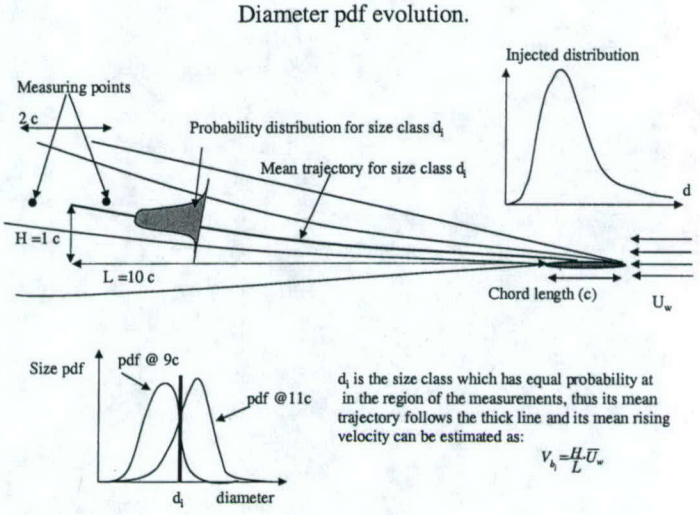

Figure 3.7: Schematic of the vertical velocity measurement based on the evolution of the bubble size distribution.

tion vary spatially, see figure 3.7. If one compares two size distributions measured a small distance apart, one would find that there is a bubble size which has not changed, whereas all sizes larger than that are decreasing their number density (because they rise faster and the measurements are already in the tail of the distribution) and all sizes smaller than this one will increase their number density (because they rise slower and they have not yet reached the maximum in the distribution). The size class that is going through the maximum at the location of the measurements has an average rise velocity that can be computed from geometrical considerations as $V_z = U_\infty \cdot H/x$. The result from this computations are shown in figure 3.8. From these measurements, we obtained a value of the rise velocity, independent of the laser alignment, to use as a reference for each Reynolds number case plotted in figure 3.5.

Finally, modifications of the laser optics, as well as the electronic settings were introduced to greatly increase the resolution with which the bubble vertical velocity could be measured by the PDPA. The rise velocity of the smallest bubbles was directly measured with a resolution better than 5 mm/s, and the results are

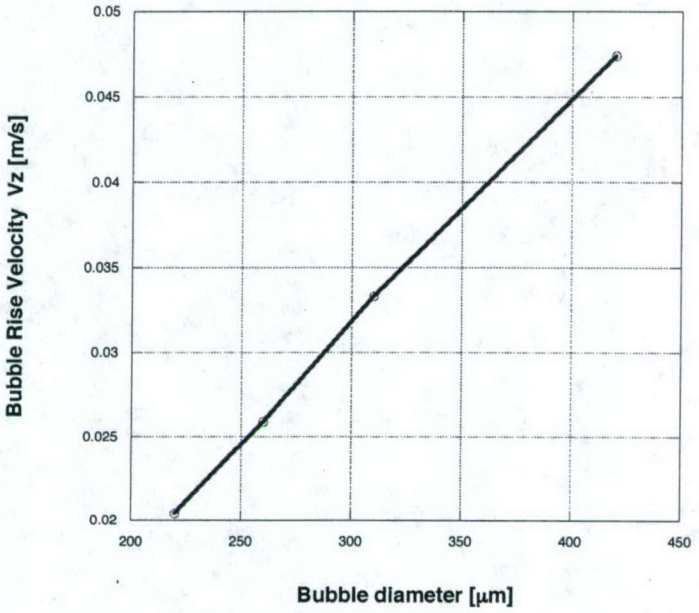

Figure 3.8: Indirect measurements of the average rise velocity for the smallest bubbles.

shown in figure 3.9 for two values of the turbulent intensity. For comparison, the values of the rise velocity in still fluid predicted by three different correlations available in the literature, are plotted in the same figure. The values of the rise velocity predicted by Maxworthy *et al.* (1996) for rigid bubbles, and by Detsch (1989) for tap and sea water, agree quite well. The uppermost curve is given by the simple Stokes law, without corrections for the finite Reynolds number. It is important to point out that the the smallest bubbles in the experiments reported by Maxworthy *et al.* (1996) were larger than the ones reported here (400 μm). Even with triply distilled water, they found that the behaviour of the smaller bubbles was very close to the rigid bubble with no internal circulation. Thus, for the bubbles in this range (10-400 μm) the clean, stress free surface with internal circulation is considered irrelevant and only the correlations obtained for contaminated, rigid bubbles have been considered. The measurements are still subject to the alignment problem and so the system was again aligned until the smallest class size, in this case 5-50 μm,

was found to have zero vertical velocity. The results seem to agree quite well with the indirect measurements taken by the evolution of the size distribution, detailed above, and complement the measurements of the rise velocity of large bubbles explained earlier.

3.2.2 Bubble visualizations

The instantaneous concentration field of bubbles in the flow was investigated by analyzing visualizations of vertical slices of the flow illuminated by a laser plane. From the many methods detailed in Chapter 2.2.2 to characterize the spatial distribution of the disperse phase in a turbulent two-phase flow, the one that proved most successful in that Chapter, namely the comparison with a random distribution, was applied to this problem. The algorithm to quantify the deviation from randomness of the bubble concentration, and its evolution with the length scale is briefly described here. A more complete explanation can be found in Chapter 2.2.2. By processing the images of the light reflected from the bubbles, their position was obtained. Once this information had been extracted, the images were divided in square windows of a certain size and the number of bubbles in each window counted. Taken into account the number of bubbles per window, for all the windows of a certain size in all the images taken under the same flow conditions, the probability density function of number of bubbles in a window could be computed. This probability distribution was then compared to the Poisson distribution, which is the probability distribution corresponding to a random field of bubbles. To obtain a quantitative measure of the deviation from randomness, the same two parameters that were introduced in Chapter 2.2.2, were used. If this algorithm is repeated for varying sizes of the windows, the evolution of this parameters that quantify the clustering can be obtain. The distributions obtained from very small windows, comparable to the smallest flow scales, must be very similar to the random distribution, since the process becomes binary, there is zero or one bubble in each window. For very large windows, larger than the integral length

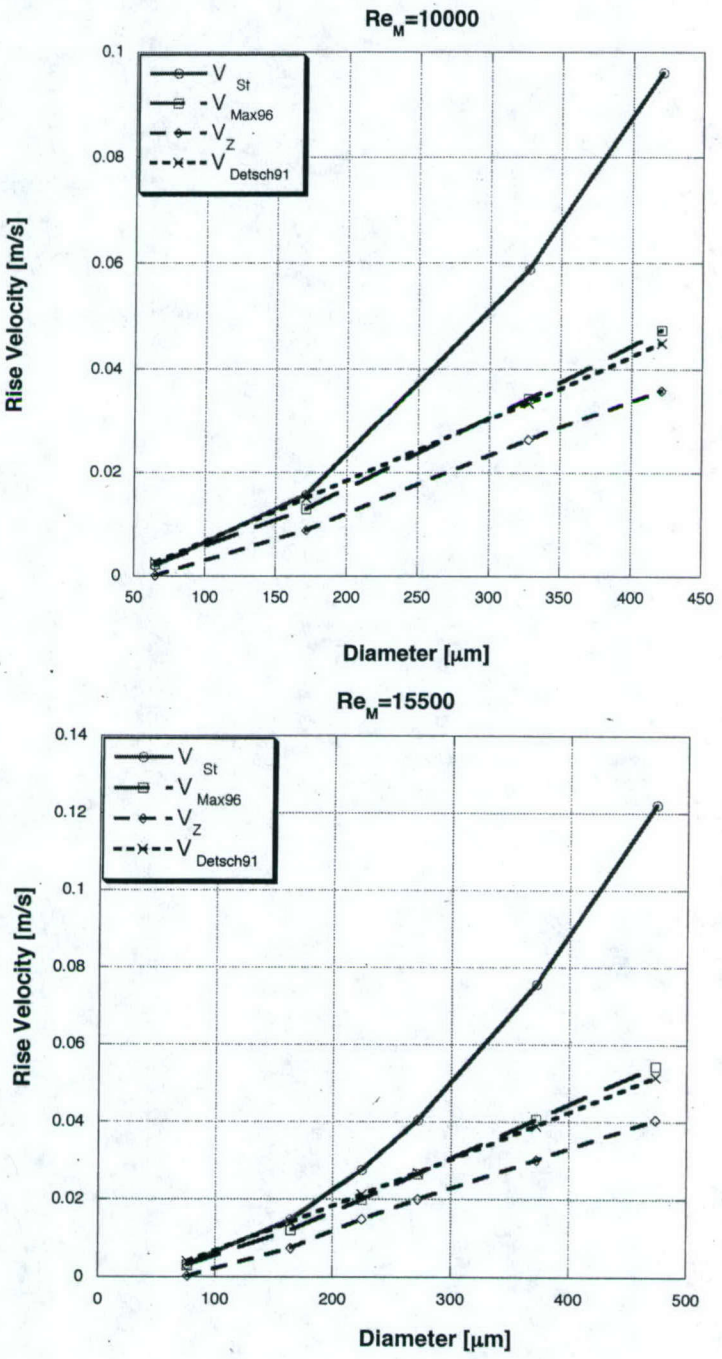

Figure 3.9: Direct measurements of the rise velocity for small bubbles. Comparison with three different estimates of the rise velocity of small bubbles in still fluid.

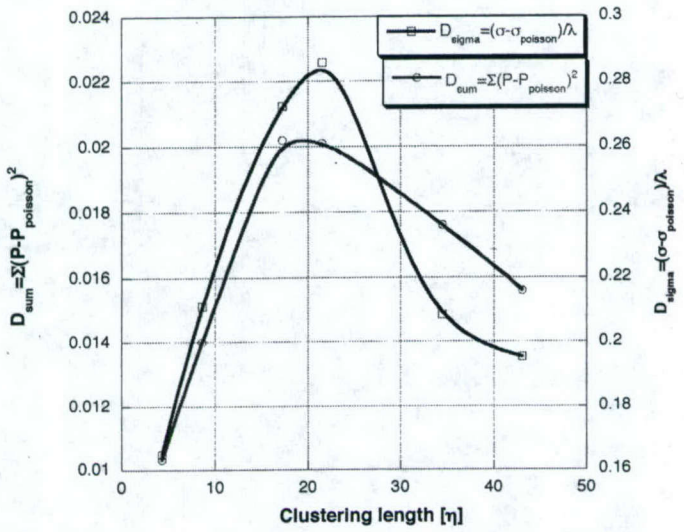

Figure 3.10: Preferential concentration of bubbles. Characteristic length scale. U=0.25 m/s, $\alpha = 8 \cdot 10^{-4}$

scale of the turbulence, the process again resembles a random distribution, as each window contains regions of high concentration and regions devoid of bubbles and the process of counting the bubbles integrates the concentration field smearing the clusters. The results from this complicated process can be seen in figure 3.10, for a particular value of experimental settings. Several conditions were tested and the result was consistent in all of them. As predicted by the theory, the deviation from randomness parameters showed the tendency to zero, although the larger windows were not large enough to show the values approaching zero. At the intermediate scales, however, preferential accumulation of bubbles was present in every case and it was maximum for windows with a size corresponding to about 20 times the Kolmogorov length scale. This is about twice the characteristic size of the particle clusters found in the experiments reported in Chapter 2.2.2.

3.3 Analysis

To establish the effect of the turbulence on the rise velocity of the bubbles, one need to compare the measured rise velocities with the values the those same bubbles would have in a stationary fluid. This is not a simple task, as it was to compare the settling velocity of heavy particles in turbulence versus in still fluid. The rise velocity of a bubble in still fluid is not simply determined by its diameter and relative density, as is the case with the settling of a spherical particle. There are different regimes depending on the surface tension between the fluids and the shape of the bubble. As explained by Maxworthy *et al.* (1996), bubbles behaviour can evolve continuously between that of a rigid sphere with no internal circulation and that of a fluid sphere with a free-stress boundary, depending on the surface tension and the viscosity. They also go through different regimes, sphere, ellipsoid and spherical cap as the size increases. The bubbles in these experiments keep their spherical shape, but it was not clear which was the right drag coefficient to use in the rise velocity computation. Two different velocities were computed for comparison, corresponding to the contaminated surface with a no slip boundary condition and to the clean surface with a stress-free interface with internal circulation cases. The equations for the rise velocities, obtained from Maxworthy *et al.* (1996), are given in Equations 3.1 and 3.2, respectively. These values were used for comparison with the rise velocity of the large bubbles, in the size range of the original experiments from which they were developed.

$$\begin{aligned} Cd &= \frac{24}{Re} \cdot (1 + \frac{1}{8} Re) \\ V_z &= \frac{d^2}{18 \cdot \nu_f \cdot (1 + \frac{1}{8} Re)} \cdot g \end{aligned} \tag{3.1}$$

$$\begin{aligned} Cd &= \frac{11.1}{Re} \cdot Re^{-0.28} \\ V_z &= \frac{4 \cdot d^2}{33.3 \cdot \nu_f \cdot Re^{-0.28}} \cdot g \end{aligned} \tag{3.2}$$

The non dimensional difference between the rise velocity of the bubbles in the turbulent flow and the velocity predicted for contaminated rigid bubbles in still fluid, equation 3.1, is shown in figure 3.11. One can observe the presence of an minimum for values of Stokes number close to unity. The comparison of the turbulent bubble rise velocity with the two limiting cases of the drag coefficient is shown in figure 3.12. In the lower curve, the rise velocity of bubbles is compared to the one predicted in still fluid for a clean, fully recirculating sphere, that has the lowest drag coefficient, equation 3.2. In the upper one, the measurements are again compared against the velocity predicted for a bubble with contaminated interface which is rigidified by surfactants and does behave as a solid sphere and has a higher drag coefficient, equation 3.1. It is worth noting that the conditions in the present experiment were closer to the fully contaminated, rigid surface than to the clean, recirculating sphere and thus a very large reduction was obtained when the measurements were compared to the maximum rise velocity obtained for the clean sphere. However, as both curves present negative values, one can claim that a reduction of the rise velocity of the bubbles due to the turbulence has been found, regardless of the uncertainty on the concentration of surfactants in the experiment.

For the case of the smallest bubbles, the experimental data from Detsch (1989) was used for comparison. These were obtained for very small bubbles, using distilled, tap and sea water. The values for tap and sea water were found to be almost identical and were used as a good approximation to the conditions in our experiments. The values of rise velocity obtained for tap and sea water were fitted by a three term empirical law given in equation 3.3,

$$V_z = -4.71\ 10^{-3} + 1.12\ 10^{2} \cdot d + 1.42\ 10^{4} \cdot d^2 \tag{3.3}$$

where the velocity is given in meters per second and d is the bubble diameter in meters.

The values of the reduction in rise velocity of the smaller bubbles, which

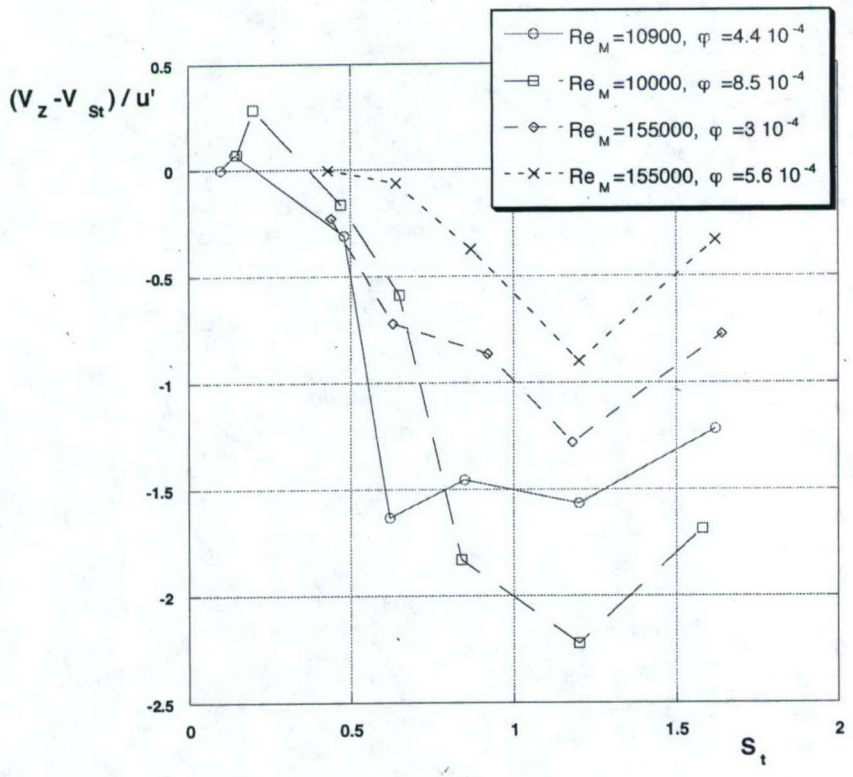

Figure 3.11: Rise velocity reduction for bubbles in the 400-1000 μm range.

a)

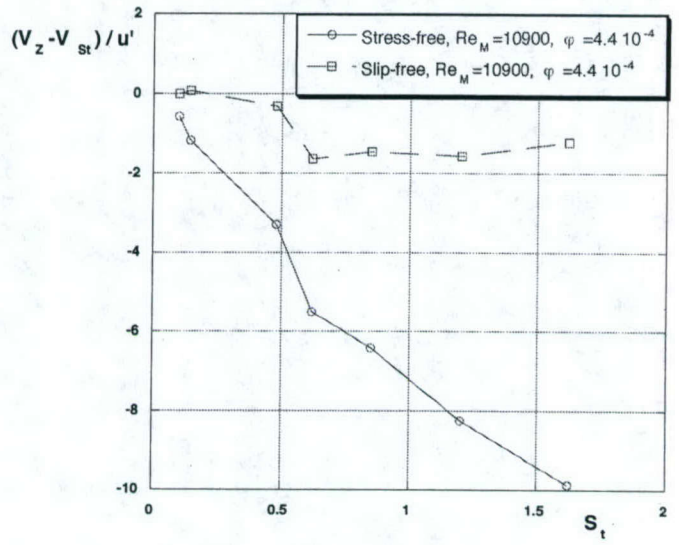

b)

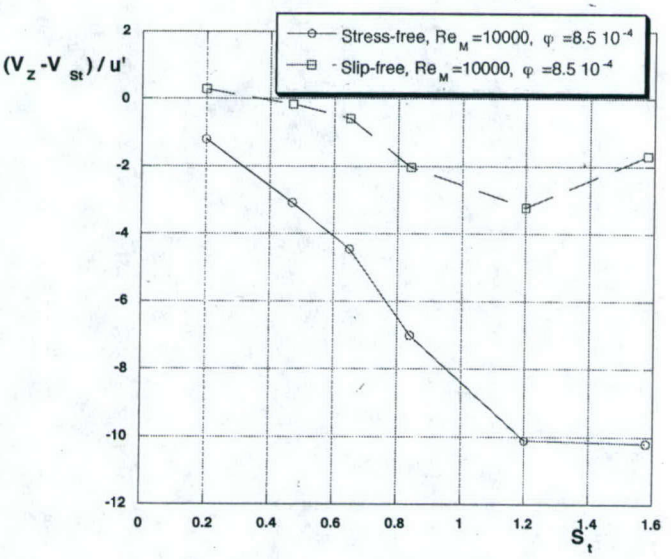

Figure 3.12: Rise velocity reduction as a function of the bubble Stokes number. Stress free, clean surface and internal circulation (eq. 3.2), and slip-free, contaminated surface with no internal circulation (eq. 3.1)

c)

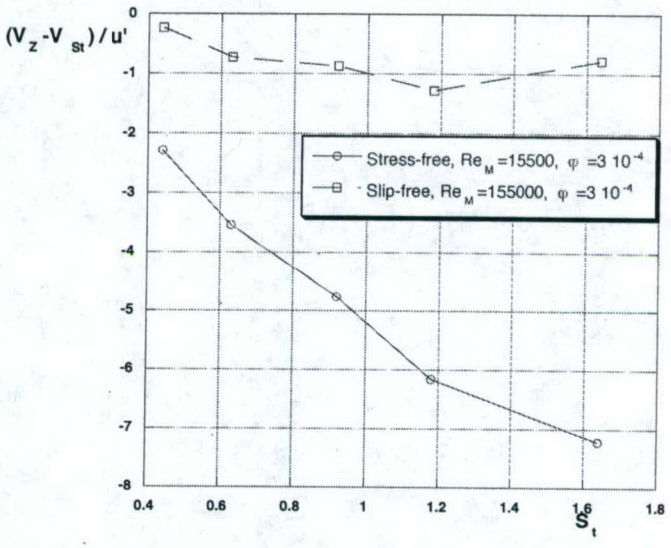

d)

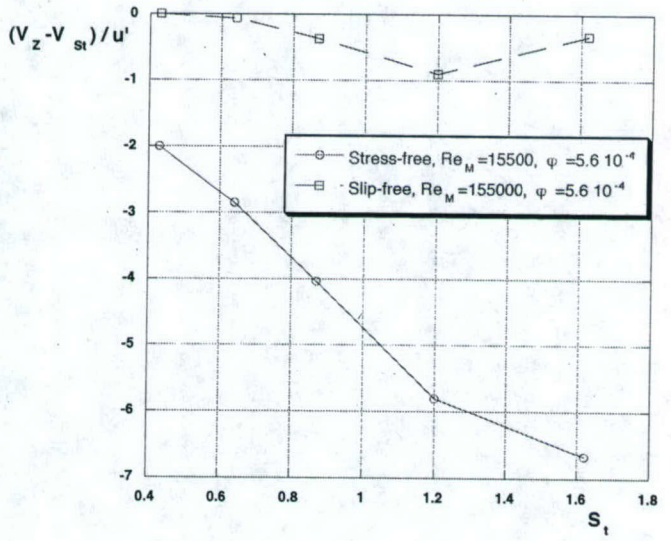

Figure 3.12: continued

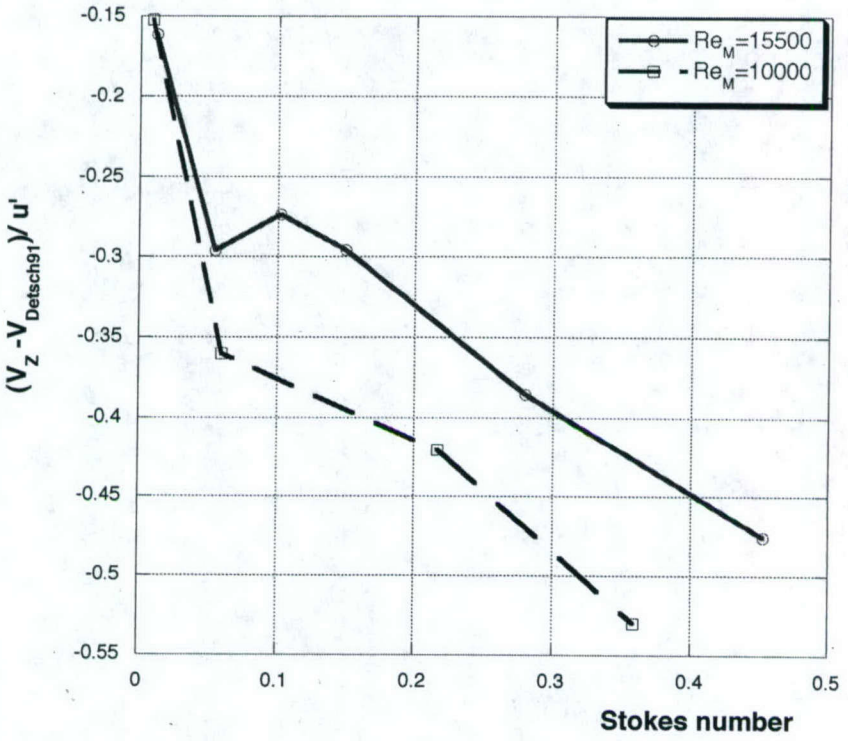

Figure 3.13: Rise velocity reduction for bubbles in the 50-400 μm range.

can be seen in figure 3.13, and were found to be significant. When the reduction is non dimensionalized with the root mean square of the fluctuating velocity of the carrier fluid, the results seem to collapse, in good agreement with the hypothesis that the rise velocity reduction is caused by the interaction of the bubbles with the turbulent structures and u' is a measure of the level of turbulent kinetic energy present in this flow.

3.4 Conclusions

The behaviour of small air bubbles in a turbulent water flow has been investigated. In parallel with the study described in Chapter 2.2.1, a homogeneous isotropic decaying turbulent flow was created by a grid located at the beginning of the channel test section. The bubbles injected into the turbulent flow were allowed

to interact with the turbulence for a large number of viscous relaxation times so that the memory of the initial conditions was lost and their behaviour was only a function of the diameter and the characteristics of the turbulence.

Different correlations found in the literature were analyzed to determine the rise velocity of bubbles in still fluid. The values from Detsch (1989) were used for the smallest bubbles ($50 - 400\ \mu m$) while the values from Maxworthy *et al.* (1996) were used for the larger ones. The two correlations were found to give consistent values in the overlap region of validity.

The rise velocity of the bubbles was found to be reduced with respect to the velocity they would have in still fluid. This reduction was very significant, even for very small bubbles (in the $50 - 400\ \mu m$). The reduction in the rise velocity was maximum for bubbles with Stokes number of order unity. The Stokes number was computed using the Kolmogorov time scale of the turbulence, a choice consistent with the results discussed in the previous section. The r.m.s. of the turbulent velocity fluctuations was used to make the reduction of the rise velocity non dimensional. Thus, the curves obtained for different turbulence intensities were found to collapse to a certain extend.

The interaction of the bubbles with the turbulence in the carrier fluid leads to the formation of large inhomogeneities in the concentration filed of the bubbles, in good agreement with the numerical simulations by Wang & Maxey (1993*b*) and the results from the experiments described in Chapter 2.2.2. The scale at which this accumulation due to the turbulent structures was found to be more efficient is 20 times the Kolmogorov scale of the turbulence, somewhat larger than the result in the previous section. The difference in the value of the Reynolds numbers of the carrier flows, 10^5 vs. $0.5 \cdot 10^6$, was considered to be responsible for the different length scale.

Chapter 4

Dynamics of a turbulent boundary layer laden with microbubbles

4.1 Experimental set-up

The experiments were performed in the same recirculating water channel described in Chapter 3. A plexiglass plate was cut to dimensions 2x0.6x0.0127 m. and mechanized so that it could be placed vertically inside the the test section of the water channel. A bubble injector, described below, was attached to the plate at the leading edge so that the bubbles were introduced inside the boundary layer, at the beginning of its development. The injector also served as a tripping mechanism for the turbulent boundary layer to transition fully within the channel test section. Once positioned inside the test section, the flat plate extended horizontally through the entire length of the test section and vertically from the bottom of the channel to well above the free surface. Thus, the flat plate pierces the surface, originating a corner type flow at the junction of the solid plate and the free surface. A sketch of the facility is shown in figure 4.1.

A large number of very small bubbles, $d_{32} \approx 200\mu m$, were injected into

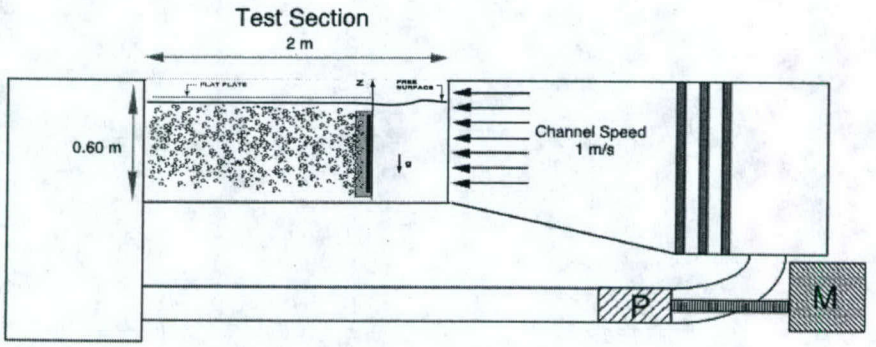

Figure 4.1: Recirculating water channel.

the flow so that the volume fraction reached was significant to study the influence of the bubbles in the underlaying turbulent carrier flow, $\phi \approx 10^{-3}$. An injector similar to the one already described in Chapter 3 was used for this purpose. A spatially uniform distribution of bubbles is created by the injector at the leading edge of the plate. The size distribution of bubbles injected at different depths can be seen in figure 4.2. This initial uniformity disappears as the bubbles interact with the turbulent structures of the boundary layer and the gravitational field. The initial bubble void fraction at the injection point is very large, of the order of 5%, but quickly decreases as the largest bubbles created by the injector, which carry a large part of the volume, rise to the surface and disappear. Thus, the void fraction inside the turbulent boundary layer, measured a few boundary thicknesses downstream of the injection, is relatively low, $o(10^{-5}) - o(10^{-3})$, and bubble-bubble interactions can be considered negligible.

4.1.1 Bubble size measurements

The same high resolution (1008x1008 pixels) Kodak ES 1.0 digital camera described in Chapter 2.1.3 was used to characterize the bubble size distribution and the concentration, as well as the velocity field. Using the image processing technique described in Chapter 3.1.3, the location of the bubble centroid was computed

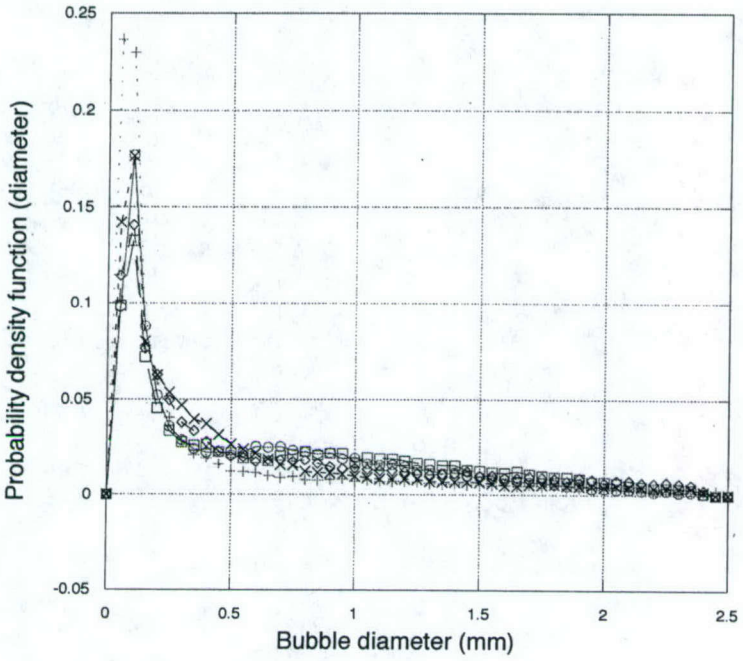

Figure 4.2: Bubble diameter distribution at injection.

and stored. By processing this information, the velocity and bubble concentration fields could be determined.

The characterization of the bubble diameter distribution was done following the procedure detailed in Chapter 3.1.3, for the sizing of the bubbles injected in homogeneous isotropic turbulence. In this experiment, the camera was focused on a point 15 mm from the plate, where the bubble number density was highest, and set to a small aperture so that the whole boundary layer was within focal depth of field. Typical images of the bubbles in the boundary layer used in this process are shown in figure 4.3

4.1.2 Velocity measurements

Measurements of the carrier flow velocity were obtained from images of the light reflected by the smallest bubbles when the flow was illuminated by a laser plane in the two configurations shown in figure 4.4. In the first set of measurements, the flow was illuminated with a horizontal streamwise laser plane, normal

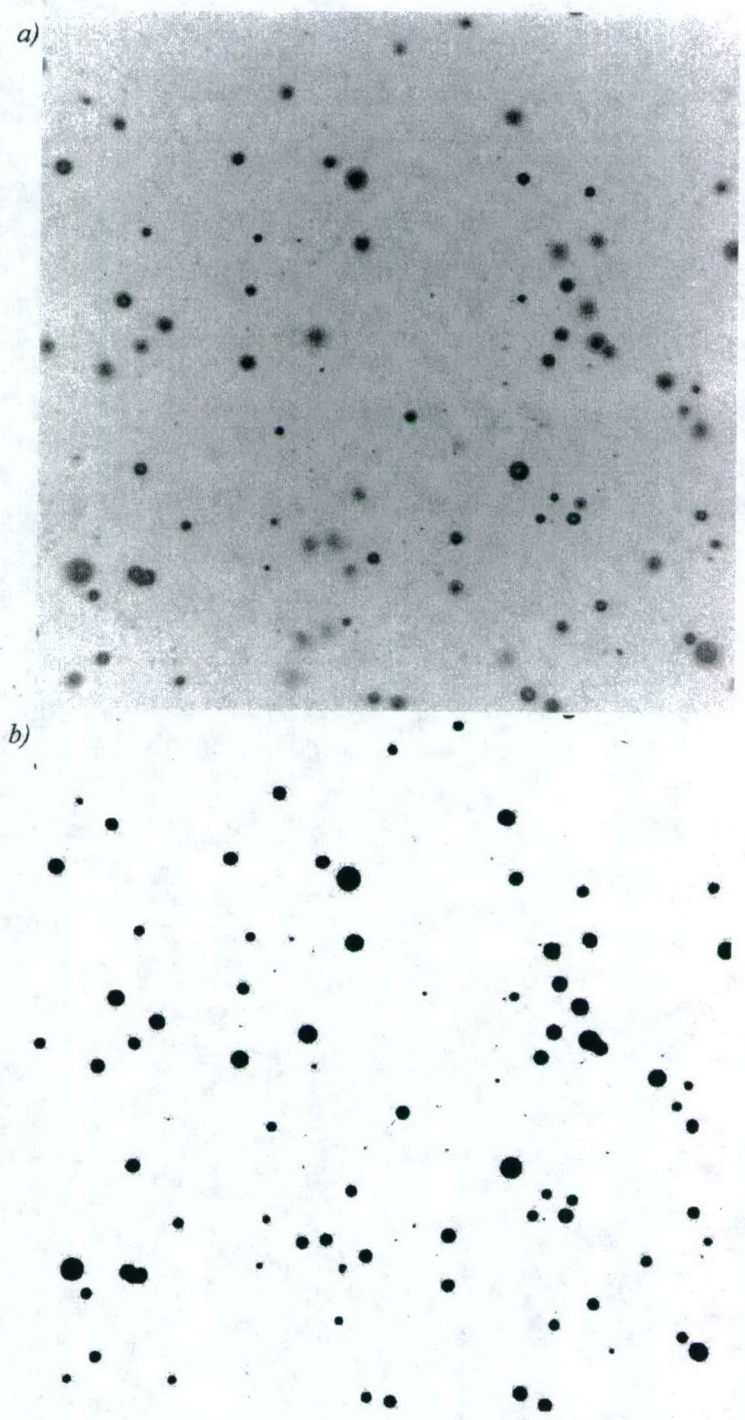

Figure 4.3: Typical pair of images of the bubbles inside the turbulent boundary layer. *a*) Background subtracted. *b*) Threshold applied.

to the flat plate and parallel to the free surface. The streamwise and spanwise velocity components were extracted, by both Particle Image Velocimetry and Particle Tracking Velocimetry, from the images. The plane was positioned at a depth z=0.28 m. from the free surface, deep enough that the boundary layer was not affected by free surface effects. The second set of measurements consists of streamwise and vertical bubble velocities obtained from images of the flow illuminated by a laser plane parallel to the flat plate and located at different distances from the plate. The camera was focused on a small region, approximately $0.04 \cdot 0.04\ m^2$, at the same depth as the first set of measurements. The interaction between the three components of the velocity could then be analyzed.

Images were taken at two downstream distances from the leading edge, x=0.36 m. and x=0.94 m., both far enough downstream that the boundary layer has transitioned into a fully turbulent state and the characteristics of the flow are independent of the tripping mechanism. Since the free stream velocity dominates the formation of the bubbles at the injector, as well as their convection along the plate inside the boundary layer, the void fraction and Reynolds number at a given location are both function of the channel mean velocity. By taking measurements at different locations within the boundary layer we were able to change the Reynolds number and the void fraction independently. The laser plane was created with the same technique described above for the flow visualizations. For the velocity measurements, however, the frequency of the rotating mirror was synchronized with the time exposure of the camera to ensure that two sweeps of the laser beam would be captured in each frame. Also, an a priori evaluation of the velocities to be measured was carried out, so that the displacement of the bubbles between sweeps would be large enough to minimize the experimental error. This, together with high spatial resolution of the images ensured a low uncertainty of the measurements. An estimate for a single bubble velocity measurement can be computed as:

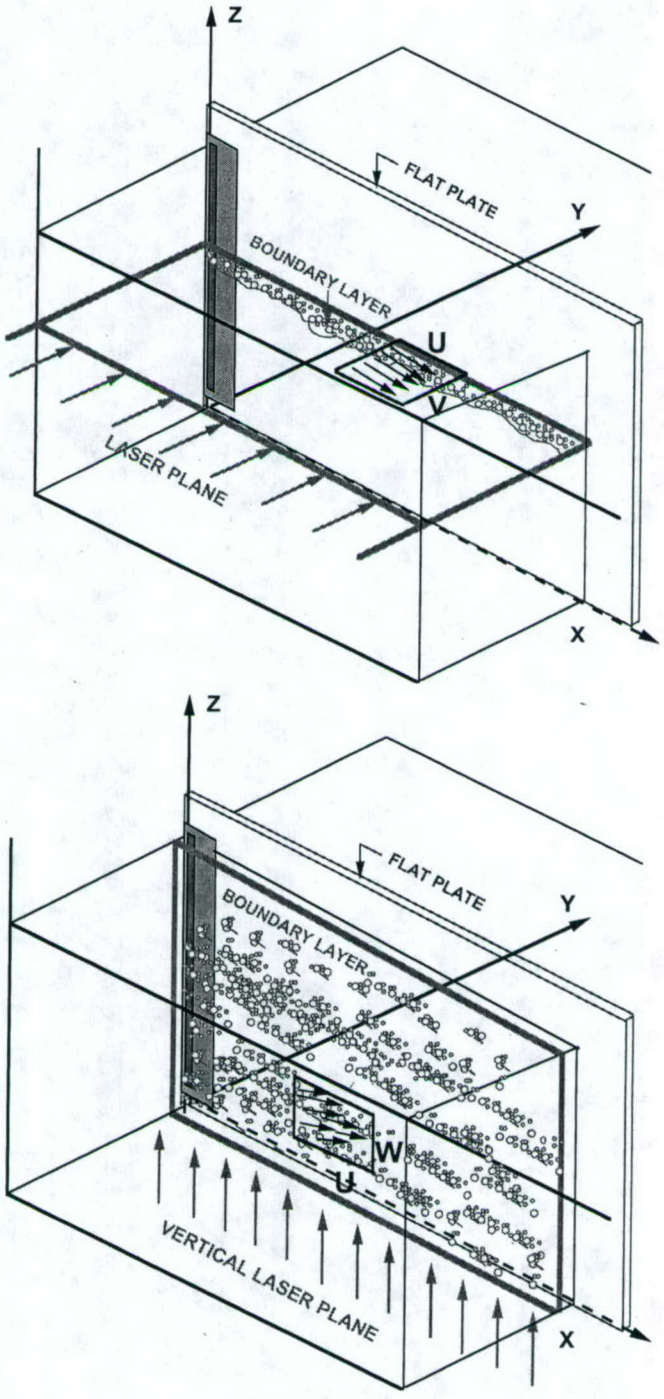

Figure 4.4: Sketch of the imaging area for velocity measurements.

$$\frac{\Delta x}{x} = \frac{1/2\ pixel}{2.5\ 10^4\ pixel \cdot\ m^{-1} \cdot 1.25\ 10^{-3}\ s \cdot 0.6\ m \cdot\ s^{-1}} \approx 2.75\ \% \qquad (4.1)$$

Velocity measurements were obtained using a commercial PIV software package (TSI Insight) as well as an in-house particle tracking algorithm. The results from both techniques were very consistent with the particle tracking providing better results in low void fraction cases, due to the larger spatial resolution and number of realizations, while the PIV provided better results in high void fraction situations, due to the larger number of bubbles per interrogation window and the difficulties of the tracking algorithm in identifying bubble pairs in these cases. A very large number of images, o(10^3), were collected for each flow condition and an ensemble-average was computed from all the measurements. The spatial resolution for the PTV was about 50 μm, while for the PIV was close to 800 μm (using a spot size of 32 pixels).

4.2 Experimental results

4.2.1 Velocity measurements

The streamwise velocity profiles measured are shown in figure 4.5. They were found to be very similar to the well known profiles from single phase turbulent boundary layers, Klebanoff (1955). The existence of a logarithmic region was confirmed for all cases studied, with the local bubble void fraction going up to 5 10^{-3}. The non-dimensional profiles corresponding to the ones plotted in figure 4.5 are displayed in figure 4.6, normalized using viscous scales. Measurements within the viscous and buffer layer were restricted by the spatial resolution of the images, $\delta^+ < 1\ pixel$, and the existence of reflections on the wall that contaminated the images very near the wall.

Unlike the streamwise component, the wall-normal velocity profile measured was very different from a single phase case. Figure 4.7 shows profiles of the

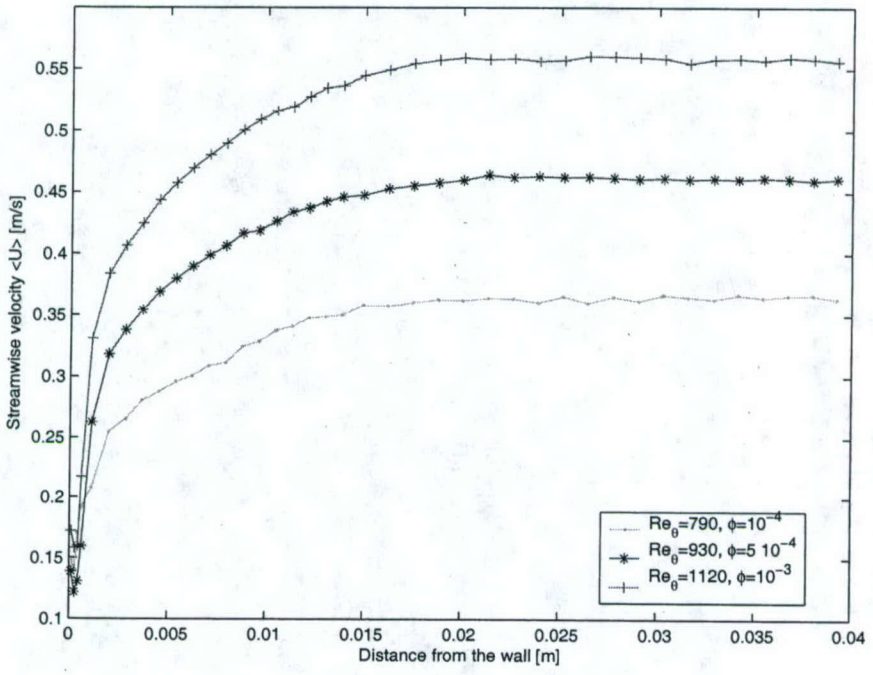

Figure 4.5: Streamwise velocity profiles. Dimensional quantities

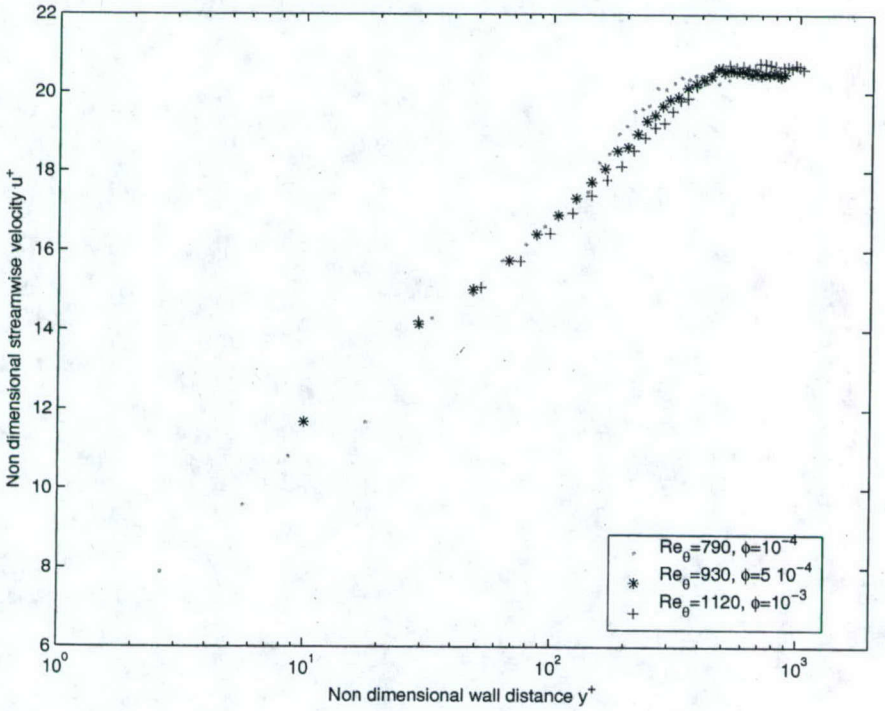

Figure 4.6: Non dimensional streamwise velocity profiles.

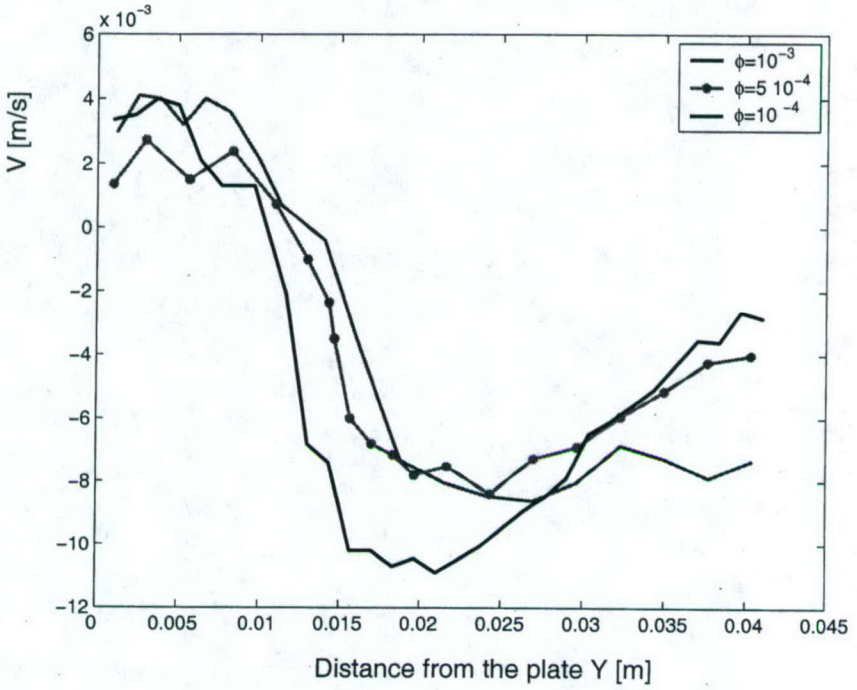

Figure 4.7: Wall-normal velocity profiles.

velocity normal to the wall, for different values of the Reynolds number and void fraction. It can be seen that the flow normal to the wall does not vary with the Reynolds number but rather it is strongly dependent on the bubble void fraction in the boundary layer, becoming stronger as the void fraction increases. This hypothesis is supported by figure 4.8 in which the wall-normal velocity is plotted against the distance from the wall, both normalized with viscous scales. The lack of a collapse of both curves seems to indicate that this secondary flow normal to the wall is caused by the presence of the bubbles, not by the dynamics of the turbulence near the wall.

Measurements of the vertical velocity of both the bubbles and the carrier flow were conducted at the same depth and distance downstream as the previous measurements. The vertical laser plane, parallel to the flat plate, was positioned at three different distances from the wall, namely at 8, 13 and 18 mm. These three positions are located in the three different subregions determined by the spanwise

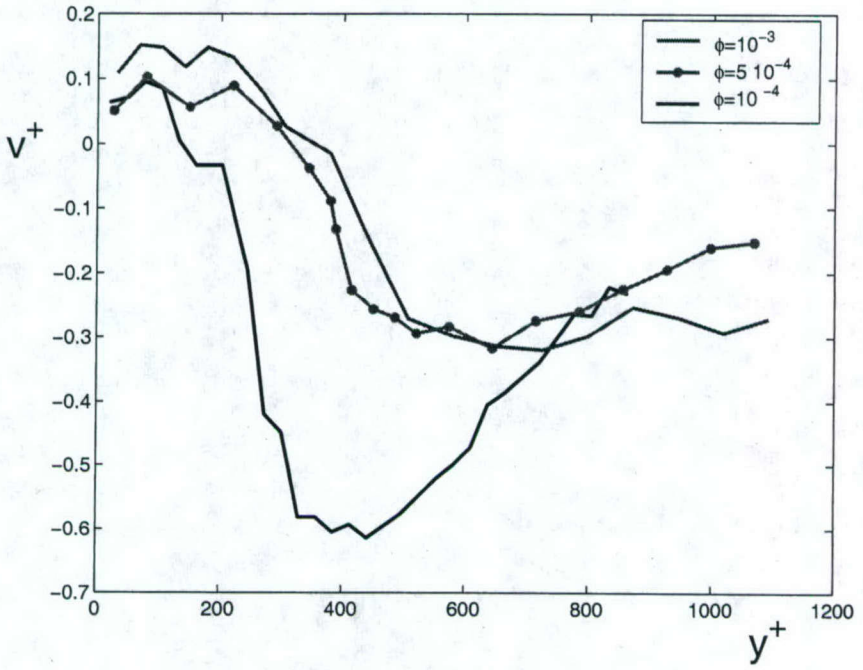

Figure 4.8: Spanwise velocity profiles. Non dimensionalized using viscous scaling.

velocity profiles, that is in the region where the normal velocity is away from the wall, at the line where the normal velocity is zero, and in the region where the normal velocity is towards the wall. In this way, the relation between the secondary flow normal to the wall and the vertical flow induced by the buoyancy of the bubbles can be confirmed. The vertical velocity profile is plotted in figure 4.9. The coordinate in the x axis is the streamwise velocity, used as a surrogate of the distance from the wall. As seen in figure 4.5, inside the boundary layer there is a one to one correspondence between the mean streamwise velocity and the distance from the wall.

The number density and diameter of the bubbles were also measured. The distribution of bubbles is plotted in figure 4.10, against the streamwise velocity which, as explained above, serves as a surrogate of the distance from the wall. It can be seen that the number density of bubbles is not uniform within the boundary layer. It grows from almost zero near the wall to a very sharp maximum, and

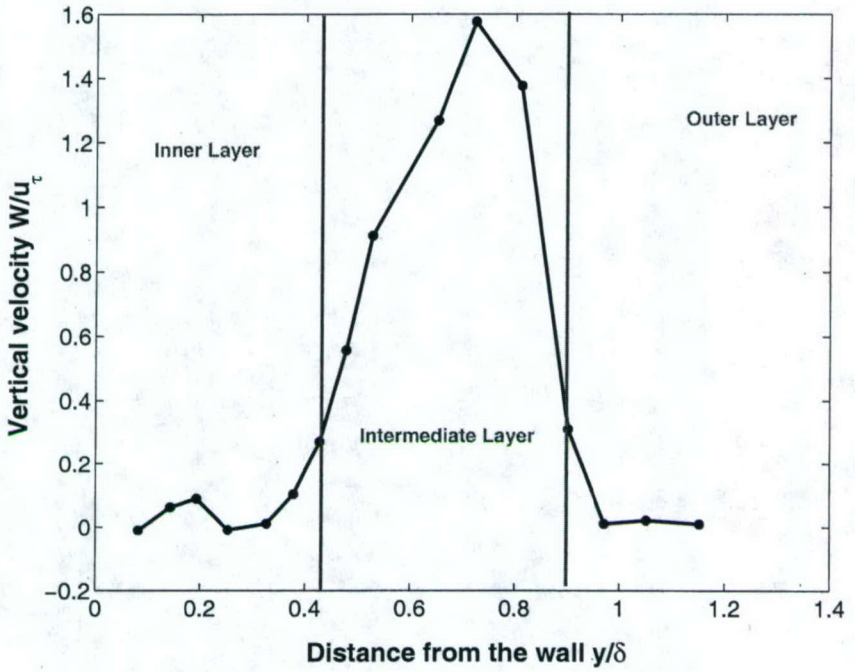

Figure 4.9: Vertical velocity profiles.

decays back to zero as the distance from the wall grows. The volume-averaged diameter of the bubbles is also plotted against the streamwise velocity, in figure 4.11. There is significant size segregation occurring inside the boundary layer. The average diameter is very small, of the order of 100 μm, in the region closest to the wall. It grows significantly, up to a value of 200 μm in the intermediate region, corresponding to the location of the maximum of the vertical velocity. Then, the average bubble size goes down quickly as we move away from the wall, past the maximum of the vertical velocity profile.

The vertical velocity of the bubbles measured at these three locations, corresponding to the three sublayers described above, was averaged for bubbles with equal diameter. The rise velocity of the bubbles computed by this method is compared in figure 4.12 against the rise velocity of micro bubbles in still fluid measured by Detsch (1989). It is clearly observed that the behaviour of the bubbles is different depending on their position with respect to the wall. The rise velocity

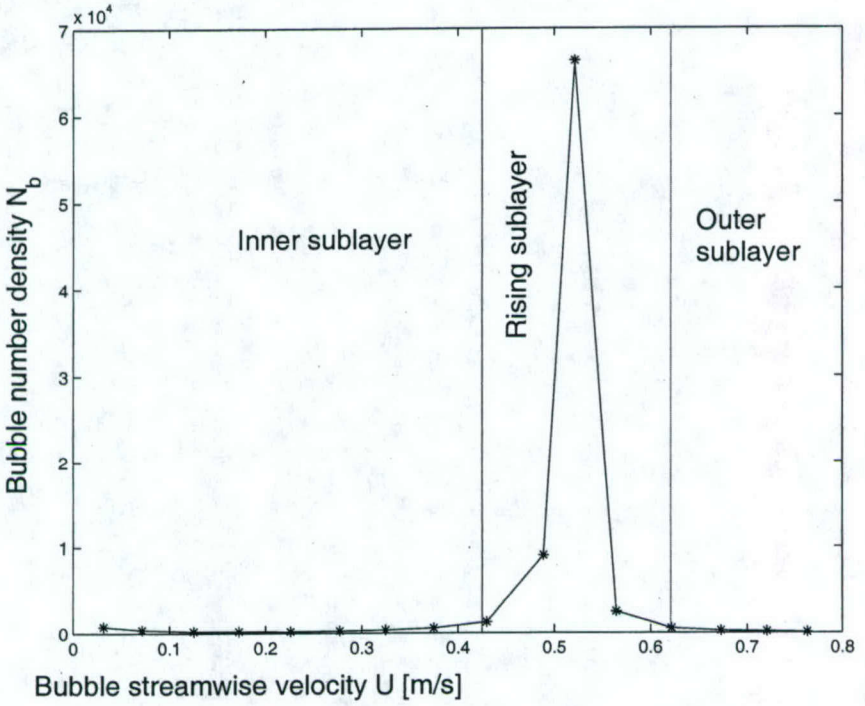

Figure 4.10: Bubble number density as a function of the distance from the wall.

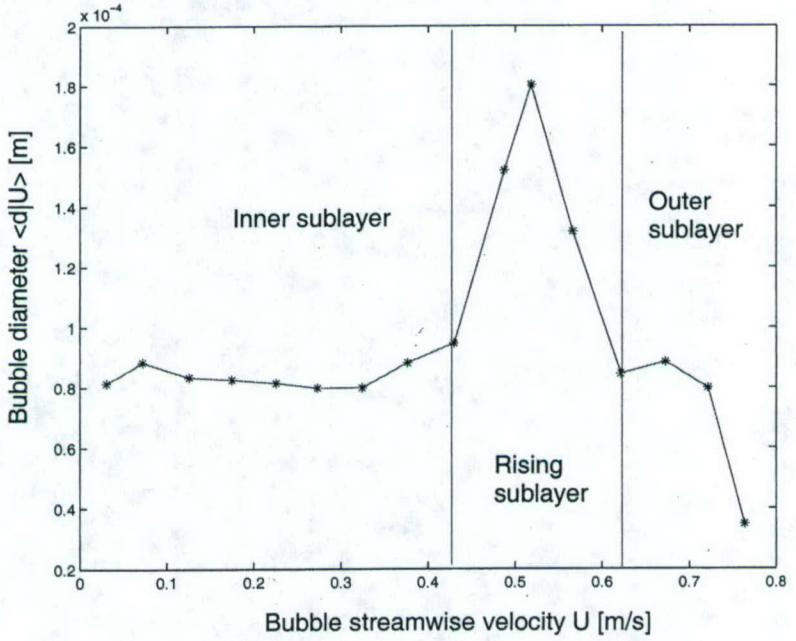

Figure 4.11: Volume averaged diameter of the bubbles as a function of the distance from the wall (d_{30}).

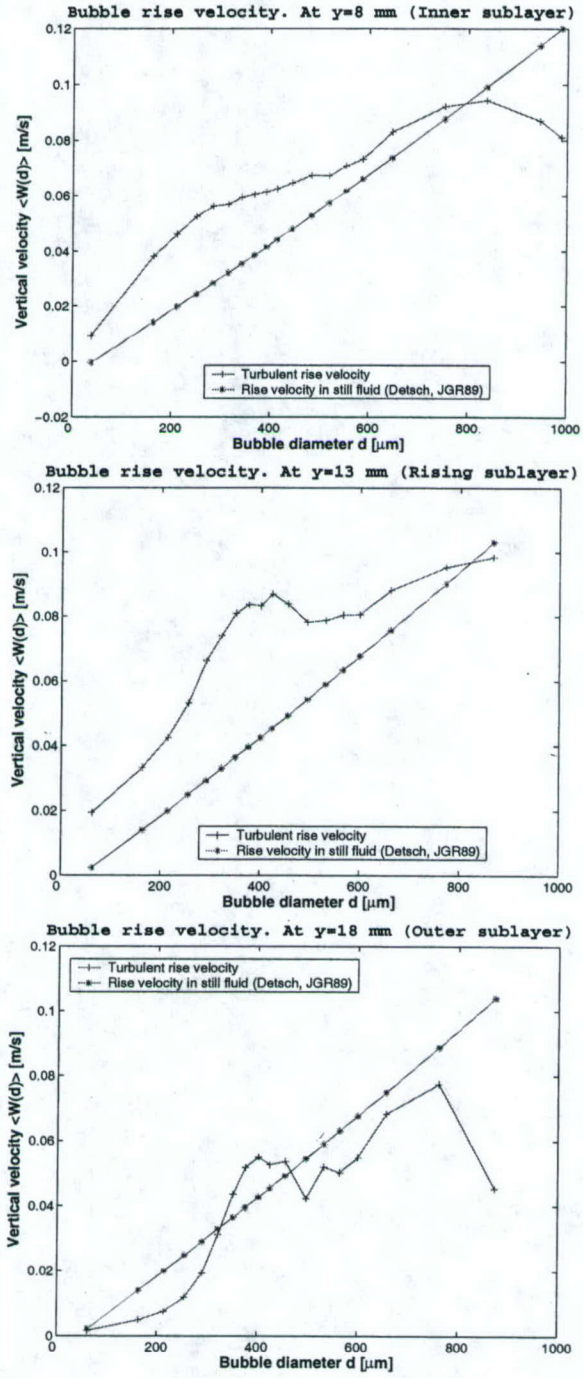

Figure 4.12: Average rise velocity of the bubbles as a function of their diameter, conditioned to the position inside the boundary layer. *a*) y=8 mm, *b*) y=13 mm, *c*) y=18 mm.

of bubbles inside the inner layer is similar to the one measured in still fluid. It is slightly enhanced for the smallest bubbles and slightly reduced for the largest bubbles. Inside the intermediate layer, where the vertical velocity of the carrier fluid reaches its maximum, the rise velocity is significantly enhanced for bubbles of all sizes. For bubbles in the outer layer, however, rise velocity is equal or even smaller than the still fluid value. In particular, the largest bubbles present in this sublayer have a reduction in the rise velocity of up to 50%.

4.2.2 Bubble accumulation due to the turbulence

The positions of the bubble centroids were determined by the image processing technique described in Chapter 5.2. This information was evaluated by different algorithms to characterized how the instantaneous bubble concentration field correlated with the turbulent structures present in the flow. The algorithm used to identify bubble clustering by the turbulence consists of the following steps. First, each image is divided into square windows of a certain size. The number of bubbles within each of these non-overlapping windows is counted and recorded. With the information corresponding to all the windows covering every image taken under given conditions, one can compute the density function for the probability of finding a number of bubbles $P(n_b)$ in one of these windows. If the bubbles were passive, their spatial concentration due to the random stirring of the turbulence would correspond to a Poisson distribution.

$$P_{poisson}(n) = \frac{e^{-\lambda} \cdot \lambda^n}{n!} \tag{4.2}$$

where λ is the mean number of particles per window, N_b/N_w, and P(n) is the probability of finding n bubbles in a window, and $\sigma_{poisson}$ is the standard deviation of the Poisson distribution. By comparing the observed Probability Density Function with the theoretical Poisson PDF resulting from a purely random process, it is possible to quantify how the bubble concentration field deviates from randomness. By repeating this algorithm for different window sizes, the depen-

dency of this deviation on the length scale can be determined. Two different ways of comparing the PDF's, which have been used consistently in the literature, were employed to quantify the extend of bubble clustering in the boundary layer. Their definitions, due to Wang & Maxey (1993*a*) and Fessler *et al.* (1994) respectively, are as follows:

$$D_{sum} = \sum_{n=1}^{N_b} (P(n_b) - P_{poisson}(n_b))^2. \tag{4.3}$$

$$D_{sigma} = \frac{\sigma - \sigma_{poisson}}{\lambda} \tag{4.4}$$

The values of these quantities, computed for many different window sizes are plotted in figure 4.13. Both indicators of preferential accumulation present a maximum for a length scale of 100 wall units. This is the flow scale at which bubble accumulation is most significant. The two quantities plotted tend to zero for very small and very large scales, as is expected as accumulation due to turbulence must disappear for scales smaller than the smallest scale in the flow, viscous length, or larger than the largest turbulent scale, the boundary layer thickness.

4.3 Analysis and discussion of the results

In the previous section, the differences that this bubbly flow presents with respect to its single phase counterpart were described. In this section, the physical mechanism by which the presence of the bubbles in the boundary layer perturbs the base flow and induces those drastic changes is analyzed.

4.3.1 Velocities inside the boundary layer

The parameters of the logarithmic law that fits the velocity profile were found to depend on the local void fraction. An offset from the wall was introduced as a new parameter in an effort to find a universal fit to the streamwise velocity profile in the logarithmic layer for the different values of Reynolds number and

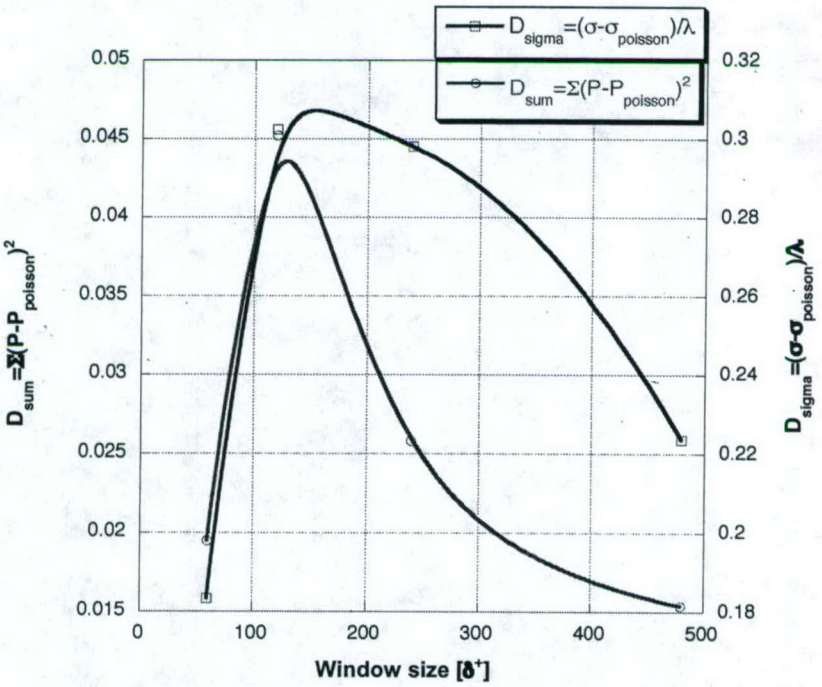

Figure 4.13: Bubble accumulation as a function of the length scale. Indicators defined in Eqs. 4.3 and 4.4

bubble void fraction. The results can be seen in figure 4.14. A systematic dependency of the wall offset with the local void fraction was found, and it is shown in figure 4.15. As the lack of an independent measurement of the wall shear stress makes it impossible to estimate a best fit, DeGraaf & Eaton (2000), the value of the wall offset was computed for two sets of parameters from single phase boundary layer studies, Coles (1956) and Zagarola *et al.* (1997). In both cases, the offset was consistently dependent on the bubble void fraction, increasing as the void fraction increases. This simple model provides a way of relating the velocity profile of the bubbly boundary layer with the well known logarithmic profile of the single phase turbulent boundary layer. Thus, the transport of bubbles can be computed without the need to take into account the interaction of the bubbles with the carrier flow.

A secondary flow, two orders of magnitude smaller than the channel mean velocity is established within the boundary layer. The characteristics of this flow normal to the wall, unlike the single phase case, consist of a small region near the wall where the flow is moving away from the wall, and a larger region, in the outer zone of the boundary layer, in which there is a relatively strong flow towards the wall. The flow in these two regions converge to a line which is located between 10 and 15 mm from the wall, for the Reynolds numbers and void fractions studied. By continuity, these converging flows have to go out of the plane and, as shown by the vertical velocity measurements described below, they do flow upwards.

This variation, when considered together with the size segregation shown in figure 4.11, explains the existence of the three sublayers within the boundary layer and the two regions of strong vertical shear. One can see the strong variation of the diameter in three sublayers, that resembles the vertical velocity profile. The strong inhomogeneity in the distribution of the buoyancy, coupled by the zero vertical velocity boundary conditions at the wall and in the free stream, leads to the development of the highly sheared vertical velocity profile, seen in figure 4.9. The entrainment of carrier fluid by the buoyantly rising sublayer induces the secondary

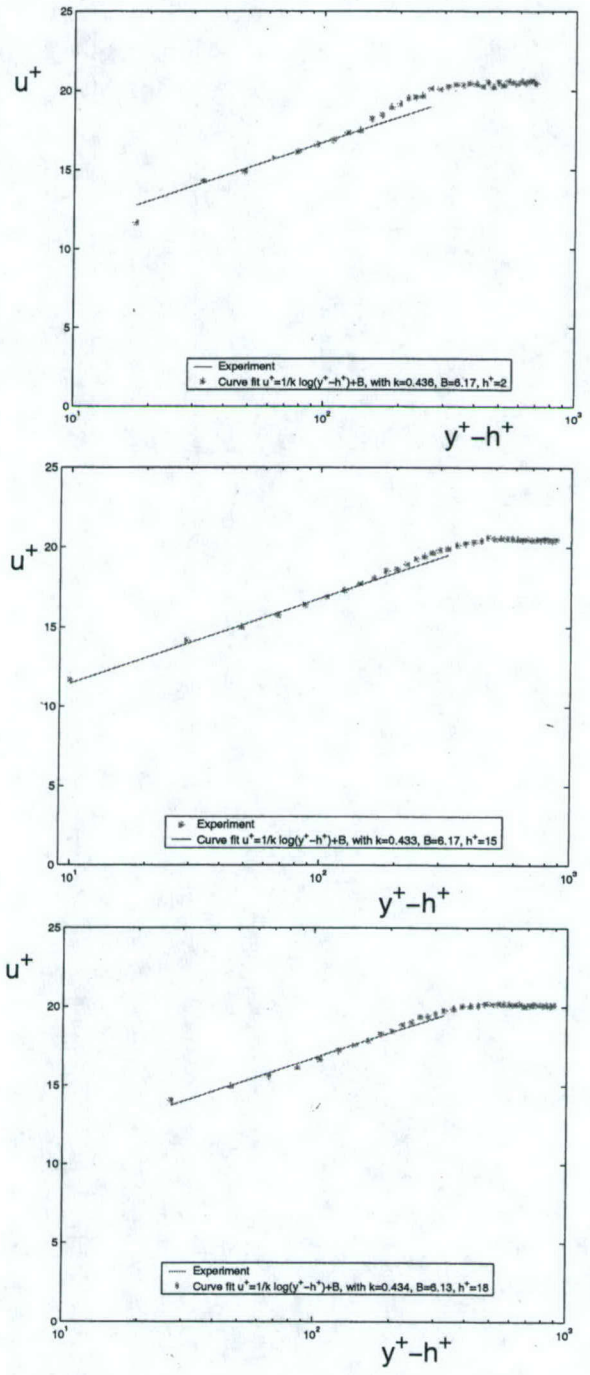

Figure 4.14: Normalized streamwise velocity profiles. Wall offset dependency on the bubble void fraction.

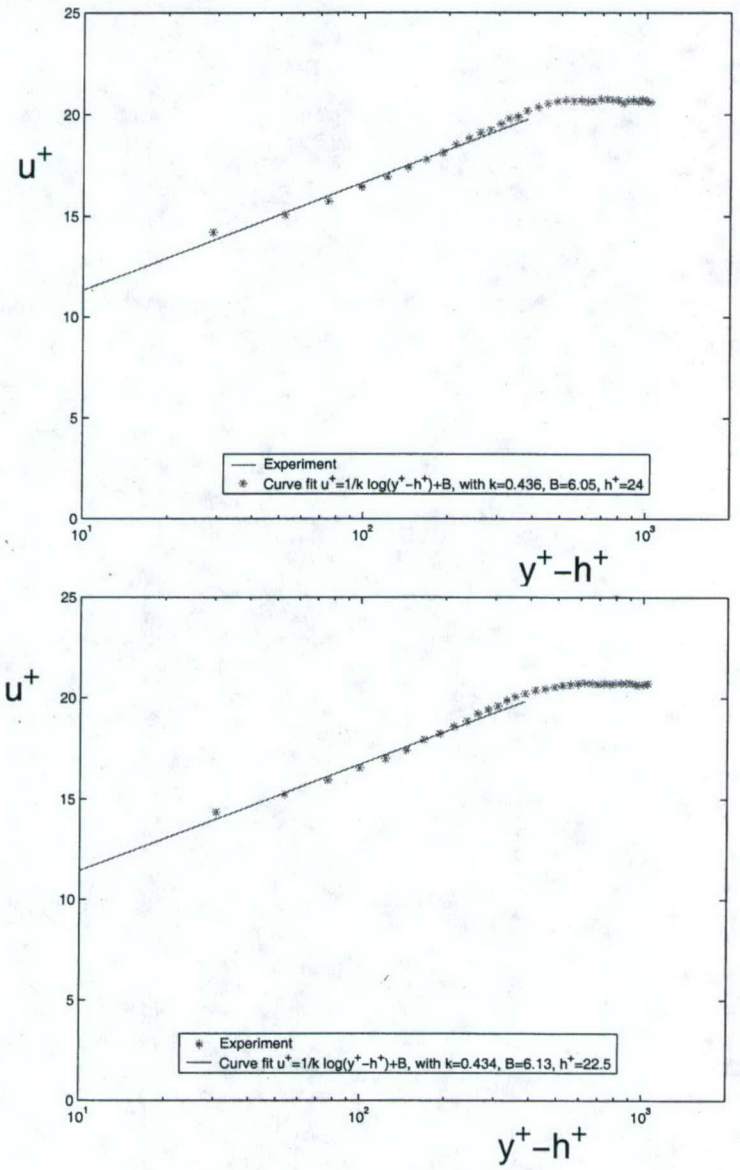

Figure 4.14: continued

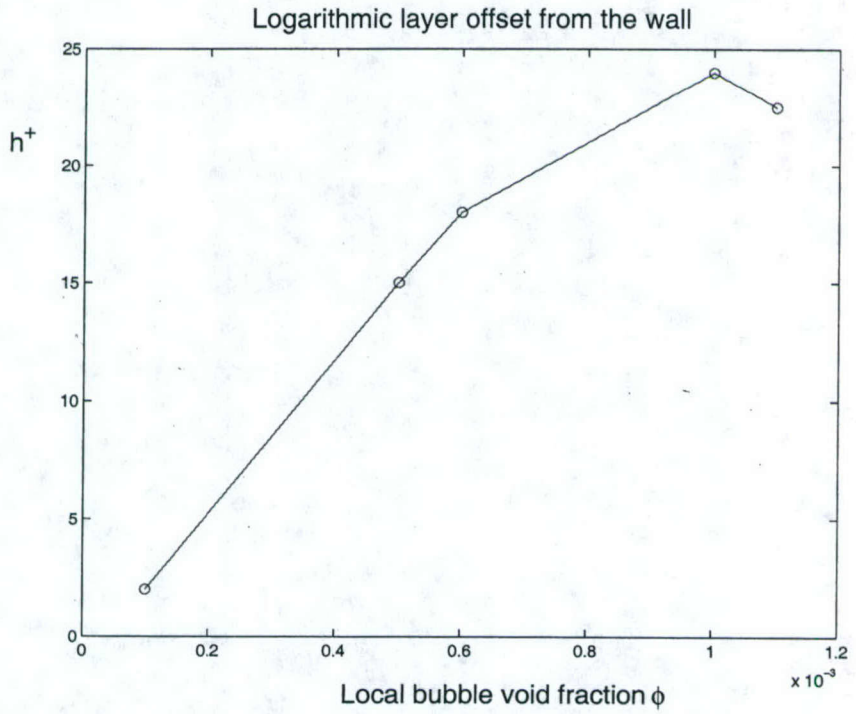

Figure 4.15: Offset from the wall of the logarithmic layer, as a function of the local bubble void fraction.

flow normal to the wall that was found in figure 4.7.

One can clearly identify three sublayers within the boundary layer. In the inner layer closer to the wall, the vertical velocity is very small, restricted by the presence of the wall. The intermediate layer has a very large vertical velocity, with two areas of high shear of opposite sign. Finally, the outer sublayer has very low vertical velocity, asymptotically going to zero as we approach the free stream. The presence of these three sublayers within the boundary layer affects the average rise velocity of the bubbles. As shown in figure 4.12b, the bubbles in the intermediate layer, where the entrained fluid have maximum vertical velocity, rise faster than they would in still fluid. This is in apparent contradiction with the hindering of the rise velocity of bubbles by turbulence that has been reported from numerical simulations, Maxey *et al.* (1997) and Mazzitelli *et al.* (2003), as well as experiments, Poorte & Biesheuvel (2002). Obviously, this contradiction is simply due to convection. The non zero value of the local vertical velocity of the carrier fluid adds up to the rise velocity of these bubbles that can be computed by a balance between viscous drag, which depends on the slip velocity, and buoyancy.

$$\begin{aligned}
\frac{\pi}{6}d^3(\rho_b-\rho_f)\overrightarrow{g} &= \tfrac{\pi}{4}d^2 C_D \rho_f |\overrightarrow{v}-\overrightarrow{u}|(\overrightarrow{v}-\overrightarrow{u}) \quad ; \; C_D \approx \frac{24}{Re} \\
\frac{\pi}{6}d^3(\rho_b-\rho_f)\overrightarrow{g} &= \tfrac{\pi}{4}d^2 \tfrac{24\nu_f}{|\overrightarrow{v}-\overrightarrow{u}|d}\rho_f |\overrightarrow{v}-\overrightarrow{u}|(\overrightarrow{v}-\overrightarrow{u}) \quad ; \; \frac{\rho_b}{\rho_f} << 1 \\
v_z &= u_z + \tfrac{d^2 g}{36\nu_f}
\end{aligned} \tag{4.5}$$

where v_z is the bubble vertical velocity, u_z is the carrier fluid vertical velocity, d is the bubble diameter and ν_f is the kinematic viscosity of the carrier fluid. The simplifying assumption of $C_D = 24/R_e$ has been made for illustration purposes only. The rise velocity is still fluid with which the measured bubble velocity is compared in figure 4.12 was experimentally determined, Detsch (1989), and takes into account nonzero Reynolds number and surfactant effects.

In both the inner and outer layer, the effect of the turbulence on the rise velocity of the bubbles was found to be strongest for the largest bubbles. The rise

velocity of the small bubbles correlates only with the vertical convection velocity of the carrier fluid. In the inner layer the rise velocity is slightly increased due to the small upwards velocity of the fluid, whereas in the outer layer the rise velocity is unaffected, corresponding to the zero mean vertical velocity in this sublayer. The rise velocity of the large bubbles is reduced in both cases due to the turbulent fluctuations, see figures 4.12a and 4.12 c. This reduction can be also glimpsed by looking at the difference between the vertical velocity of the bubbles in the intermediate layer and the one in still fluid. The increase in the bubbles rise velocity comes out to be much smaller than the peak velocity of the carrier fluid shown in figure 4.9, approximately 2 cm/s vs. 4 cm/s. This difference can be interpreted as a reduction of the rise velocity due to the turbulence.

4.4 Conclusions

The dynamics of a turbulent boundary layer laden with micro bubbles have been studied experimentally. The configuration chosen for the study was a vertical surface piercing flat plate, with the air bubbles injected at the leading edge into the horizontal water flow. In this way, the bubbles kept confined to the boundary layer, as they were convected by the carrier flow and rise under the effect of buoyancy. The presence of a relatively high void fraction of bubbles inside the boundary layer introduced a source of momentum perpendicular to the free stream, generating secondary flows in the vertical and wall normal directions. The presence of these secondary flows had a very significant effect on the transport of the bubbles, as well as on the statistics of the mean carrier flow.

The logarithmic layer, typical of a single phase turbulent boundary layer, was modified by the presence of the bubbles. It was found that a logarithmic fit that preserves the canonical values of the constants described in the single phase literature could be used, with the addition of a new constant. This constant represents an offset in the distance from the wall, that is a function of the void

fraction.

The secondary flows induced by the buoyancy inside the boundary layer, created three sublayers with distinct values of the bubble number density, average diameter and rise velocity. The inner sublayer was characterized by the presence of flow normal to the wall and away from it, coupled with low positive values of the vertical velocity. It was found to be populated by a low number of relatively small bubbles, $d_{10} = 100\ \mu m$, which had their rise velocity enhanced compared to the value in still fluid. The intermediate sublayer presented a maximum of the vertical velocity, corresponding to the region where the wall-normal flow was zero. The largest bubbles accumulated almost exclusively in this sublayer, resulting in a marked increase of the average diameter, $d_{10} = 200\ \mu m$, and a very large increase of the bubble number density. As a result of the large vertical velocity of the carrier fluid, the rise velocity of bubbles of all sizes in this sublayer was significantly increased. Finally, in the outer layer the vertical component of the velocity was essentially zero and the wall normal component was strongly negative, that is, directed towards the wall. This sublayer had the smallest bubble number density and average diameter, $d_{10} = 80\ \mu m$, resulting from the difficulty of the bubbles to diffuse into a region where both the wall normal velocity and the vertical shear are negative. Unlike the other two sublayers, the rise velocity of the bubbles was reduced due to the turbulence and the zero value of the carrier fluid vertical velocity.

Chapter 5

The characteristics of bubbly junction flow at the intersection of the free surface with a solid wall

5.1 Introduction

The flow at the intersection of two boundaries, a solid wall characterized by the no slip condition, and a free surface which imposes a stress free condition, is investigated in this chapter. This type of flow develops as a consequence of the configuration chosen to study the bubbly turbulent boundary layer. The vertical plate pierces the free surface in the channel and the resulting flow that develops locally near the two surfaces is dominated by both the presence of the bubbles and the boundary conditions.

The single phase flow that exists at the juncture between a solid boundary and a free surface has been experimentally and numerically studied by Stern and collaborators, Sreedhar & Stern (1998) Longo *et al.* (1998). The Reynolds averaged statistics revealed two counter-rotating streamwise vortical structure of relatively weak intensity. The turbulent boundary layer was observed to thicken close to the free surface. These two effects are attributed to imbalances in the Reynolds

stresses at the juncture. Numerical simulations and experiments by Grega et al., Grega *et al.* (1995) Grega *et al.* (2002), confirmed the existence of two streamwise vortices at the juncture region. The inner vortical structure flows towards the wall near the free surface and downwards along the wall. The outer one takes low momentum fluid from the boundary layer upwards around the inner region and towards the free surface. At the free surface it flows away from the wall, causing the thickening of the boundary layer. These secondary flows are very weak, with mean velocities of the order of 1% of the mean flow.

The characteristics of flow in this region were found to be greatly affected by the rising of the bubbles along the plate towards the free surface. Visualizations were conducted to provide the qualitative features of this complex flow. The vorticity field inside the boundary layer and at the junction region was visualized by the light reflected from the bubbles and by dyeing the flow with fluorescein. The experimental results showed a very complex pattern of vortical structures that have some similarities and strong differences to the single phase flow.

5.2 Experimental technique

Flow visualizations were obtained using a Canon Optura digital video recorder and stored in Mini-DV format tape. Except in a few cases where ambient light was used, in most instances the flow was illuminated by a laser plane created using a continuous Coherent I-70C Ar^+ laser and a Lincoln Laser Co. rotating mirror operating at 500 Hz. The plane could be oriented to illuminate a vertical slice of the flow, perpendicular to the free stream flow, as indicated by the sketch in figure 5.1a. The camera was situated at the end of the channel, looking into the test section through a plexiglass window in the channel's end-wall. The laser plane could also be positioned horizontally, perpendicular to the flat plate, as shown in figure 5.1b, cutting across the boundary layer. In this case, the camera was located under the test section looking up, through the transparent channel floor. Finally,

the flow was also illuminated by a vertical laser plane parallel to the flat plate and the free stream in the test section. To do this the rotating mirror was located under the test section and the camera looked horizontally into the test section through the transparent walls, see figure 5.1c.

5.3 General flow features

A top view of the flow is shown in figure 5.2. In this picture of the water channel, the flow moves from top to bottom and the surface-piercing flat plate, located at the middle of the channel's test section, with the bubbles being injected on its left side can be seen at the right edge of the picture. The free surface presents a typical Kelvin wave, with a set of capillary waves radiating from it, produced by the presence of the plate. A foamy line can be observed starting at the leading edge of the plate, separating from it and becoming parallel to the plate at a certain distance. This is, as explained in Chapter 4.3, the surface signature of a submerged streamwise vortex that develops near the juncture.

A horizontal slice of the flow is visualized in figure 5.3. It shows a cross cut of the bubbly boundary layer, as well as some features of the outer juncture flow. The flow is from right to left. The boundary layer is tripped by the bubble injector and the bubbles themselves making the bubbly boundary layer considerably thicker than the single phase case for an equivalent Reynolds number based on the distance downstream. As it develops, bubbles diffuse inside the boundary layer but, it can be clearly seen from figure 5.4, they keep confined to it, not diffusing into the free stream. Some surface features are made visible by multiple scattering of the laser light from the regions where bubbles accumulate. A close up of this view is shown in figure 5.4. Non uniformities in the bubble concentration field, resulting from the interaction of the bubbles with the turbulent structures present inside the boundary layer, are apparent.

A snapshot of the flow illuminated by a vertical laser plane, perpendicular

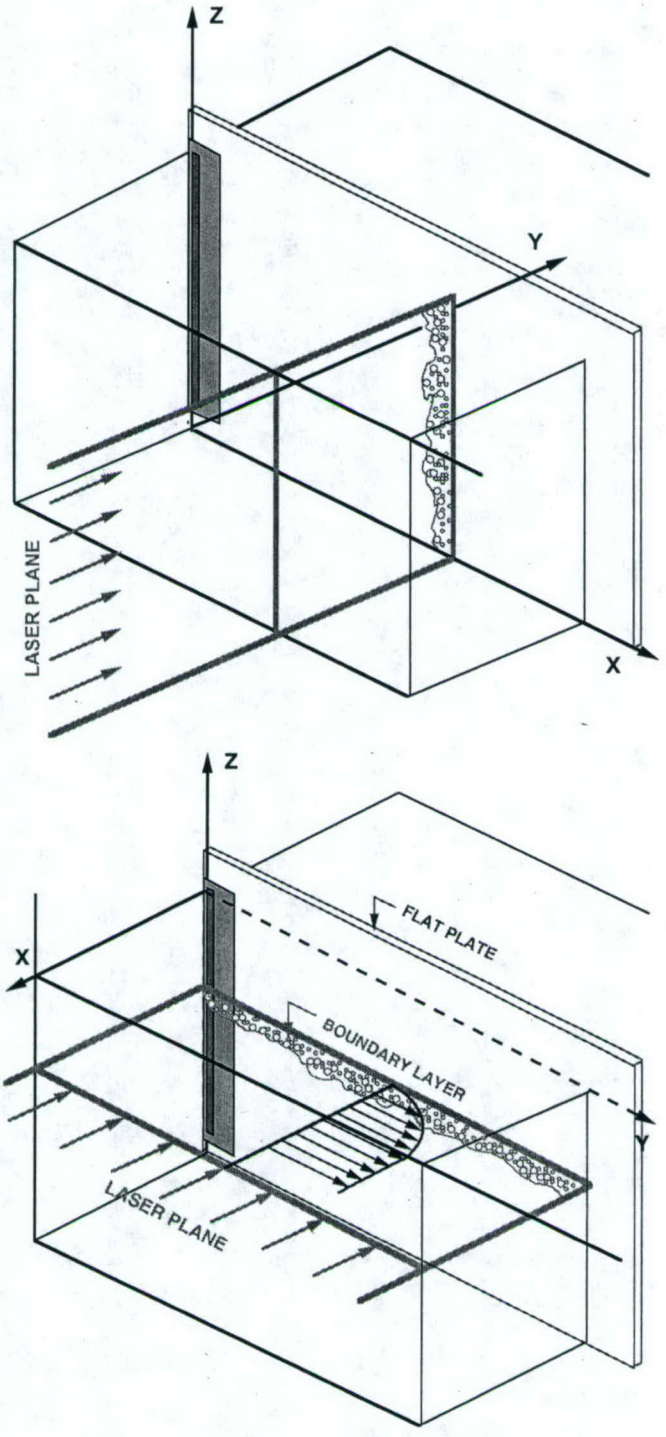

Figure 5.1: Sketch of the Laser plane orientations for flow visualizations.

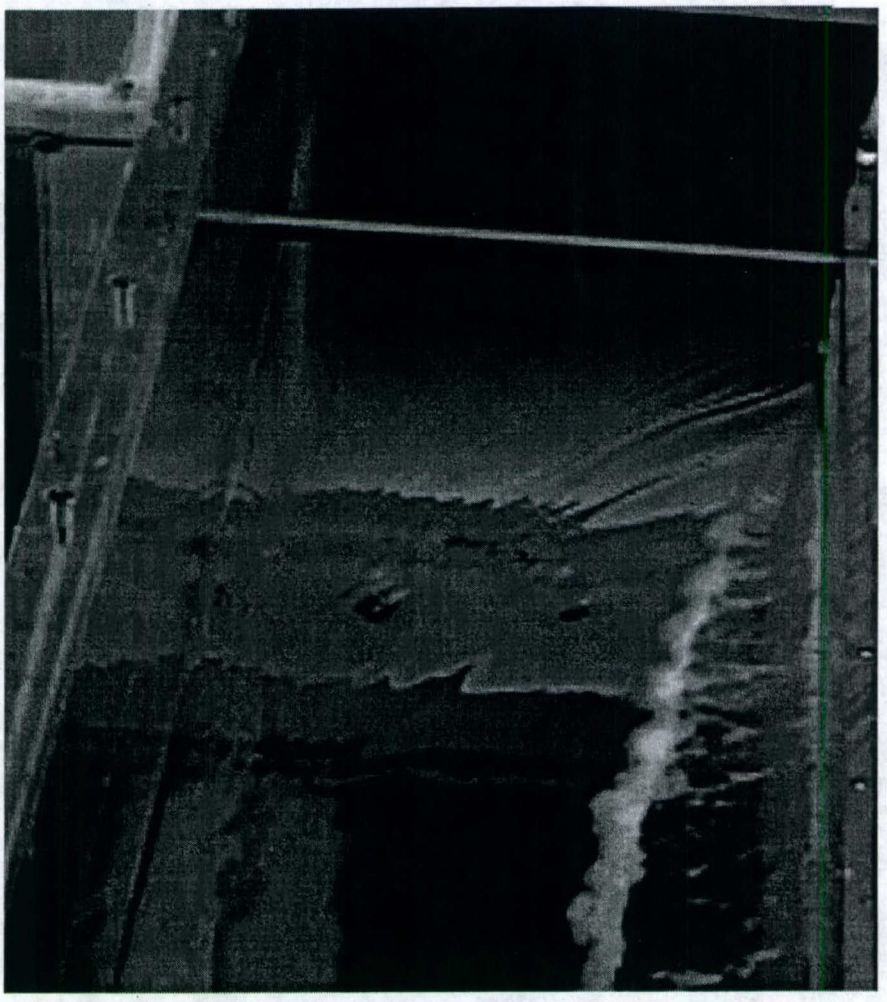

Figure 5.2: Overall view of the flow facility.

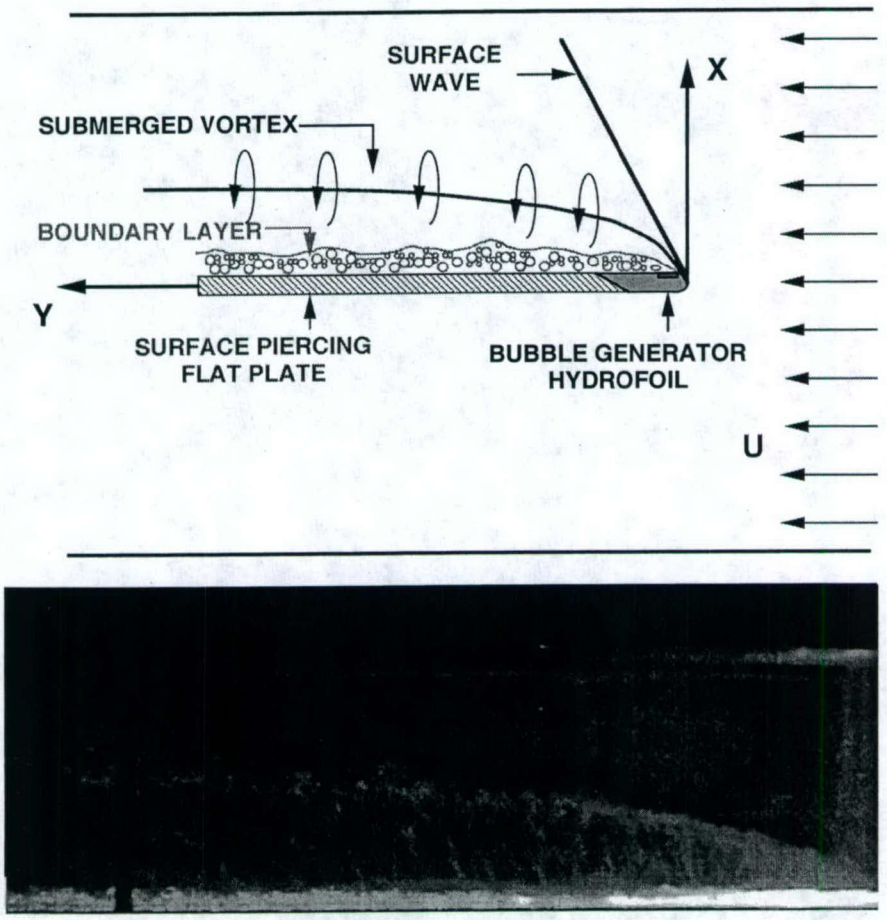

Figure 5.3: Horizontal cut. General View

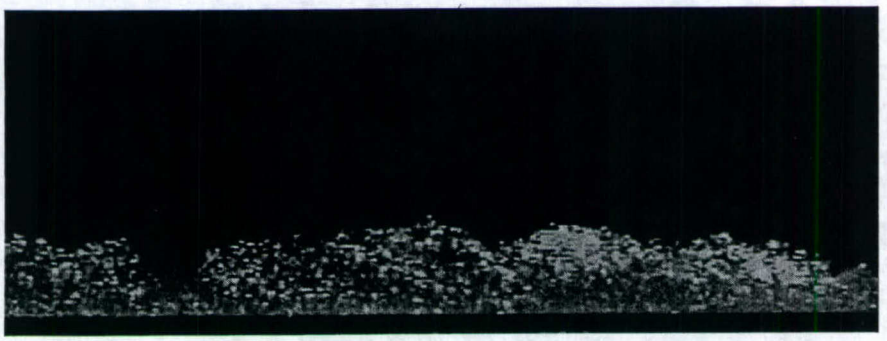

Figure 5.4: Horizontal cut, close up. Instantaneous bubble concentration field.

to the free stream flow, is shown in figure 5.5. The most outstanding feature of this flow is the existence of a streamwise vortex located at a certain distance and depth with respect to the plate. This large coherent structure has circulation of the same sign as the outer vortex described in single phase juncture flows, Sreedhar & Stern (1998) and Grega *et al.* (2002). Its strength, however, is much larger. A source of streamwise vorticity associated with the presence of the bubbles is described in the Chapter 4.3.

To further clarify the origin of the strong coherent vortex seen in the previous figure, and to determine its relationship with the vorticity that has been described in single phase juncture flows, we performed visualizations with fluorescein injected on both sides of the plate. In figure 5.6a, one can observed how the fluorescein introduced in the flow near the bubbly side of the plate is convected upwards and entrained by the vortex, alongside the bubbles. When fluorescein is introduced in the flow on the other side of the plate where there are no bubbles, shown in figure 5.6b, it diffuses slowly due to random fluctuations, with no visible coherency in the flow.

5.4 Effect of the bubbles on the overall flow features

The fluid inside the boundary layer rises along with the bubbles and, once it reaches the free surface, moves away from the plate, by continuity. A schematic of this is shown in figure 5.7. This surface flow carries the bubbles around before they have time to reach the surface and burst open. The effect of the bubble size on this surface flow away from the plate can be seen in figure 5.8. For the same bubble void fraction, the smaller bubbles are more effective at entraining fluid from the boundary layer, resulting in a larger flow rate induced at the surface and a wider angle separating the free stream and the surface flow.

The vertical velocity profile has been measured and shown to have two shear layers that will become unstable and roll up. In figure 5.9, which is a close

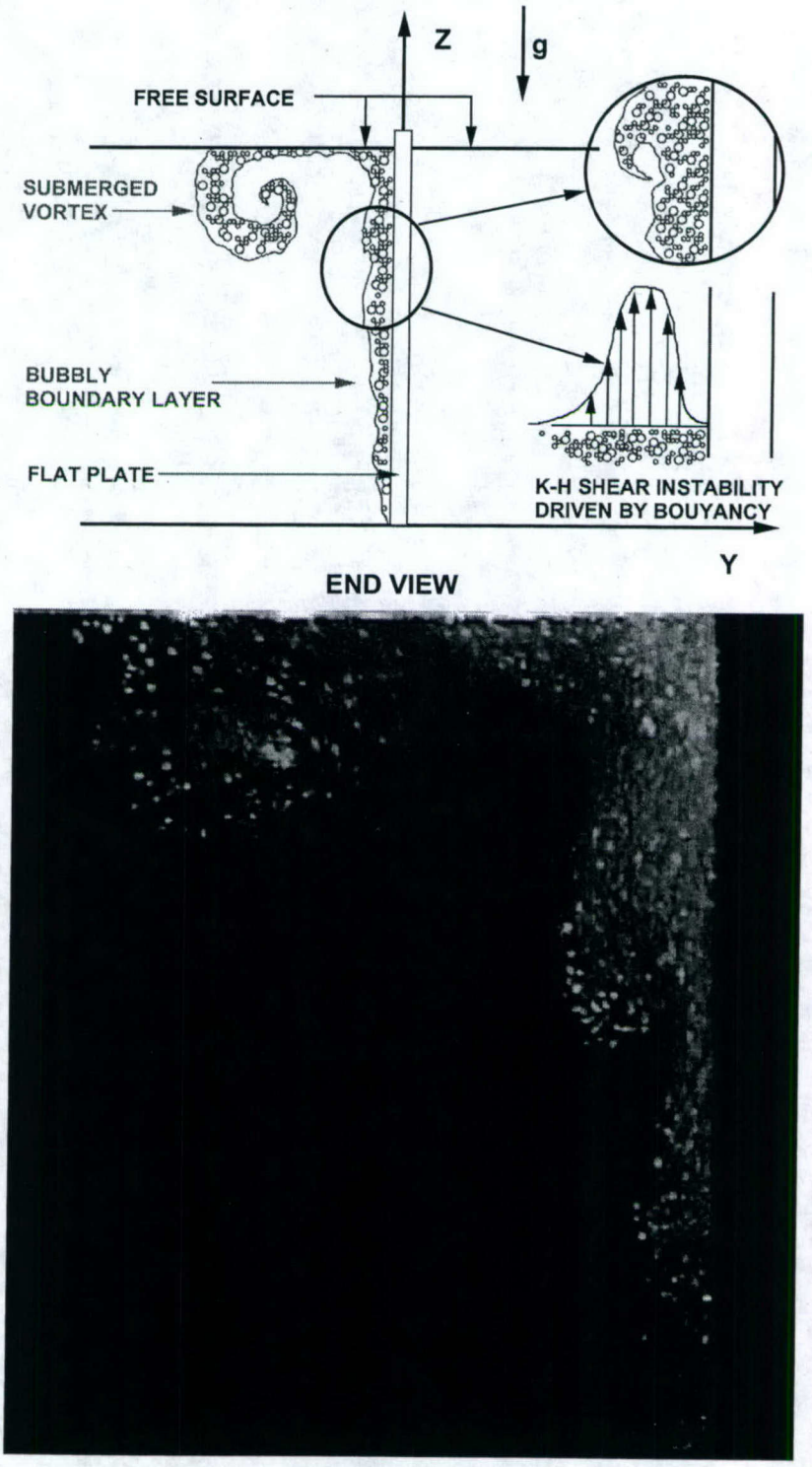

Figure 5.5: Vertical cut. General View

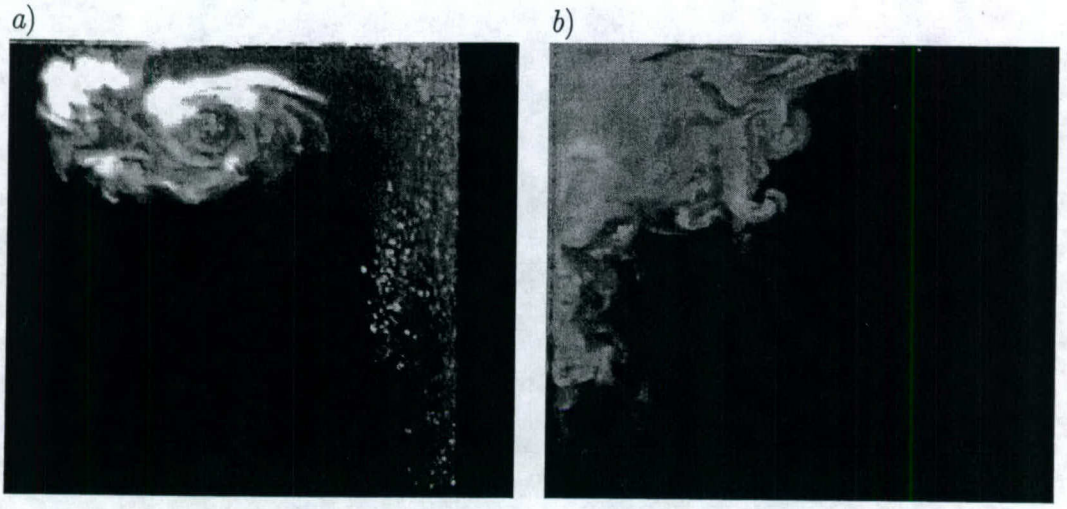

Figure 5.6: Fluorescein visualizations. *a*) Strong coherent structure on the bubbly side. *b*) No coherency on the single phase side.

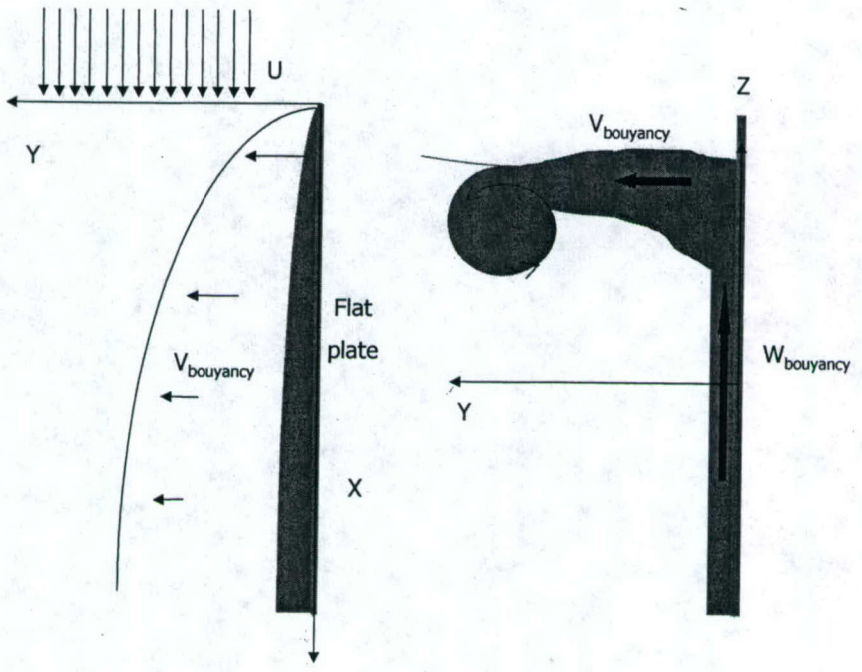

Figure 5.7: Schematic of the flow rising along the boundary layer and, at the surface, away from the plate

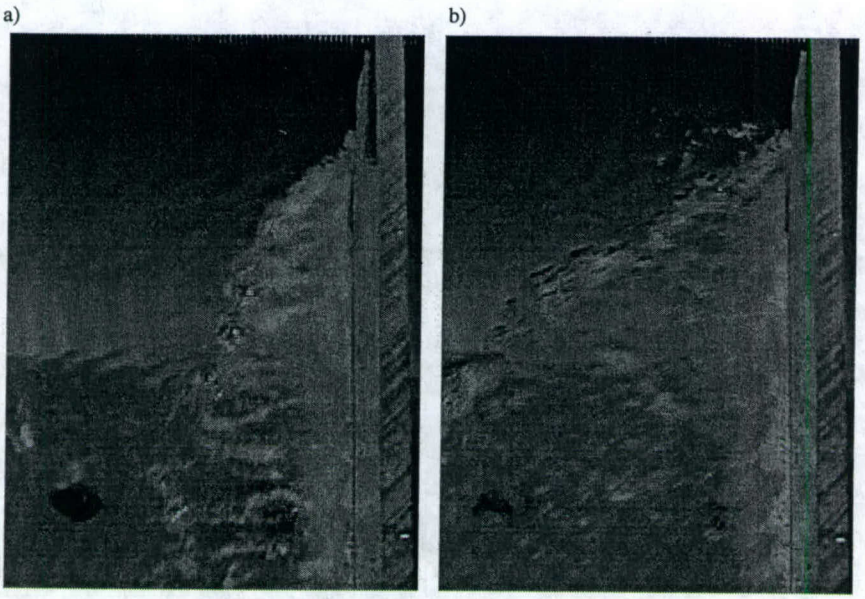

Figure 5.8: Effect of the bubble size on the induced surface flow. a) Sauter mean diameter =450 μm. b) Sauter mean diameter =250 μ.

up of figure 5.5, one can observe the roll up of the outer shear layer subject to a Kelvin-Helmholtz/Rayleigh-Taylor mixed type instability that generates positive streamwise vorticity. In this figure one can identify, by the presence of the streamwise billows at the interface between the bubbly layer and the free stream, the source of vorticity that ends up in the coherent vortex described above. Note that these billows have the same sense of rotation as the vortex, whereas there should be another shear layer very close to the wall, that generates vorticity of opposite sign. A sketch of the mechanism for this instability is shown in figure 5.5. This is a source of streamwise vorticity in the flow, which does not exist in the single phase boundary layer. The streamwise vorticity, resulting from the vertical shear, couples with the vertical vorticity present in the boundary layer as a result of the horizontal shear, see figure 5.10 . This coupling leads to a complex pattern of tilted vortex lines, a sketch of which is found in figure 5.11, that resembles those found by Thorpe (1985) and Atsavapranee & Gharib (1997) in stratified mixing layers inclined around two perpendicular axis. The vorticity generated in the boundary

Figure 5.9: Vertical cut. Close up of the Kelvin-Helmholtz-type billows present in the boundary layer.

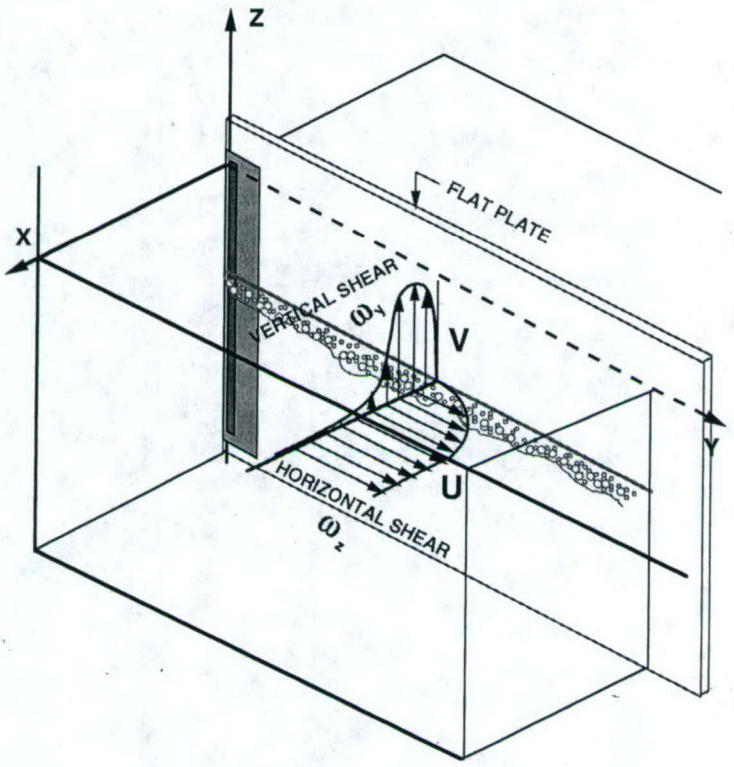

Figure 5.10: Schematic of the horizontal and vertical velocity profiles.

layer is advected upwards by the buoyant flow. Once they reach the surface, the vortex lines becomes parallel to it and reconnect in the form of a strong coherent streamwise vortex that positions itself at a certain depth and angle with the plate. These white filaments are made visible in figures 5.2 and 5.3 by the accumulation of bubbles near the cores.

The submerged streamwise vortex formed by the reconnection of all those vortex lines entrains the surface flow generated by buoyancy and thus serves as a demarcation line that divides the boundary layer flow, laden with bubbles, from the free stream that is unaffected by the presence of the bubbles. To corroborate this hypothesis, fluorescein was injected in the boundary layer. Figure 5.12 clearly shows the boundary layer fluid, marked with fluorescein for this visualization, rising to the surface and being entrained by the vortex. Thus, the vortex growth

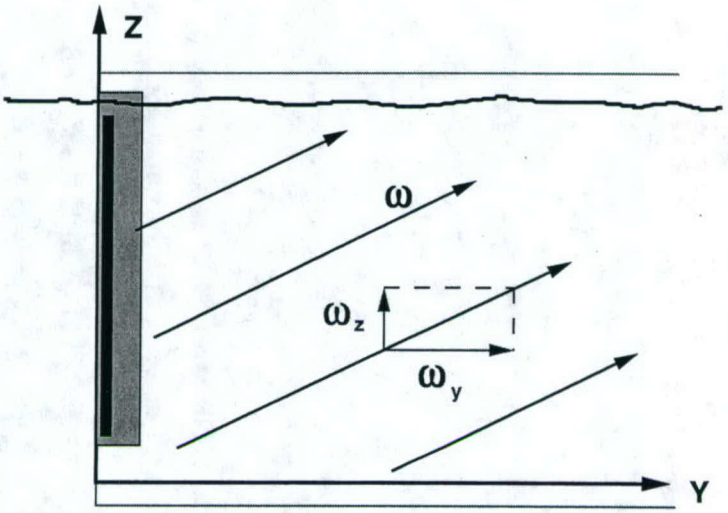

Figure 5.11: Schematic of the vortex lines pattern resulting from the coupling of the boundary layer vorticity with the buoyancy-induced streamwise vorticity.

and its separation from the plate is explained by the entrainment of the bubbly flow which carries positive vorticity. The vortex core captures bubbles from the boundary layer as they get near the surface. These bubbles remain near the vortex core for long times, coalescing until their size is large enough that they escape the vortex and rise to the surface. At the surface these large bubbles create a foamy pattern that helps locating the position of the vortex from the surface, in the visualizations shown above.

5.5 Conclusions

The bubble-laden junction flow at the intersection of a solid wall and a free surface has been investigated. This is the first time that this type of flows has been studied in the presence of bubbles. The results show a strong effect of the bubbles that make this flow qualitatively different from the single-phase one.

The flow is dominated by the presence of a strong coherent streamwise vortex that is submerged and located several boundary layer thickness from the wall. This vortex is reminiscence of the one described in the single phase junction,

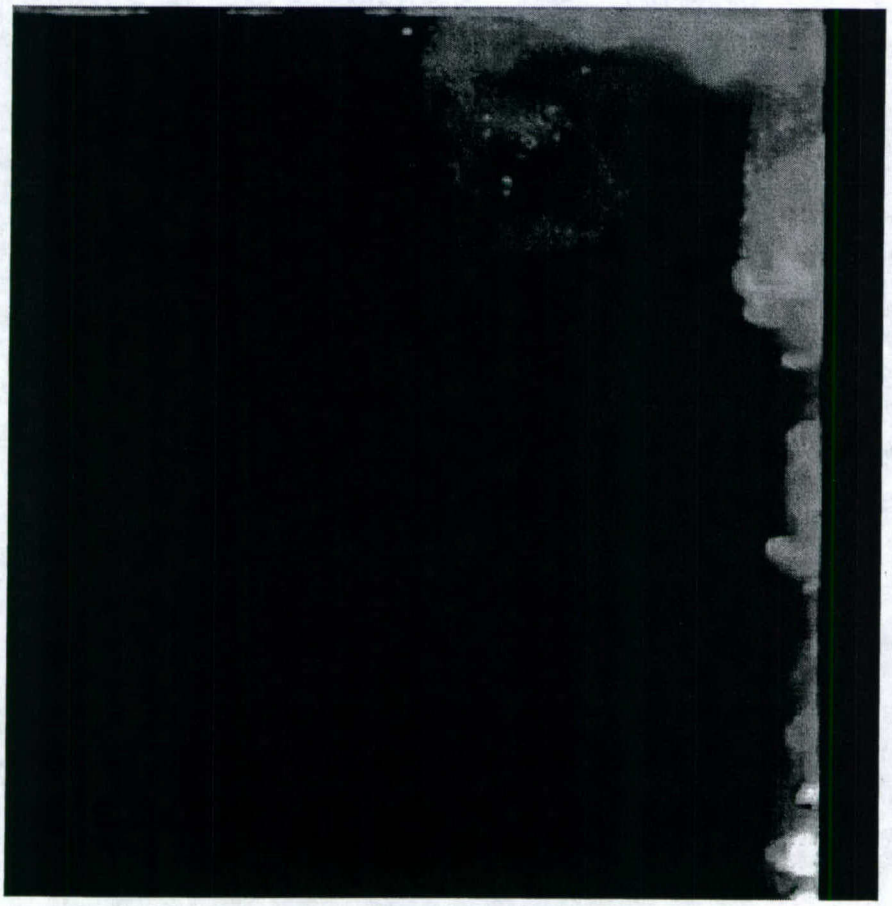

Figure 5.12: Vortex entraining boundary layer fluid. Fluorescein visualization.

but is much stronger and located at larger distance from the wall, The origin of this vortex is at the leading edge of the plate, as it is in the single phase case. The strength, however, can be explained by the instability of the sheared vertical velocity profile in the boundary layer, which coupled with the presence of a density gradient normal to the hydrostatic pressure gradient, acted as a source of streamwise vorticity. As a result of the interaction of the streamwise vorticity with the vertical vorticity present in the boundary layer, there was a complicated pattern of tilted vortex lines, which rose to the surface and were convected away from the wall and reconnected into a strong coherent streamwise vortex that dominates the junction flow. This vortex, which originated at the leading edge of the plate, laid at a depth and distance from the wall that were dependent on the Reynolds number of the flow and the bubble void fraction.

Chapter 6

Conclusions

Experimental studies of multi-phase turbulent flows have been conducted in order to address four questions that were identified in the introduction to be relevant to the understanding of these type of flows. Three different experiments were designed and carried out to study the effect of turbulence, with and without mean shear, on the concentration and on the gravitational drift velocity of spherical particles with much higher and much lower density than the carrier fluid.

The settling velocity of heavy particles and the rise velocity of bubbles were found to be significantly modified by the interaction with homogeneous isotropic turbulence. The effect of the local concentration of particles was found to be very strong, increasing the settling velocity as the local concentration increases, with a quasi-linear dependency. This gave rise to a simple model to capture the dependency of the settling velocity of the particles on the characteristics of both the turbulence and the clusters. The effect of the instantaneous bubble void fraction on the rise velocity could not be determined due to the different experimental conditions of the bubbles versus the particles.

The previous results are consistent with the hypothesis that heavy particles settling in a turbulent flow spend more time in the downwards side of the eddies, enhancing their settling velocity. By a similar reasoning, however, light bubbles would spend more time near the core of the vortices, where pressure and

drag forces would reduce their rise velocity.

When mean shear was present in the carrier flow, as is the case of the turbulent boundary layer, the rise velocity was found to be strongly influenced by both the turbulence intensity and the bubble void fraction. The presence of a solid wall lead to the development of large scale spatial inhomogeneities in the average bubble void fraction, which induced secondary flows that changed the character of the flow. Accumulation of buoyancy in certain subregions within the boundary layer created an upward motion of the carrier fluid which enhanced the rise of the bubbles in these regions. The interaction of the bubbles with the turbulent structures reduced the rise velocity in the regions where there was negligible vertical velocity of the carrier fluid, in agreement with the results from the unbounded case.

Preferential accumulation of particles and bubbles was found in all experiments. The length scale for which this accumulation is highest, however, was found to differ for different cases. In the first experiment, at a Reynolds number of 10^5, heavy particles accumulate in regions of high strain and low vorticity and the optimal length scale for accumulation was found to be of the order of ten times the Kolmogorov length scale. In the second experiment, at a higher Reynolds number of 0.5 10^6, bubbles accumulate near the core of the vortices, where the pressure is lowest. The preferred length scale for accumulation was found to be 20 η. This could be due to the accumulation in different regions of the flow, or to the different vorticity spectrum in these finite Reynolds number flows, where the peak of the vorticity spectrum shifts slowly with the value Reynolds number. For the turbulent boundary layer experiments, the bubbles were found to concentrate in an average sense, as well as in the instantaneous sense. The average accumulation is caused by the shear imposed by the presence of the wall. The instantaneous accumulation, however, is caused by the interaction with the turbulent structures. The length scale for accumulation in this flow was measured to be of the order of 100 wall units. This length scale corresponds to the separation between counter rotating vortices that are responsible for ejection and sweeps in the boundary layer.

The presence of streamwise vortices from the instability of the vertical velocity profile may also play a role in the accumulation of bubbles and deserves further investigation

6.1 Future work

6.1.1 Dynamics of heavy particles in homogeneous isotropic decaying turbulence.

The implications of these experimental results are important and they warrant further investigation of these phenomena, until a better understanding is achieved and models can be implemented to fully account for the mechanism of interaction between the particles and the turbulence. Although there are important questions about the clusters that are still open, namely the existence of more than one characteristic lengths, shape and lifetime, our initial analysis of the particle clustering and the results presented in this thesis are encouraging.

A better characterization of the clustering of particles would bring about better prediction capabilities for both the instantaneous concentration of particles, which is the key variable in problems such as fuel atomization in combustion chambers, and the settling velocity, which is key in sedimentation and rain formation problems. In order to be able to compute the effect of the turbulence on the settling velocity, the intermittency factor of the clusters would need to be described. The lifetime of clusters of a certain concentration, or alternatively, the percentage of time that a particle of a certain size spends in clusters of certain concentrations also needs to be experimentally measured. It was hypothesized that the clusters are formed by the small scale vorticity that accumulates the particles and are destroyed by the large scale structures that disperse the particles in the cluster. This hypothesis should be validated and quantified to provide the necessary statistics of lifetimes of clusters in turbulence. Several other levels of refinement of the model accounting for the shape complexity of the clusters and dependency of the size

PDF on the local concentration could be studied to increase accuracy.

6.1.2 Dynamics of bubbles in a homogeneous isotropic decaying turbulent flow.

The experimental results presented in Chapter 3, while providing new insights on the effect of turbulence on the dynamics of bubbles, leaves many unanswered questions. The continuous refinement of the resolution of the size and velocity measurements is bound to improve the accuracy of the predictions for the rise velocity reduction, specially for very small bubbles. The investigation of the effect of the local bubble concentration on the rise velocity of the bubbles, in parallel with the results from Chapter 2.2.1, could not be carried out due to limitations in the data rate and sampling frequency of the system. A totally different optical setup, and a higher bubble void fraction will be necessary to be able to successfully characterize this phenomena.

The determination of the velocity scale with which the rise velocity reduction should be make non dimensional, will require experiments with a large range of turbulence intensities. The variation of the turbulent scales with the Reynolds number would make possible to determine the best scaling law, and thus could shed more light on the mechanism of interaction between the bubbles and the turbulent flow. The Kolmogorov velocity scale and the r.m.s of the turbulent velocity fluctuations vary in a different way as the Reynolds number in the flow changes, $u_k/u' \approx R_e^{-1/4}$, but the exponent that characterizes their different behaviours is very small. Thus, the difficulty of precisely observing the different characters and establishing the right scaling.

For very similar reasons, determining the proper scale for the bubble clusters created by the preferential accumulation of the bubbles by the turbulence was found to be very difficult. As the ratio of the turbulent micro scales, $\eta/\lambda \approx R_e^{-1/4}$, also vary with a 1/4 exponent on the Reynolds number of the flow, a very wide range of Reynolds numbers would need to be studied for the scaling of the clusters

to be unequivocally determined. Another idea that needs to be explored is the correspondence of the clustering length with the peak of the vorticity spectrum. It is well known that for infinitely high Reynolds number flows, the vorticity spectrum peaks at a wave number of 50, that is at a length scale of 50 times the Kolmogorov length scale. The dependency of finite Reynolds number flows is asymptotic to this value. Studying the evolution of the clustering length with the Reynolds number would help clarify if the accumulation of bubbles is simply associated with the hypothesis that the bubbles respond to the energy of the vortical structures by being driven to their cores and thus the statistics of the instantaneous bubble concentration field mimic those of the vorticity field.

6.1.3 Dynamics of bubbles in a turbulent boundary layer.

A detailed description of the bubbly boundary layer developing along a vertical flat plate has been experimentally studied. However, the characterization of the junction flow at the intersection of the solid wall and the free surface has been done only in a qualitative way. Detailed measurements of the three components of the velocity close to the free surface would be necessary to determine the normal flow away from the wall that is established by the upwards moving carrier fluid as a result of continuity. The effect of this secondary flow on the transport of bubbles and vorticity away from the wall and into the core of the streamwise vortex that dominates the dynamics of this junction flow, needs to be systematically studied as a function of the Reynolds number and bubble void fraction. This characterization would also provide details of the development of the coherent vortex as vorticity lines from the boundary layer are convected to the surface and reconnect.

The effects of bubble size and bubble void fraction on the development of the secondary flows, as characterized by the magnitude of the upwards flow and the position of the crossover point between flow away and towards the wall, would also need to be determined. As the bubbles rise along the boundary layer, the local void fraction and size distribution depends on the distance from the leading

edge and from the free surface. A careful mapping of the bubble void fraction and size distribution would enable the analysis of the origin and evolution of these secondary flows.

Finally, the instability of the vertical velocity profile that is the main source of streamwise vorticity in the flow, needs to be carefully analyzed. The shear layer present in the outer region of the boundary layer has been measured and observed to become unstable in flow visualizations. The mechanism for this instability needs to be clarified, and the most unstable frequency needs to be determined and given a theoretical background.

Bibliography

ATSAVAPRANEE, P. & GHARIB, M. 1997 Structures in stratified plane mixing layers and the effect of cross shear. *J. Fluid Mech.* **342**, 53–86.

BACHALO, W. 1994 Experimental methods in multiphase flows. *Int. J. Multiphase Flow* **20** (Suppl), 261–295.

CATRAKIS, H. J. & DIMOTAKIS, P. 1996 Mixing in turbulent jets: scalar measures and isosurface geometry. *J. Fluid Mech.* **317**, 369–406.

CLIFT, R. G. J. & WEBER, M. 1978 *Bubbles, drops and particles*. Academic Press.

COLES, D. 1956 The law of the wake in a turbulent boundary layer. *J. Fluid Mech.* **1**, 191–226.

COMTE-BELLOT, G. & CORRSIN, S. 1966 The use of a contraction to improve the isotropy of grid-generated turbulence. *J. Fluid Mech.* **25**, 657–682.

CROWE, C., CHUNG, J. & TROUTT, T. 1988 Particle mixing in free shear flows. *Prog. Energy Combust. Sci.* **14**, 171–194.

DEGRAAF, D. & EATON, J. 2000 Reynolds number scaling of the flat-plate turbulent boundary layer. *J. Fluid Mech.* **422**, 319–346.

DETSCH, R. 1989 Small air bubbles in reagent grade water and seawater 1. Rise velocities of 20 to 1000 μm diameter bubbles. *J. Geophys. Res.* **96** (C5), 8901–8906.

DRUZHININ, O. & ELGHOBASHI, E. 1998 Direct numerical simulations of bubble-laden turbulent flows using the two fluid formulation. *Phys. Fluids* **10** (3), 685–697.

EATON, J. 1994 Experiments and simulations on turbulence modification by dispersed particles. *Appl. Mech. Rev.* **47** (6, part 2), 44–48.

ELGHOBASHI, S. & TRUESDELL, G. 1992 Direct numerical simulation of particle dispersion in a decaying isotropic turbulence. *J. Fluid Mech.* **242**, 655–700.

ELGHOBASHI, S. & TRUESDELL, G. 1993 On the two way interaction between homogeneous turbulence and dispersed solid particles. I: Turbulence modification. *Phys. Fluids* **5** (7), 1790–1801.

FELTON, K. & LOTH, E. 2001 Spherical bubble motion in a turbulent boundary layer. *Phys. Fluids* **13** (9), 2564–2577.

FERRANTE, A. & ELGHOBASHI, S. 2004 On the physical mechanisms of drag reduction in a spatially developing turbulent boundary layer laden with microbubbles. *J. Fluid Mech.* **503**, 345–355.

FESSLER, J., KULICK, J. & EATON, J. 1994 Preferential concentration of heavy particles in turbulent channel flow. *Phys. Fluids* **6** (11), 3742–3749.

GREGA, L., HSU, T. & WEI, T. 2002 Vorticity transport in a corner formed by a solid wall and a free surface. *J. Fluid Mech.* **465**, 331–352.

GREGA, L., WEI, T., LEIGHTON, R. & NEVES, J. 1995 Turbulent mixed-boundary flow in a corner formed by a solid wall and a free surface. *J. Fluid Mech.* **294**, 17–46.

HINZE, J. 1975 *Turbulence*. McGraw-Hill.

HOGAN, R., CUZZI, J. & DOBROVOLSKIS, A. 1999 Scaling properties of particle density fields formed in simulated turbulent flows. *Phys. Rev. E* **60** (2), 1674–1680.

KIGER, K. T. 1995 *Particle dispersion and inter-phase kinetic energy transfer in a turbulent, two phase shear layer*. Ph.D thesis, University of California, San Diego.

KLEBANOFF, P. 1955 Characteristics of turbulence in a boundary layer with zero pressure gradient. *NACA Tech. Rep.* **1247**.

LANCE, M. & BATAILLE, J. 1991 Turbulence in the liquid phase of a uniform bubbly air-water flow. *J. Fluid Mech.* **222**, 95–118.

LÁZARO, B. J. & LASHERAS, J. 1992 Particle dispersion in the developing free shear layer. Part 1. Unforced flow. *J. Fluid Mech.* **235**, 143–178.

LONGO, J., HUANG, H. & STERN, F. 1998 Solid/free juncture boundary layer and wake. *Exp. Fluids.* **25**, 283–297.

MAGNAUDET, J. & EAMES, I. 2000 The motion of high Reynolds-number bubbles in inhomogeneous flows. *Ann. Rev. Fluid Mech.* **32**, 659–708.

MARIE, J., MOURSALI, E. & TRANG-CONG, S. 1997 Similarity law and turbulence intensity profiles in a bubbly boundary layer at low void fractions. *Int. J. Multiphase Flow* **23**, 227–247.

MAXEY, M. 1987*a* The gravitational settling of aerosol particles in homogeneous turbulence and random flow fields. *J. Fluid Mech.* **174**, 441–465.

MAXEY, M. 1987*b* The motion of small spherical particles in a cellular flow field. *Phys. Fluids* **30** (4), 1915–1928.

MAXEY, M. & CORRSIN, S. 1986 Gravitational settling of aerosol particles in randomly oriented cellular flows. *J. Atmospher. Sci.* **43**, 1112–1134.

MAXEY, M., PATEL, B., CHANG, E. & WANG, L. 1997 Simulations of dispersed turbulent multiphase flow. *Fluid Dyn. Res.* **20**, 143–156.

MAXEY, M. & RILEY, J. 1983 Equation of motion for a small rigid sphere in a nonuniform flow. *Phys. Fluids* **26** (4), 883–889.

MAXWORTHY, T., GNANN, C., KURTEN, M. & DURST, F. 1996 Experiments on the rise of air bubbles in clean viscous liquids. *J. Fluid Mech.* **321**, 421–441.

MAZZITELLI, I., LOHSE, D. & TOSCHI, F. 2003 On the relevance of the lift force in bubbly turbulence. *J. Fluid Mech.* **488**, 283–313.

MERKLE, C. & DEUTSCH, S. 1992 Microbubble drag reduction in liquid turbulent boundary layers. *Appl. Mech. Rev.* **45**, 103–127.

MOURSALI, E., MARIE, J. & BATAILLE, J. 1995 An upward turbulent bubbly boundary layer along a vertical flat-plate. *Int. J. Multiphase Flow* **21** (1), 107–117.

NIR, A. & PISMEN, L. 1979 The effect of a steady drift on the dispersion of particles in a turbulent fluid. *J. Fluid Mech.* **94**, 369–381.

PANIDIS, T. & PAPAILIOU, D. 2000 The structure of two-phase turbulence in a rectangular channel: an experimental study. *Int. J. Multiphase Flow* **26**, 1369–1400.

POORTE, R. & BIESHEUVEL, A. 2002 Experiments on the motion of gas bubbles in turbulence generated by an active grid. *J. Fluid Mech.* **461**, 127–154.

REEKS, M. 1977 Dispersion of small particles suspended in an isotropic turbulent fluid. *J. Fluid Mech.* **83**, 529–546.

RIGHTLEY, P. & LASHERAS, J. 2000 Bubble dispersion and interphase coupling in a free shear flow. *J. Fluid Mech.* **412**, 21–59.

SEGRE, G. & SILBERBERG, A. 1962 Behaviour of macroscopic rigid spheres in Pouiseuille flow. *J. Fluid Mech.* **14**, 115–157.

SNYDER, W. & LUMLEY, J. 1971 Some measurements of particle velocity autocorrelation function in turbulent flow. *J. Fluid Mech.* **48**, 41–71.

SOMMERFELD, M. & QIU, H. 1995 Particle concentration measurements by phase-Doppler anemometry in complex dispersed two-phase flows. *Exp. Fluids.* **18**, 187–198.

SPELT, P. & BIESHEUVEL, A. 1997 On the motion of gas bubbles in homogeneous isotropic turbulence. *J. Fluid Mech.* **336**, 221–244.

SQUIRES, K. & EATON, J. 1991*a* Measurements of particle dispersion obtained from direct numerical simulations of isotropic turbulence. *J. Fluid Mech.* **226**, 1–35.

SQUIRES, K. & EATON, J. 1991*b* Preferential concentration of particles by turbulence. *Phys. Fluids* **3** (5), 1169–1178.

SREEDHAR, M. & STERN, F. 1998 Prediction of solid/free-surface juncture boundary layer and wake of a surface-piercing flat plate at low Froude number. *J. Fluids Eng.* **120**, 354–362.

SRIDHAR, G. & KATZ, J. 1995 Drag and lift forces on microscopic bubbles entrained by a vortex. *Phys. Fluids* **7** (2), 389–399.

TAYLOR, G. 1921 Diffusion by continuous movements. *Proc. R. Soc. Lond. A* **20**, 196–211.

THORPE, S. 1985 Laboratory observations of secondary structures in Kelvin-Helmholtz billows and consequences for ocean mixing. *Geophys. Astrophys. Fluid Dyn.* **34**, 175.

TIO, K., GAÑÁN CALVO, A. & LASHERAS, J. 1993*a* The dynamics of small, heavy, rigid spherical particles in a periodic Stuart vortex flow. *Phys. Fluids* **5** (7), 1679–1693.

TIO, K., LAHERAS, J., GAÑÁN CALVO, A. & LIÑÁN, A. 1993*b* The dynamics of bubbles in periodic vortex flows. *Appl. Sci. Res.* **51** (1–2), 285–290.

WANG, L. & MAXEY, M. 1993*a* Settling velocity and concentration distribution of heavy particles in homogeneous isotropic turbulence. *J. Fluid Mech.* **256**, 27–68.

WANG, L. & MAXEY, M. 1993*b* The motion of microbubbles in a forced isotropic and homogeneous turbulence. *Appl. Sci. Res.* **51**, 291–296.

WELLS, M. & STOCK, D. 1983 The effect of crossing trajectories on the dispersion of particles in a turbulent flow. *J. Fluid Mech.* **136**, 31–62.

YANG, C. & LEI, U. 1998 The role of the turbulent scales in the settling velocity of heavy particles in homogeneous isotropic turbulence. *J. Fluid Mech.* **371**, 179–205.

ZAGAROLA, M., PERRY, A. & SMITS, A. 1997 Log laws or power laws: the scaling in the overlap region. *Phys. Fluids* **9** (7), 2094–2100.